Materials Preparation and Characterization of the Quasi-Two Dimensional Triangular Rare-Earth Magnets $Ba_6Yb_2Ti_4O_{17}$ and $ErMgGaO_4$

MATERIALS PREPARATION AND CHARACTERIZATION OF THE QUASI-TWO DIMENSIONAL TRIANGULAR RARE-EARTH MAGNETS $\mathrm{BA_6YB_2TI_4O_{17}}$ AND $\mathrm{ERMGGAO_4}$

By Zachary W. CRONKWRIGHT,

A Thesis Submitted to the School of Graduate Studies in the Partial Fulfillment of the Requirements for the Degree Masters of Science

McMaster University
November 24, 2020

McMaster University
Masters of Science (2020)
Hamilton, Ontario (Department of Physics and Astronomy)

TITLE: Materials Preparation and Characterization of the Quasi-Two Dimensional Triangular Rare-Earth Magnets $Ba_6Yb_2Ti_4O_{17}$ and $ErMgGaO_4$
AUTHOR: Zachary W. Cronkwright (McMaster University)
SUPERVISOR: Dr. Bruce D. Gaulin
NUMBER OF PAGES: xiv, 100

Abstract

Within in this work, I present the successful synthesis of $Ba_6Yb_2Ti_4O_{17}$ in a powder form. To the best of my knowledge, this is the first instance in which this has been achieved. I also show that single crystal synthesis experiments using the floating zone synthesis (FZS) technique have yet to produce single crystals. The magnetic characterization of $Ba_6Yb_2Ti_4O_{17}$ powder is also presented. DC susceptibility measurements reveal no spin freezing or ordering down to 0.5K and inverse susceptibility shows antiferromagnetic coupling between spins. A cold neutron scattering experiment was performed at low temperatures with and without an applied magnetic field on $Ba_6Yb_2Ti_4O_{17}$ powder. This experiment shows the possibility of spinon-like excitations with a band width of approximately 0.3meV, but this is inconclusive due to the signal to noise ratio. The powder averaged g-tensor for $Ba_6Yb_2Ti_4O_{17}$ was also experimentally estimated to be approximately 2.4. Further work required to complete this study is also discussed.

Synthesis of phase pure $ErMgGaO_4$ has yet to be reported in the literature. Here, I show that small amounts of phase pure polycrystalline $ErMgGaO_4$ can be produced using the FZS technique. Through using FZS, 0.85g of phase pure $ErMgGaO_4$ powder was produced and supplemented using 1.26g of $ErMgGaO_4$ powder containing approximately 1% $Er_3Ga_5O_{12}$ magnetic impurity. To estimate the effect of this magnetic impurity on the magnetic signatures exhibited by $ErMgGaO_4$, DC susceptibility measurements were performed between 0.5K and 50K. The magnetic impurity in such small quantity was shown to have negligible effect on the bulk $ErMgGaO_4$ magnetic features. Cold neutron scattering conducted on this material revealed a spinon excitation continuum similar to the one observed in $YbMgGaO_4$.[1] Also present at low temperatures was a diffuse elastic magnetic feature that was used to estimate an order parameter for the material. Analysis of this diffuse feature also revealed a Warren line shape, indicative of two dimensional correlations within the Er^{3+} triangular planes. Analysis of the spinon excitation continuum revealed a gapless spinon continuum overall. Results presented for both $Ba_6Yb_2Ti_4O_{17}$ and $ErMgGaO_4$ will be discussed and compared to neutron scattering experiments performed on $YbMgGaO_4$

Acknowledgements

I would like to take some time to acknowledge and express my gratitude for the help that was provided to me in the completion of this work. I will begin with my supervisor Prof. Bruce Gaulin. Being a member of the Gaulin research group has provided me with the opportunity to learn and grow as not only a scientist, but as a person. I have formed relationships with colleagues that I know will last a lifetime and for that I am eternally grateful. I also cannot begin to express my gratitude for the direction and technique training being a member of the Gaulin group afforded me. Without Prof. Gaulin, this work would have been impossible.

The neutron scattering experiments presented in this work were performed using DCS at NIST in Gaithersburg, Maryland, USA and IN6-SHARP at ILL in Grenoble, France. These experiments were performed by myself and a team of collaborators, so I would like to take moment to thank them. Firstly, I would like to express my gratitude to Edwin Kermarrec and Suvam Bhattacharya, our collaborators from the Université Paris-Saclay for fruitful discussions and assistance in conducting the experiments and data analysis. I would also like to thank Nick Butch and Craig Brown at DCS and Jean-Marc Zanotti at IN6-SHARP. These instrument scientists provided invaluable insight into the operation of the instruments and data reduction of the resultant data sets and was it was a pleasure to work with them.

I would like to thank Prof. Graeme Luke and Sudarshan Sharma for their help with the DC susceptibility measurements performed in this work. The susceptibility measurements were performed using a SQUID magnetometer belonging to Prof. Luke and his graduate student Sudarshan Sharma trained me in its use. I would also like to thank my group-mates Connor Buhariwalla, Kyle Ma and Evan Smith as well as my office mates James Beare, Matthew Nugent, Mathew Pula and Megan Rutherford. The assistance provided by the BIMR crystal synthesis laboratory manager, Casey Marjerrison, was also imperative to this work. Your friendship and assistance made this work possible.

Lastly, I would like to thank my parents, Judy and Daryl, and my significant other, Hannah. Without your support over theses last two years, none of this would been possible. Thank you!

Co-Authorship

The work presented in Chapters 4 and 5 of this thesis were performed as collaborative efforts. Synthesis of materials was performed by myself, Casey Marjerrison, James Beare, Evan Smith, Sudarshan Sharma, Matthew Nugent and Mathew Pula. Susceptibility measurements were performed in collaboration with Prof. Graeme Luke and Sudarshan Sharma.

The inelastic neutron scattering experiments performed on $Ba_6Yb_2Ti_4O_{17}$ were conducted using the DCS instrument at NIST. This experiment was performed on a powder sample provided by Edwin Kermarrec and Suvam Bhattacharya from the Université Paris-Saclay. The experiment was performed by myself, Edwin Kermarrec, Suvam Bhattacharya and DCS instrument scientists Nick Butch and Craig Brown. The data analysis presented in Chapter 4 was performed by myself, with direction from Prof. Bruce Gaulin.

Inelastic neutron scattering performed on $ErMgGaO_4$ was conducted using IN6-SHARP at ILL in Grenoble-France. This experiment was performed in collaboration with Edwin Kermarrec, Suvam Bhattacharya, Sylvain Petit and Jean-Marc Zanotti. Once again, the data analysis of the experimental results, presented in Chapter 5, was performed by myself under the supervision of Prof. Gaulin.

Contents

List of Figures

List of Tables

I dedicate this thesis work to my grandparents Margret and Willis Cronkwright. Thank you for your love and support!

Chapter 1

Introduction

I will use this chapter to introduce the relevant background information and physical concepts related to the study of rare-earth triangular magnets. Here, I will briefly discuss magnetism in matter and geometrical frustration, specifically in the context of quasi-two dimensional triangular materials. Then, I will discuss how geometrical frustration can lead to exotic quantum spin liquid (QSL) ground states. To end the chapter, I will introduce recent results on the triangular rare-earth magnet $YbMgGaO_4$, which here serves as the motivation for this work.

1.1 Magnetism in Materials

Magnetism is present in materials when one or more of the material's constituent ions produce local magnetic moments. These local moments are produced by unpaired electrons in the ions' electronic configuration. Because materials consist of many interacting ions, magnetism can be quite complicated. As such, I will begin the discussion by considering isolated magnetic ions and building from there. In an isolated magnetic ion, there are many electrons, each occupying a state defined by a unique set of quantum numbers. Due to the angular motion of the electron and it's intrinsic spin angular momentum, each individual electron can be prescribed a total angular momentum operator, $\mathbf{J}$, defined as:

$$\mathbf{J} = \mathbf{L} + \mathbf{S} \tag{1.1}$$

where **L** is the angular momentum operator and **S** is the spin angular momentum operator. Because the z-component of **L** (**S**) can take any of $2L + 1$ $(2S + 1)$ values in the series $-L, -L + 1, ..., L - 1, L$ $(-S, -S + 1, ..., S - 1, S)$, there are $(2L+1)(2S+1)$ values available to the z-component of **J**. Due to the large number, the ground state electron configuration that preserves the Pauli Exclusion Principle while minimizing the free energy of the ion is not immediately obvious. This problem was solved by Friederich Hund in the 1920's with the development of the so-called "Hund's Rules". They read as follows[2]:

1. Configure the electrons in the ground state such that S is maximized. This ensures that no energy level in the ground state configuration contains electrons with parallel spins, thus adhering to the Pauli Exclusion Principle while minimizing the Coloumb repulsion.
2. Configure the electrons in the ground state such that L is maximized. This minimized the amount of time electrons travelling within the same orbital are in close proximity, thus minimizing the Coloumb repulsion.
3. The correct value of J is dependant on how many electrons are present to fill the energy levels. If the previous two rules have been followed, and the number of electrons is such that the orbital is less than half full, then $J = |L - S|$. If the shell is more than half full, $J = |L + S|$. This will minimize the spin-orbit energy.

It is important to note that the above description only applies to the ground state configuration of the ion. This does not provide information for excited states but, nevertheless, provides a strong foundation for the upcoming discussions.

1.1.1 Effects of the Local Environment

In the above discussion, I assumed a completely isolated magnetic ion wherein the electron energy levels in the given orbital were completely degenerate (i.e. had the same energy). That is not the case when the assumption is relaxed to include the ion's immediate environment. Here, I will consider a positively charged magnetic ion surrounded by some number of negatively charged oxygen ions (as is the case with the materials studied in this work). The effect of the negative ions is to produce a potential energy, V_{CEF}, that splits the degenerate energy levels in the considered orbital (what will now be referred to as crystal electric field levels (CEF)). The extent to which this potential affects the ground state is not a trivial matter. The calculation of the ground state eigenfunction is only possible with accuracy when fitting to measured results. Nevertheless, a point charge approximation (i.e. an approximation ignoring the spatial extent of the involved ions) can be used to make an "in-the-right-ballpark" estimate.[3]

The calculation begins with determining the appropriate potential. Attempting to calculate this potential in terms of Cartesian coordinates is quite cumbersome. It is therefore beneficial consider to the potential in terms of the tesseral harmonics. Following the calculation outlined in [3], one arrives at a potential of the form:

$$V_{CEF}(r,\theta,\phi) = \sum_{n=0}^{\infty}\sum_{\alpha} r^n \gamma_{n\alpha} Z_{n\alpha}(\theta,\phi) \tag{1.2}$$

where r, θ and ϕ are the coordinates of the magnetic ion, n is the order of the tesseral harmonic, α corresponds to their being Z_{n0}, Z^c_{nm} and Z^s_{nm} for all $m \leq n$ and $\gamma_{n\alpha}$ is defined as:

$$\gamma_{n\alpha} = \sum_{j=1}^{k} \frac{4\pi}{(2n+1)} q_j \frac{Z_{n\alpha}(\theta_j,\phi_j)}{R_j^{n+1}} \tag{1.3}$$

Here, j corresponds to the j^{th} oxygen ion in the local environment, q_j the charge of the j^{th} oxygen, R_j the distance of the j^{th} oxygen from the origin and θ_j and ϕ_j the angular coordinates of said oxygen ion. This is convenient because there is a direct correspondence between the $Z_{n\alpha}$ and the so-call "Stevens' operator equivalents" for angular momentum. From here, the CEF Hamiltonian can be written as follows:

$$\mathcal{H}_{CEF} = \sum_{nm} B_n^m \mathbf{O}_n^m \tag{1.4}$$

where B_n^m are coefficients determined by the point group symmetry of the magnetic ion (referred to as CEF parameters henceforth) and $\mathbf{O}_n^m$ are the operator equivalents for the magnetic ion and are dependant on the $\mathbf{J}_z$, $\mathbf{J}_+$ and $\mathbf{J}_-$ matrices corresponding to the ion in question. Here, the CEF parameters are defined as:

$$B_n^m = C_n^m \langle r^n \rangle \theta_n (-|e|) \gamma_{nm} \tag{1.5}$$

where the subscript α has been replaced with m due to the fact that the point group can be rotated such that all Z_{nm}^s appearing in $\gamma_{n\alpha}$ vanish[3], C_n^m are the multiplicative constants appearing in the corresponding Z_n^m, $\langle r^n \rangle$ are parameters determined by Hartree-Fock analysis for a number of rare-earths in [4] and θ_n is tabulated for all rare-earths in [3].

The number of CEF parameters appearing in Equation 1.4 are determined by the point group symmetry. The symmetry operations of the magnetic ion only allow for certain terms to appear in the CEF Hamiltonian, causing all others to vanish. The point groups C_{3v} and D_{3d} - the point groups of consideration in this work - have CEF Hamiltonians of the same form[3, 4, 5]:

$$\mathcal{H}_{C_{3v},D_{3d}} = B_2^0 \mathbf{O}_2^0 + B_4^0 \mathbf{O}_4^0 + B_4^3 \mathbf{O}_4^3 + B_6^0 \mathbf{O}_6^0 + B_6^3 \mathbf{O}_6^3 + B_6^6 \mathbf{O}_6^6 \tag{1.6}$$

Using the CEF Hamiltonian, one can solve the eigenvector/eigenvalue problem to estimate the structure of the ground state as well as the energies and structure of the CEF excited states in the m_j basis. It can also be used to determine the spin anisotropy in the system, which will be presented later.

1.1.2 Magnetic Interactions

I will now extend this discussion from the local environment to the magnetic interactions within and between unit cells. The effects of interactions between magnetic moments within the crystalline lattice can have pronounced effects on the ground state and excited state physics of the material in question. I will begin by discussing the magnetic dipole interaction - that is, the interaction between two magnetic dipoles, $\boldsymbol{\mu}_1$ and $\boldsymbol{\mu}_2$, separated by a displacement $\mathbf{r}$. The interaction energy between these dipoles is defined as:

$$E = \frac{\mu_0}{4\pi r^3}\left[\boldsymbol{\mu}_1 \cdot \boldsymbol{\mu}_2 - \frac{3}{r^2}(\boldsymbol{\mu}_1 \cdot \boldsymbol{r})(\boldsymbol{\mu}_2 \cdot \boldsymbol{r})\right] \tag{1.7}$$

where μ_0 is vacuum permeability. This energy is dependant on the distance between the magnetic moments and their relative alignment. As such, this interaction is usually on the order of 1K in strength and is not typically relevant to materials that order at high temperatures.[2]

Much more interesting is the exchange interaction between magnetic moments within the lattice. As a first approximation and, regarding only the spin contribution, this exchange interaction Hamiltonian has a simple form:

$$\mathcal{H} = -\sum_{\langle ij \rangle} J_{ij}\mathbf{S}_i \cdot \mathbf{S}_j \tag{1.8}$$

where $\langle ij \rangle$ denotes the sum is taken over nearest neighbors, J_{ij} is the nearest neighbor exchange integral and $\mathbf{S}_i$ and $\mathbf{S}_j$ are the spin operators for the i^{th} and j^{th} magnetic ions on the lattice. This is derived from a system in which the unpaired electrons are well localized to the ions' positions (this is known as the Heilter-London Model).[6] If $\mathbf{S}_{i,j}$ is allowed to point in any direction, this is referred to as the "Heisenburg Model".[2, 7]

The simplest form of exchange is "direct" exchange. Here, electrons on neighbouring sites can virtually hop from site to site, provided unpaired electrons are present to accommodate this. This type of exchange is often not relevant to magnetic materials comprised of rare-earth ions as there is not a significant amount of orbital overlap for the electrons to communicate (i.e. the electron density is extremely small in the interstitial region, thus preventing a direct exchange path). It is for this reason that an intermediary is required. This can be satisfied by the oxygen environment surrounding the magnetic ions. Here, the overlap of the unpaired electron orbital in the magnetic ions and the full p orbital in the oxygen allows the unpaired electrons to become delocalized. It is typically through this interaction that magnetic materials are able to magnetically order.[2]

This is not the only magnetic interaction relevant to magnetic ordering. The oxygen ions are not the only pathway by which two neighboring magnetic ions can interact. Magnetic ions can exchange energy through a spin-orbit interaction.[2] Instead of exchanging energy through oxygen ions, the magnetic ions may exchange energy through spin-orbit coupling in a pseudo-dipolar way.[8] This is known as the Dzyaloshinski-Moriya (DM) Interaction and is defined by:

$$\mathcal{H}_{DM} = \mathbf{D} \cdot \mathbf{S}_i \times \mathbf{S}_j \tag{1.9}$$

where $\mathbf{S}_i$ and $\mathbf{S}_j$ are the interacting spins and $\mathbf{D}$ is a vector that vanishes if there is an inversion symmetry present between the interacting ions (i.e. this vector coefficient will provided the crystal symmetry is sufficiently high).[8] If $\mathbf{D}$ does not vanish, then it will lie either parallel or perpendicular to the line joining the spins. It will then serve to "cant" the spins. This can result in a "weak ferrormagnetism" in antiferromagnetic materials.[2]

1.1.3 Magnetic Ordering

Prior to discussing the effects of magnetic ordering, it is useful to recall some important definitions. The first being that of the magnetization. This can be defined in several ways. The magnetization, $\mathbf{M}$, is defined as:

$$\mathbf{M} = \sum_i \frac{\boldsymbol{\mu}_i}{V} \tag{1.10}$$

where $\boldsymbol{\mu}_i$ is the i^{th} magnetic moment and V is the volume. When the material is in a magnetically disordered state (i.e. in a state where the temperature is high enough that the thermal energy is large enough to cause the spins to fluctuate in spite of the exchange interactions) then the material has no net magnetization. If the temperature is lowered and the spins align in one direction, then a spontaneous magnetization will occur.

From a statistical mechanical standpoint, the magnetization can be defined in terms of the Helmholtz free energy of the magnetic system. Starting with the differential form of the free energy:

$$dF = -TdS - MdH \tag{1.11}$$

it is immediately follows that:

$$M = -\left(\frac{\delta F}{\delta H}\right)_T \tag{1.12}$$

By Equation 1.11, when the temperature approaches zero, the only mehcanism by which the magentic system can minimize it's free energy is through the onset of a net magnetization. Magnetization can also be defined on grounds of classical electromagnetism. If one considers a linear material (i.e. a material whose magnetization scales linearly with the applied magnetic field) then the magnetization can be written in the form:

$$\mathbf{M} = \chi\mathbf{H} \tag{1.13}$$

where χ is known as the dimensionless magnetic susceptibility. This quantity reveals how effective the magnetic field is at aligning spins within the material. These two observables are of particular interest in magnetic materials due to the pronounced effects of ordering.

I will now consider a magnetic system in that is not magnetically ordered. In such a system, the spins are all directed and fluctuating in random directions. This system is therefore said to be in a paramagnetic state. When a magnetic field is applied, the spins will be forced to align with one another. This corresponds to a magnetic susceptibility that is always positive and the onset of a net magnetization. For a general spin system (i.e. a system that can take any total angular moment,

J), using Equation Equation 1.10, the magnetization becomes:

$$M = ng_J\mu_B\langle m_J\rangle \tag{1.14}$$

where $n = N/V$, $\langle m_J\rangle$ is the expectation value of m_J, the z-component of $\mathbf{J}$ and g_J, the Landé g-value, is defined as:

$$g_j = \frac{3}{2} + \frac{S(S+1) - L(L+1)}{2J(J+1)} \tag{1.15}$$

Using this form of the magnetization and recalling from statistical mechanics that:

$$\langle m_J\rangle = \frac{\sum_{m_j=-J}^{J} m_j e^{m_J x}}{\sum_{m_J=-J}^{J} e^{m_J x}} \tag{1.16}$$

where $x = g_J\mu_B B/k_B T$, on arrives at the result that the magnetization in a paramagnetic system given by:

$$M = M_S B_J(y) \tag{1.17}$$

where $M_S = ng_J\mu_B J$ and is known as the saturation magnetization, $y = xJ$ and $B_J(y)$ is the Brillouin Function defined as:

$$B_J(y) = \frac{2J+1}{2J}\coth\left(\frac{2J+1}{2}y\right) + \frac{1}{2J}\coth\left(\frac{1}{2}y\right) \tag{1.18}$$

Details of the calculation can be found in [2].

This form allows for the deduction of the temperature dependence of the susceptibility. Rearranging Equation 1.13, and using a small magnetic field (i.e. $y \ll 1$), one arrives to a susceptibility of the form:

$$\chi = \frac{n\mu_0\mu_{eff}^2}{3k_B T} \tag{1.19}$$

where μ_{eff} is known as the effective moment and is given by:

$$\mu_{eff} = g_J \mu_B \sqrt{J(J+1)} \tag{1.20}$$

and is known as Curie's Law. This relation shows that the susceptibility of a paramagnetic material is asymptotic about 0K. If one plots the inverse susceptibility and extrapolates the data to the T-axis, the T-intercept is 0K for a paramagnetic material.

The interactions presented in the Section 1.1.2 can have pronounced effects on the low temperature physics in materials. The Hamiltonian presented in Equation 1.8 can be used to describe a model system of spins can point in any direction in 3D space (also known as the so-called "Heisenburg Model"). If a magnetic field is applied, then the model Hamiltonian for such a system takes the form[2]:

$$\mathcal{H} = -\sum_{\langle ij \rangle} J_{ij} \mathbf{S}_i \cdot \mathbf{S}_j + g\mu_B \sum_j \mathbf{S}_j \cdot \mathbf{H} \tag{1.21}$$

where g is once again the Landé g-value, μ_B is the Bohr magneton and $\mathbf{H}$ is the applied magnetic field. In a material containing anisotropic spins, the g-factor must be replaced with a "g-tensor". Should the value of J_{ij} be positive, then it is clear to see that the energy of this model system would be minimized should the spins be aligned in the same direction (they would tend to align anti-parallel if J_{ij}<0). Thus, should the exchange be strong enough, as the temperature of the system is lowered, the thermal energy will not be enough to cause the spins to continue to fluctuate. The spins will then be forced to align. If they align parallel to one another, the system has undergone a transition to a ferromagentic state (if they align anti-parallel, they system is said to be ordered into an anti-ferromagnetic state).[2, 9]

To examine the consequences of a ferromagnetically ordered system one can apply an approximation, that is the so-called "mean field theory". This assumes that the spins in the magnetic system all experience the exact same field, regardless of their position in the material.[9] Thus each spin in the system is functionally the same. As such, one can transform the Hamiltonian presented in Equation 1.21 to[2]:

$$\mathcal{H} = g\mu_B \sum_i \mathbf{S}_i \cdot (\mathbf{H} + \mathbf{H}_{mf}) \tag{1.22}$$

where $\mathbf{H}_{mf}$ is:

$$\mathbf{H}_{mf} = -\frac{2}{g\mu_B} \sum_j J_{ij}\mathbf{S}_j \tag{1.23}$$

The ferromagnetic Hamiltonian now has the same form as the paramagnetic Hamiltonian, with the applied field now being represented by the mean field approximation $\mathbf{H} + \mathbf{H}_{mf}$. As such, the results presented for the paramagnetic case hold true for the ferromagnetic case in a mean field approximation with y now being given the form[2]:

$$y = \frac{g_J\mu_B(H + \lambda M)}{k_B T} \tag{1.24}$$

where λ is the proportionality constant that determines how strongly the mean field forces the spins to align. This is know as "self consistent mean field theory".[9] If one examines the case where H=0, then by Equation 1.24,

$$M = \frac{k_B T y}{g_J\mu_B J\lambda} \tag{1.25}$$

and in setting this equal to Equation 1.17 when y is small, one can determine the transition temperature T_C. If the temperature is above T_C, then the only point at which Equation 1.25 and Equation 1.17 intersect is at $M = 0$. If T is below T_C, then the two equations will intersect at three points and if $T = T_C$ then the gradients of both equations with be exactly the same in the region of small y. As such, the transition temperature for a ferromagnetic material can be defined as[2]:

$$T_C = \frac{g_J \mu_B (J+1) \lambda M}{3k_B} = \frac{n\lambda \mu_{eff}^2}{3k_B} \tag{1.26}$$

At this temperature, the material exhibits the onset of a spontaneous magnetization, that will increase from zero to the saturation magnetization, M_S, at low temperatures. Above the transition temperature, there is no magnetization. For this type of material, the magnetization is continuous at T_C but the first derivative is not. As such, this is know as second-order phase transition.[9] When one applies a small magnetic field, then on can determine the magnetic susceptibility of the ferromagnetic material. In the small y limit, the susceptibility can be defined as[2]:

$$\chi = \frac{C}{T - T_C} \tag{1.27}$$

where C is a constant. This simple relation is known as the Curie-Weiss Law. Thus, one can accurately determine T_C through plotting the inverse susceptibility and extrapolating to $1/\chi$=0.

The antiferromagnetic state is one in which the spins are aligned anti-parallel to one another (i.e. $J_{ij} < 0$). As was the case in ferromagnetic materials, an antiferromagnetic material is in a paramagnetic state at high temperatures, as the thermal energy is large enough to overcome the interactions. As the temperature is lowered, exchange between neighboring spins becomes important and the spins will try to align anti-parallel to minimize the energy. This, along with the paramagnetic and ferromagnetic states are shown on a simple square lattice in Figure 1.1. Because adjacent spins are pointed in opposing directions, one would expect the magnetization to be zero. While this is true, it is distinctly different than the paramagnetic state. If one extends Figure 1.1c to the extent of a bulk material, then the square lattice can be divided into two interwoven square ferromagnetic sublattices, one with spin up and one with spin down. Using this construction, the mean fields experienced by the spin up lattice and the spin down lattice are respectively represented by[2]:

$$\mathbf{B}_{+mf} = -|\lambda|\mathbf{M}_{-} \tag{1.28}$$

$$\mathbf{B}_{-mf} = -|\lambda|\mathbf{M}_{+} \tag{1.29}$$

Following this prescription one arrives at the result:

$$M_{\pm} = M_S B_J\left(\frac{-g_J \mu_B J|\lambda|M_{\mp}}{k_B T}\right) \tag{1.30}$$

Since the field experienced by each sublattice has the same strength but is directed in opposite directions, the total magnetization of an antiferromagnetic material is truly zero when in the antiferromagnetic state. The temperature at which this transition occurs is know as the Néel temperature, T_N.[2] Like T_C, T_N is defined as:

$$T_N = \frac{n|\lambda|\mu_{eff}^2}{3k_B} \tag{1.31}$$

Like the paramagentic and ferromagnetic states, the magnetic susceptibility can be given in terms of T_N. It takes a very similar form to Equation 1.27:

$$\chi = \frac{C}{T + T_N} \tag{1.32}$$

where C is once again a constant. When one analyzes the inverse susceptibility, T_N is once again found by extrapolating the data to the T-intercept. In the case of an antiferromagnet, the intercept is now negative. In comparing Equation 1.19, Equation 1.27 and Equation 1.32 one can define the magnetic susceptibility for a general magnetic system as:

$$\chi = \frac{C}{T-\theta} \tag{1.33}$$

where θ is know as the Weiss temperature. If $\theta = 0$, then the material is paramagnetic, if $\theta > 0$, ferromagnetic and if $\theta < 0$, antiferromagnetic.

1.2 Geometrical Frustration

Geometrical frustration is an interesting physical property exhibited in some magnetic materials. Should the magnetic sublattice of the material be constructed in triangular motifs, it can at times be impossible for the magnetic ions to satisfy all pairwise interactions between nearest neighbors simultaneously (in principle, the magnetic lattice need not be constructed in triangular motifs to create this situation but, as frustration brought about by two dimensional triangular planes is the focus of this work, I will confine this discussion to geometrical frustration involving triangular structures). This is easily understood when one considers the triangle presented in Figure 1.2a. If the magnetic ions appended to the vertices of the triangle are Ising (i.e. the spins can only be directed in either the "up" or "down" directions) and are coupled by an antiferromagnetic exchange, then it will be impossible for the triangle to find a unique configuration that minimizes the free energy of the system. Regardless of the orientation of the first two spins on the triangle, the third will be unable to satisfy the antiferromagnetic exchange with one of the other two. Thus, the triangle has a 6-fold degeneracy when considering the spins on all three vertices. This is compounded when the degeneracy is extended across the the material as triangular lattice (Figure 1.2b) or the so-called Kagome lattice (Figure 1.2c) - that is a two dimensional lattice of corner sharing triangles. It has been shown that the triangular lattice consisting of such antiferromagnetically-coupled Ising spins gives rise to a ground state with large degeneracy. At zero temperature the entropy is $0.3383R$.[10] This large degeneracy and finite ground state entropy leads to the persistence of ground state cooperative fluctuations of spins. This is analogous to the fluctuations present in a liquid

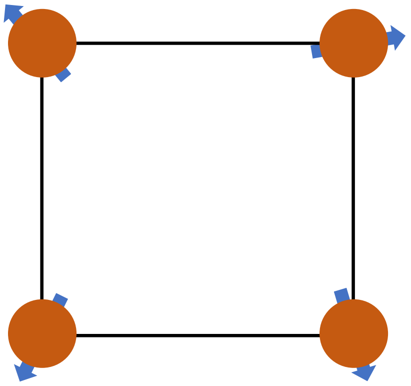

(A) Paramagnetism

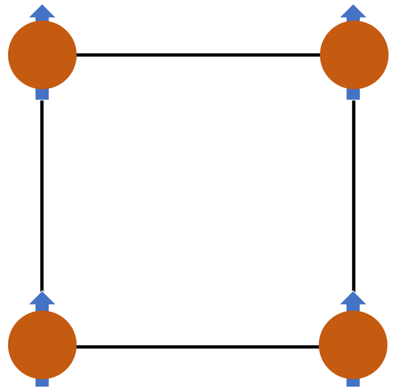

(B) Ferromagnetism

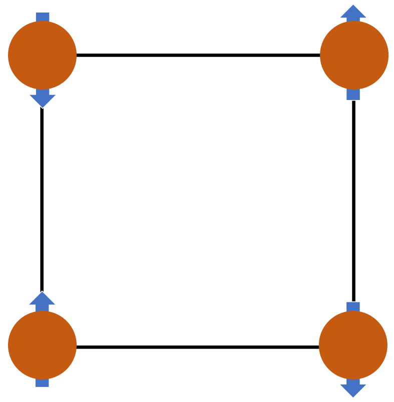

(C) Antiferromagnetism

Figure 1.1: Schematic diagram of common magnetic orders on a square lattice. It is important to note that in the paramagnetic case shown in (A), the spins are not static and are instead randomly fluctuating in time.

as atoms in a liquid fluctuate in a correlated way. Thus, geometrically frustrated materials can produce a class of magnetic materials known as spin liquids.[11]

Spin liquid materials can be divided into two camps, depending on the value of the spin quantum number S. If S is large in comparison to the minimum value allowed by quantum mechanics (that being $\hbar/2$), then the material is said to be a classical spin liquid. In a spin liquid material where spins are considered in the classical regime, the fluctuations of said spins are dominated by the thermal energy provided by the temperature. As $k_B T$ is lowered, the fluctuations will become weaker, and unconventional orders can arise.[11] One such example is that of spin ice materials. These materials consist of a rare-earth magnetic ion with high spin on the pyrochlore lattice (that is, a lattice comprised of two interwoven networks of corner sharing tetrahedra). If the material exhibits a strong ferromagnetic Ising interaction, then, due to the geometry of the lattice, it will be impossible for all spins to align in one direction. This is due to the fact that the the directions of the four sublattice positions of the tetrahedron are not collinear. This will cause two spins to point inward and two spins to point outward with respect to the center of each tetrahedra (i.e. two-in-two-out order). This is know as spin ice due to the analogous nature of the material to that of the two-in-two-out configuration of the protons in water ice.[11] The comparison does not end there however, as this system has been shown to exhibit the same ground state entropy as that of water ice.[12] The second group of spin liquid materials consists of frustrated materials whose magnetic ions exhibit spins approaching the fundamental quanta of spin, known as quantum spin liquids.

1.3 Quantum Spin Liquids

When a material exhibits geometrical frustration in combination with magnetic ions with spins approaching $\hbar/2$, it can produce a unique and interesting class of quantum magnet. Such a material is know as a quantum spin liquid (QSL). As was the case in the classical spin liquid, the spins present in the material are analogous to atoms in a liquid in that they fluctuate in a correlated manner. They differ in the sense that in the classical spin liquid, because S is large, quantum effects

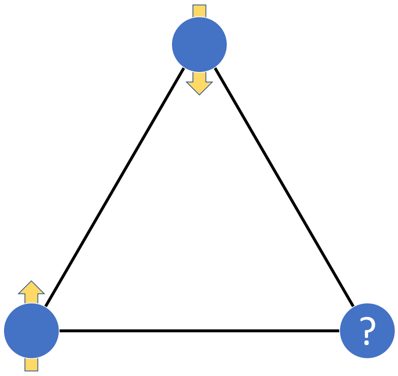

(A) Geometrical frustration on a triangle

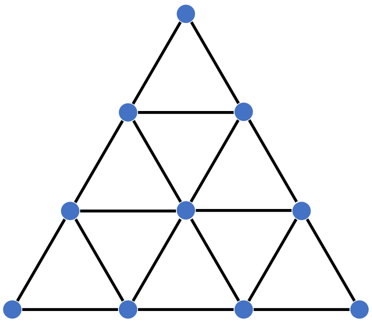

(B) Triangular lattice

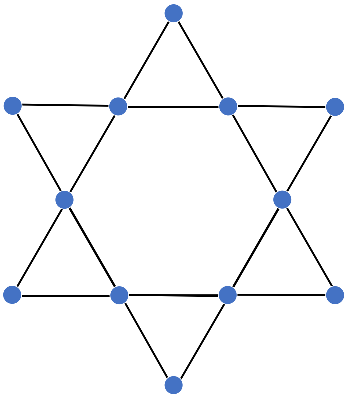

(C) Kagome lattice

FIGURE 1.2: Schematic diagram of geometrical frustration on common magnetic sublattices.

to the energy of the system are small. Due to enhanced quantum effects in QSL materials, the spins are allowed to fluctuate (i.e. change their direction randomly) even down to $T = 0$.[11] These fluctuations are known as quantum fluctuations (these are analogous to thermal fluctuations that are the random changing of the spin direction brought about by thermal energy). This amounts to a material that has a non-magnetic ground state consisting of magnetic moments.

The ground state wavefunction of a QSL material is built with consideration to valence bonds, that is, a dimer comprised of two spins resulting in a spin-0 singlet state.[11] This produces a state in which each spin is highly entangled with its bond mate. This, however, is not enough to describe the QSL state as it does not preserve the lattice symmetries of the crystal. Thus, one must construct a ground state as a superposition of all partitionings of spins into pairs, regardless of the length of the valence bond, multiplied by the configurations weighting factor. Such a configuration is know as the "resonating valence bond" and was shown to be the ground state of the triangular antiferromagnet with spin equal to $\hbar/2$ by P. Anderson in 1973.[13] One of the possible partitionings is shown schematically in Figure 1.3. Because the length of the bond can be arbitrary, those valance bonds spanning a large distance require little energy to be destroyed and this ground state is therefore gapless. If the weighting of the states is such that the ground state is primarily constructed from long range bonds, then excitations brought about by such bonds would be of comparatively small energy with those from short ranged valence bonds.[11] This produces a large number of possible ground states for QSL correlations and thus a large variety in types of QSL materials.

With such a diverse landscape of physical phenomena present in the various types of QSL's, it has been difficult to find one characteristic signature they all share. One possibility is that of a of an exotic particle known as a spinon. A spinon is a $S = 1/2$ (in units of $\hbar$) quasi-particle that has neutral charge. The magnon, (the quasi-particle used to represent spin waves in magnetically ordered materials), in contrast, is spin-1 with neutral charge.[11] The spinon is well known to exist in certain 1D materials (referred to as 1D spin chains). In the 1D spin chain, the spinon manifests as two domain walls surrounding a spin that has been flipped out of the ordered arrangement. The domain walls are then able to move

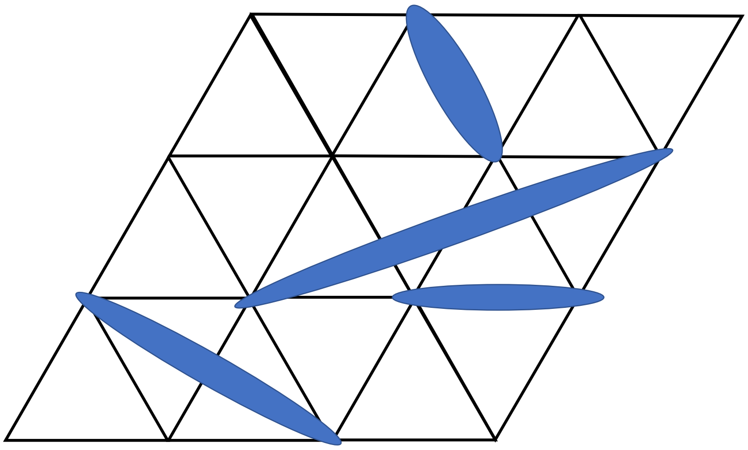

FIGURE 1.3: Resonating Valance Bond schematic

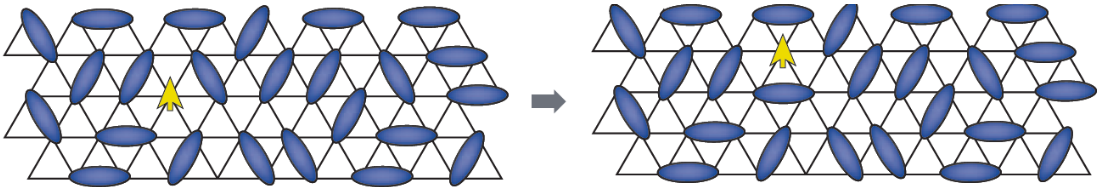

FIGURE 1.4: Cartoon picture of a spinon in two dimensions. Adapted with permission from Springer Nature: Nature Physics [11]. ©

throughout the chain, flipping spins, so that the spin chain re-establishes the local magnetic order.[11] In a two dimensional system, the spinon manifests by breaking a dimer, then rearranging the dimer pairs with the new flipped spin. This is shown on the triangular lattice in Figure 1.4.

Experimental realizations of QSL ground states have been difficult to come by. This is due to the fact that they are chiefly characterized by what they are not, that is, a state without broken symmetry and no long range order down to 0K.[11] This difficulty is compounded with the wide variety of different possible signatures for different QSL states. This has lead to a long and arduous search for candidate materials. Such materials include organic and inorganic materials, triangular lattice materials, kagome lattice materials and pyrochlore lattice materials. They may also exhibit gapped or gapless spinon excitations. One material of particular interest is the triangular rare-earth antiferromagnet: $YbMgGaO_4$, which I will discuss in the next section. To identify the QSL characteristics present in a material, researchers must use a wide array of experimental techniques. These techniques include neutron scattering to investigate correlations and low energy spin dynamics in the material and susceptibility measurements to investigate spin fluctuations at low temperatures.

1.4 Introduction to the $YbMgGaO_4$ Crystal System

The triangular rare-earth antiferromagnet $YbMgGaO_4$ has garnered much interest since the successful synthesis of a powder sample in 2015.[14] In this material, the Yb^{3+} ions are confined to triangular lattices in a $\mathbf{R\bar{3}m}$ unit cell symmetry (see Figure 1.5a) with chemically disordered Mg^2+/Ga^{3+} sites in the interlayer regions and a D_{3d} local point group symmetry for the Yb^{3+} ions. While each of the two dimensional triangular lattices differ due to the chemical disorder present in the inter-plane regions, each individual plane is constructed by equilateral triangles and therefore displays no in-plane anisotropy in real space. Many of the QSL candidate materials do not form isotropic triangular lattices and, thus display some form of anisotropic intralayer exchange[15, 16, 17]. Because $YbMgGaO_4$ contains isotropic triangular lattices, no such anisotropic exchange exists within real space in this material. $YbMgGaO_4$ also does not possess significant magnetic defects within the triangular magnetic layers, owing to the extreme chemical differences between Yb^{3+} ions and the non-magnetic ions (Mg^{2+}, Ga^{+3} and O^{2-}). There is also no DM interaction as the inversion center lies on the midpoint between adjacent Yb^{3+} ions and the Yb^{3+} layers are well separated by a collection of non-magnetic Mg^{2+}/Ga^{3+} triangular bipyramids preventing interlayer interactions.[14] $YbMgGaO_4$ also differs from many QSL candidates in that the magnetism is manifested by a magnetic ion that exhibits an effective spin-1/2 due to spin-orbit coupling (SOC) and an odd number of electrons per unit cell.[14]

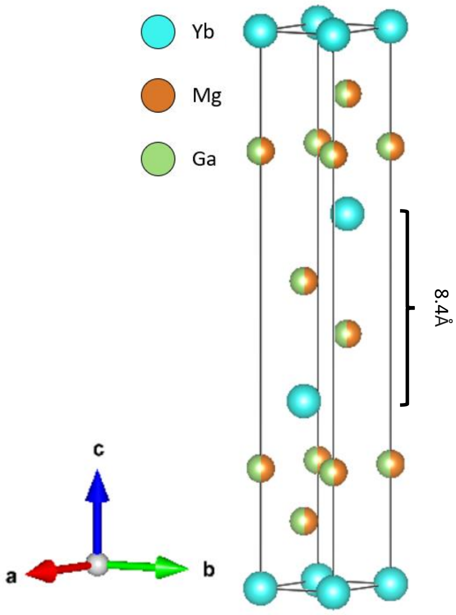

(A) $YbMgGaO_4$ unit cell with oxygen ions omitted. Generated using VESTA.[18]

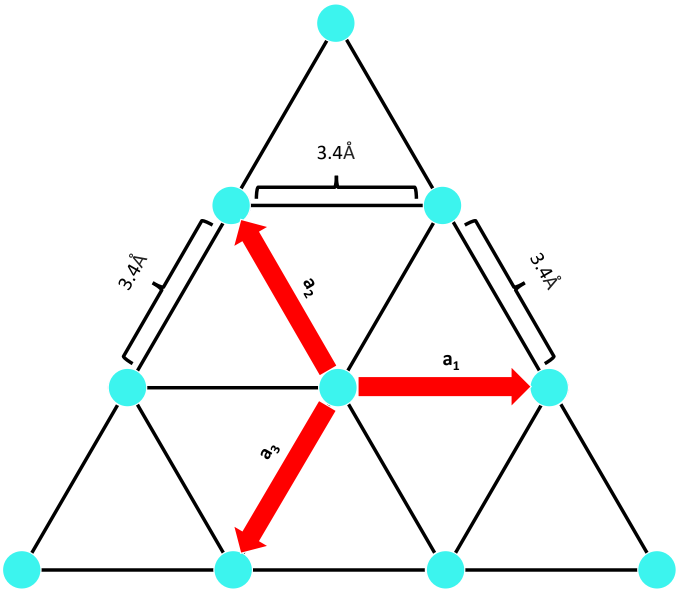

(B) Yb^{3+} triangular planes in $YbMgGaO_4$.

FIGURE 1.5: Crystal structure of $YbMgGaO_4$.

Preliminary characterization on powder samples was performed in [14]. Inverse susceptibility measurements revealed an antiferromagnetic exchange interaction of -4K. This combined with the fact that heat capacity measurements revealed no magnetic transitions down to 60mK, lead the research team to consider the material a QSL candidate but further analysis on single crystals would be a necessity. This was achieved in the same year by Y. Li *et. al.*.[19] Single crystals of various sizes where synthesized using the floating zone synthesis technique. With 13 electrons in the $4f$ orbital, the Yb^{3+} ions have total angular moment $J = 7/2$. Due to the D_{3d} crystal electric field's influence, the $J = 7/2$ eight-fold degenerate manifold is split into four Kramers doublets.[19] They also determined the effective Hamiltonian for the effective spin-1/2 system via a symmetry analysis:

$$\begin{aligned}\mathcal{H} = \sum_{\langle ij\rangle}[J_{zz}S_i^zS_j^z + J_{\pm}(S_i^+S_j^- + S_i^-S_j^+) + J_{\pm\pm}(\gamma_{ij}S_i^+S_j^+ + \gamma_{ij}^*S_i^-S_j^-) \\ - \frac{iJ_{z\pm}}{2}(\gamma_{ij}^*S_i^+S_j^z - \gamma_{ij}S_i^-S_j^z + \langle i \leftrightarrow j\rangle)] \quad (1.34)\end{aligned}$$

where $S_i^{\pm} = \mathrm{S}_i^x \pm +iS_i^y$ and γ_{ij} is a phase factor, who's value is dependant on the direction of the interation (i.e. if the interaction is along ij bonds $\mathbf{a}_1$, $\mathbf{a}_2$ or $\mathbf{a}_3$ in Figure 1.5b). [19] This amounts to an anisotropic spin interaction due to the spin-orbit coupling in the local ground state doublet without the presence of the symmetry-disallowed DM interaction.[19] Li *et. al.* also showed through directionally dependent magnetization, susceptibility and electron spin resonance (ESR) measurements the values of the parrallel and perpendicular components of the anisotropic $g - tensor$ appearing in the Zeeman Hamiltonian, as well as the isotropic and anisotropic exchange couplings in Equation 1.34. The components of the anisotopic $g - tensor$ were found to be: $g_{\perp} = 3.060(4)$ and $g_{\parallel} = 3.721(6)$ thus implying a relatively isotropic magnetic system.[19] The exchange couplings can be found in Table 1.1

In-depth neutron scattering studies have also been conducted on $\mathrm{YbMgGaO}_4$. Cold neutron (neutrons produced on the energy scale of 10K) inelastic scattering

Exchange Coupling	Coupling Strength (K)
J_{zz}	0.98(8)
$J_{\pm}$	0.90(8)
$J_{z\pm}$	0.155(3)
$J_{\pm\pm}$	0.04(8)

TABLE 1.1: Anisotrpic coupling constants in $YbMgGaO_4$ present in Equation 1.34 and as estimated in [19].

experiments performed in [1] and [20] revealed a gapless continuum of scattering extending out of the elastic line at a temperature of 60mK in a 0T applied field (see Figure 1.6a). This continuum is indicative of the hallmark 2D spinons produced in a spin liquid material. Thermal conductivity and specific heat measurements confirm the gapless nature of the spinon excitations observed in the neutron data.[21] Paddison *et. al.* showed that the spinon excitations are robust with temperature (persisiting to temperatures up to 14K) and the material can be fully polarized in a 7.8T applied field. When polarized, $YbMgGaO_4$ exhibits a ferromagnetic ordering, as evidenced by the fitting of the lower bound of the spin wave dispersion in Figure 1.6b to linear spin wave theory.[1] They proposed that this QSL behaviour can be understood when next-nearest-neighbor interaction were considered but further theoretical study shows that nearest-neighbour interactions are sufficient.[22] Paddison *et. al.* also proposed that the chemical disorder plays an important role in the ground state correlations in the system, similar to that in the pyrochlore case.[1, 23]

Due to the ambiguity in the origin of the QSL correlations, further investigation was required. Careful study of results of thermal neutron (neutrons produced with energy on the order of 300K) inelastic scattering experiments revealed the CEF energy eigenvalues of the system.[24] The CEF excitations observed in [24] display broad energy widths, in comparison to the expected sharp excitations that should be limited by the resolution of the instrument. Due to the extended width of the excitations, the randomness present in the unit cell as a product of the chemically disordered Mg^{2+}/Ga^{3+} sites must be playing a significant role. Recent theoretical developments have proposed that when the disorder is removed from the system, Yb^{3+} ions in this structure may enter into an ordered state - a phenomenon coined

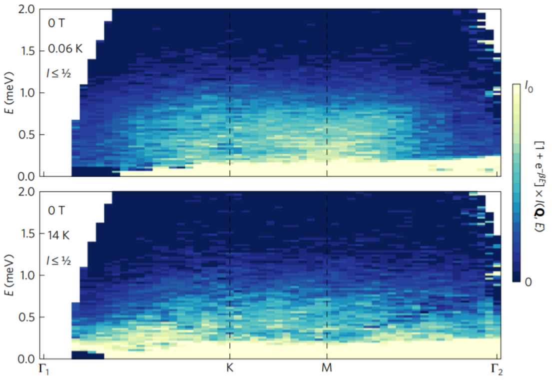

(A) 0T inelastic neutron scattering on a single crystal of $YbMgGaO_4$

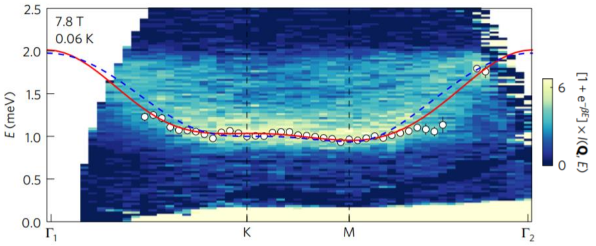

(B) 7.8T inelastic neutron scattering on a single crystal of $YbMgGaO_4$

Figure 1.6: Cold inelastic neutron scattering experiments performed on a single crystal of $YbMgGaO_4$. Adapted with permission from Springer Nature: Nature Physics [1]. ©

"disorder-induced spin liquid mimicry".[25, 26] Whether or not the disorder is the driving force for the QSL-like spin correlations in $YbMgGaO_4$ still remains to be settled.

1.5 Purpose of this Work

This thesis work seeks to examine the question as to whether $YbMgGaO_4$ is an intrinsic QSL candidate or a disorder-induced QSL. To do that, I will present the synthesis and characterization of two related crystal systems: $Ba_6Yb_2Ti_4O_{17}$ (Figure 1.7a) and $ErMgGaO_4$ (Figure 1.7b). Like, $YbMgGaO_4$, $ErMgGaO_4$ and $Ba_6Yb_2Ti_4O_{17}$ have the magnetic rare-earth ions confined within 2D triangular lattices interspersed throughout the unit cell. In $Ba_6Yb_2Ti_4O_{17}$, the disorder has been completely removed from the system. The nonmagnetic Ba^{2+} and Ti^{4+} ions are sufficiently chemically different and no site mixing is possible with a crystal space group symmetry of **P63/mmc**. Thus, synthesis and characterization of $Ba_6Yb_2Ti_4O_{17}$ is critical to the estimation of the effects chemical disorder has on the ground state in $YbMgGaO_4$. Should QSL correlations be present in $Ba_6Yb_2Ti_4O_{17}$, one would assume that the QSL behaviour is intrinsic to the Yb^{3+} triangular planes. Prior to this work, successful synthesis of $Ba_6Yb_2Ti_4O_{17}$ has yet to be reported. One of the aims of this work was to determined an optimal synthesis procedure, confirm phase purity via powder X-Ray diffraction, perform preliminary neutron scattering experiments and low temperature susceptibility measurements. From this investigation, the ground state of $Ba_6Yb_2Ti_4O_{17}$ will be classified.

$ErMgGaO_4$, however, crystallizes in the same structure as $YbMgGaO_4$. The changing of the magnetic ion may change the spin anisotropy in the system. Indeed, point charge calculations for Er^{3+} in ErMgGaO4 predict an Ising-like Er^{3+} magnetic moment.[27] Thus, one would expect the ground state physics in the system to display different characteristics. Susceptibility and μSR measurements on single crystals show a predominately QSL like character but this is not presently known with certainty.[27, 28] The single crystals synthesized prior to this work contain a nominal amount of a magnetic impurity; that being $Er_3Ga_5O_{12}$. $Er_3Ga_5O_{12}$

crystallizes in a garnet cubic structure and displays a spin glass transition at temperatures of approximately 0.8K in a 40Oe applied magnetic field.[29] Because of the presence of such an impurity, the ground state of the material has yet to be characterized. It is therefore imperative that pure $ErMgGaO_4$ be synthesized and characterized to complete the study and compare with the findings in $YbMgGaO_4$.

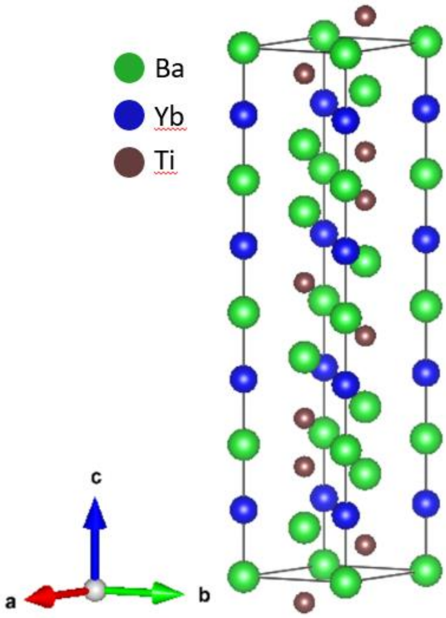

(A) $Ba_6Yb_2Ti_4O_{17}$ unit cell

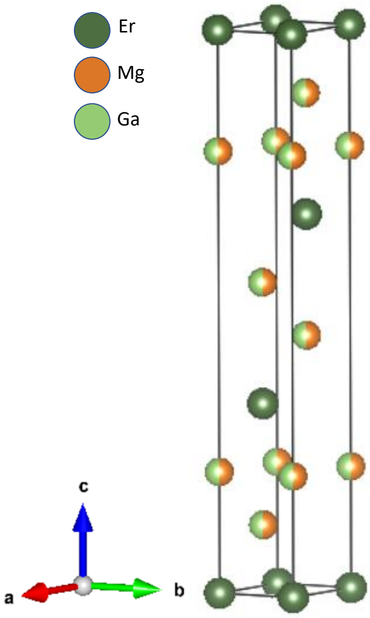

(B) $ErMgGaO_4$ unit cell

Figure 1.7: Unit cells for the materials investigated in this work. Generated using VESTA software.[18] Oxygen ions have once again been omitted.

Chapter 2

Materials and Methodology

With a foundation built on the pertinent physical concepts related to geometrically frustrated quantum magnets, I will now turn my attention to the methodology used in this thesis work to investigate these systems. I will begin by describing the synthesis procedures for both materials introduced in chapter 1 followed by the experimental techniques used to characterize the resultant samples. I will discuss powder X-Ray diffraction, SQUID magnetometry as it relates to temperature dependent susceptibility measurements as well as the method used to perform theoretical point charge CEF calculations on $Ba_6Yb_2Ti_4O_{17}$.

2.1 Materials Preparation

2.1.1 Powder Synthesis

To the best of my knowledge, successful $Ba_6Yb_2Ti_4O_{17}$ powder synthesis has yet to be reported in the literature. As such, the synthesis process was, by and large, a trial and error approach, until the optimal recipe was discovered. The starting materials $BaCO_3$, Yb_2O_3 and TiO_2 were first placed in a drying furnace held a temperature of 200°C for 24h prior to mixing, to remove any water the powders may have absorbed. The powders were then mixed using an agate mortar and pestle, adhering to the appropriate stoichiometry. Once well mixed by hand, the powders were poured into a Nalgene bottle containing yttrium stabilized zirconia beads and ball milled for 3h to ensure homogeneity. Preliminary powder synthesis trials were conducted using an alumina crucible in a 1350-1400°C air environment.

Trails were conducted over various lengths of time ranging from 48h to 7 days of annealing. Subsequent attempts made use of a 1500°C air environment furnace for durations of 48 to 72h. The results of the material preparation experiments were subject to powder X-Ray diffraction measurements to determine the sample composition.

The procedure for synthesizing $ErMgGaO_4$ has been well established at McMaster University. Due to the proximity of the materials composition to that of $Er_3Ga_5O_{12}$ (a magnetic material with a garnet crystal structure), synthesis of phase pure powder material is difficult by conventional means (eg. those employed in the synthesis of $Ba_6Yb_2Ti_4O_{17}$).[27, 28] When starting materials of Er_2O_3, Ga_2O_3 and MgO are reacted, the Er_2O_3 and Ga_2O_3 have a tendency to forgo the presence of the MgO entirely and form in the garnet phase. Because the garnet phase exhibits a spin glass transition,[29] it can make the magnetic characterization the ground state of $ErMgGaO_4$ difficult. It is, therefore, imperative that the material be synthesized such that the amount of garnet present in the sample is at a minimum. As such, one must by-pass attempts at powder synthesis and go immediately to the formation of single crystals. A single crystal growth attempt is advantageous to overcome these issues, as it provides extra control over how much impurity is present, and where it may manifest in the bulk of the material. This was done using floating zone optical image synthesis technique.

2.1.2 Synthesis by Floating Zone Optical Image Furnace Techniques

Floating Zone Synthesis (FZS) is not an new idea. In fact, it has been used with great success to produce high quality, large single crystals of a variety of novel metal and rare-earth oxides in the past. This technique makes use of a floating zone optical image furnace (Figure 2.1). The halogen or xenon lamps are powered via computer control, thus allowing the user to change the heat being supplied to the growth. The light from the lamps is incident on ellipsoidal mirrors whose common focii direct the light to the well centred hot zone. The sample is comprised of a "feed" and "seed" rod. To begin the growth, the feed and seed rods are held close to the centre of the focused hot zone and the power output of the lamps is increased slowly. When the feed and seed rods begin to show signs of melting (i.e. they become glossy), the left and right rotation control is triggered by the user. This ensures a uniform heating of both rods. When the tips of the rods appear molten, the feed rod is lowered onto the seed and the molten zone is created (being held together by surface tension). The feed rod's rotation is then switched to the opposite direction of that of the seed and the automatic lowering speeds of both rods are engaged. With the seed rod being lowered, the molten material is being pulled out of the hot zone and slowly cooled, thus hopefully creating a single crystal crystallization front. More material is supplied by the feed rod as it is lowered through the hot zone to keep the amount of molten material constant. All of this is performed within a transparent quartz tube which allows the user to perform the technique in a variety of gas environments (ranging from vacuum to 10 atmospheres of argon or oxygen, for example).

FZS is particularly useful in crystal growth due to the control the crystal grower has over the growth conditions. The user has control over growth speed, seed rod speed, rod rotation, temperature via the lamp power control and the growth environment all in real time. It is therefore possible to determine the optimal conditions for single crystal synthesis for the given material. All this is contingent on how well the experiment is set up. Rods should have a uniform density throughout their length. If this is not the case, then the amount of power required to melt the material could change depending on how much material is in the zone. The rods should also be packed tightly to prevent air bubbles. The air bubbles could burst when passing through the molten zone and, as a result, could destroy the zone entirely. To combat this, rods are prepared as cylinders, typically of dimensions 0.5cm in diameter and 10cm in length. They are packed using a hydro-static press under a pressure of 60MPa for 20 minutes, then sintered at temperatures of 1200°C to 1350°C to harden. They are then aligned in the centre of the optical image furnace to ensure that no additional stress will be placed on the zone from misalignment.

Because the rods of polycrystalline material are only in contact with the gas environment of the growth, so too is the molten zone. This allows for an extremely pure synthesis as there is nowhere for impurities to be introduced from

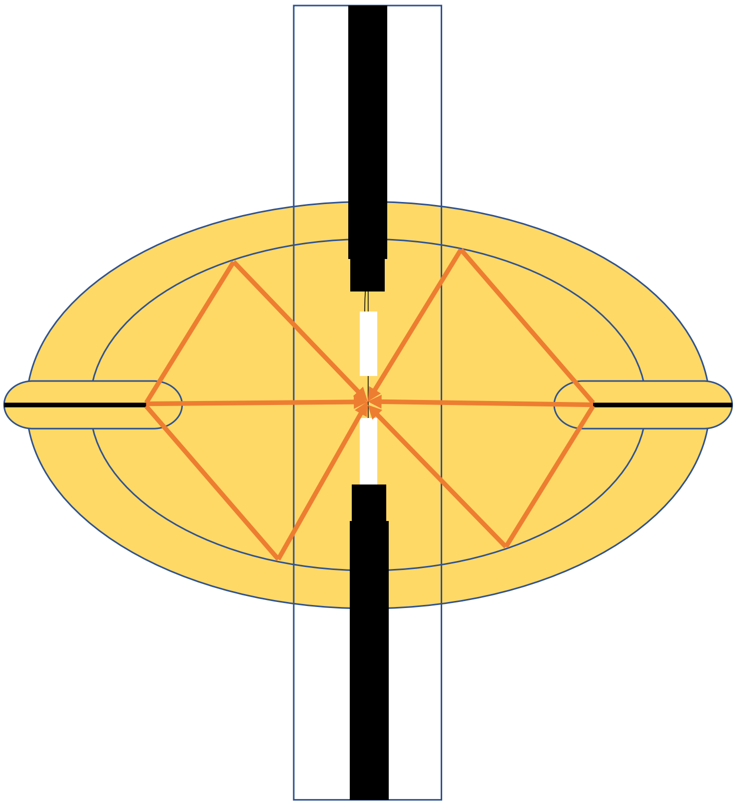

Figure 2.1: Cross-sectional view of an floating zone optical image furnace.

(as there would be for a growth using a crucible). This, along with the length of the polycrystalline seed and feed rods can result in a phase pure single crystal of considerable size (upwards of a few grams in mass and 3-6cm in length). Rods of this size are required to perform single crystal neutron scattering experiments due to the relative weakness of how the neutron interacts with matter. The floating zone technique is not without its draw backs, however. Because it requires a stable zone, if the material melts incongruently or the molten zone has a low viscosity, FZS may not produce single crystals as the molten material will have a tendency to "spill over" the sides of the seed rod. It is also not well suited for a material that is particularly volatile. If the material evaporates quickly, the residue will build up on the inside of the tube, blocking the light from reaching the hot zone and effectively lowering the temperature of the zone. If these issues are not present, and the user performs a good growth, then one can verify the resulting single crystal nature via Laue X-ray diffraction or by performing a neutron pole figure. Phase purity can be verified by grinding a small piece (20-50mg) into a powder and performing a powder X-ray diffraction experiment. Two optical image furnaces developed by Nippon Electric Co. (NEC) at McMaster University in the Brookhouse Institute for Materials Research laboratories were used in the completion of this work.

2.1.3 X-ray Diffraction

Prior to discussing X-ray diffraction, it is useful to recall the definition of the reciprocal lattice, **G**. If one assumes a crystal of material comprising of ion's whose positions can be described by Bravais lattice vectors given by:

$$\mathbf{R} = n_1\mathbf{a}_1 + n_2\mathbf{a}_2 + n_3\mathbf{a}_3 \tag{2.1}$$

where n_i are integers and $\mathbf{a}_i$ are the bases vectors forming the lattice. Using this construction of the atomic positions, one can then construct a reciprocal lattice, **G**, of the form:

$$\mathbf{G} = h\mathbf{b}_1 + k\mathbf{b}_2 + l\mathbf{b}_3 \tag{2.2}$$

where h, k, and l are known as the Miller Indices and $\mathbf{b}_i$ are related to $\mathbf{a}_i$ through the following relations:

$$\mathbf{b}_1 = 2\pi\frac{\mathbf{a}_2 \times \mathbf{a}_3}{V}, \mathbf{b}_2 = 2\pi\frac{\mathbf{a}_3 \times \mathbf{a}_1}{V}, \mathbf{b}_3 = 2\pi\frac{\mathbf{a}_1 \times \mathbf{a}_2}{V} \tag{2.3}$$

and:

$$\mathbf{b}_i \cdot \mathbf{a}_j = 2\pi\delta_{ij} \tag{2.4}$$

where $V = \mathbf{a}_1 \cdot (\mathbf{a}_2 \times \mathbf{a}_3)$. Defining the reciprocal lattice as such is important as research techniques such as X-ray scattering are discussed in terms of the reciprocal lattice (for example, the peak intensities observed in the scattering profile a related to specific hkl values allowed for the given crystal system).

X-ray diffraction (XRD) is a useful experimental tool for determining phase purity of a material. If one considers a beam of X-rays traveling in a direction $\hat{\boldsymbol{n}}$ with wavelength λ and wavevector $\mathbf{k}$ incident on two ions separated by a vector $\mathbf{d}$, then a beam of scattered X-rays (with wavevector $\mathbf{k}$' along $\hat{\boldsymbol{n}}$') will be observed provided the incident rays interfere constructively.[7] The condition for constructive interference is the path difference between photons scattered from the atoms must be an integer number of wavelengths of the incident X-rays. This path difference is given by:

$$d\cos(\theta) + d\cos(\theta') = \mathbf{d} \cdot (\hat{\boldsymbol{n}} - \hat{\boldsymbol{n}}') \tag{2.5}$$

where θ and θ' are the angles subtended by the incident photons and scattered photons to vector $\mathbf{d}$ respectively. From the condition for constructive interference and Equation 2.5, the path difference can be rewritten as:

$$\mathbf{d} \cdot (\hat{\boldsymbol{n}} - \hat{\boldsymbol{n}}') = m\lambda \tag{2.6}$$

where m is an integer. If one then relaxes the constraint of two scattering sites to a system of scattering sites displaced from one another by a Bravais lattice vector $\mathbf{R}$, then Equation 2.6 becomes:

$$\mathbf{R} \cdot (\mathbf{k} - \mathbf{k}') = 2\pi m \tag{2.7}$$

given that $\mathbf{k} = 2\pi\hat{\boldsymbol{n}}/\lambda$. This condition is equivalent to the definition of the reciprocal lattice vector, $\mathbf{G}$, thus implying that constructive interference will occur when:

$$\mathbf{G} = \mathbf{k}' - \mathbf{k} \tag{2.8}$$

and when the tip of $\mathbf{k}$ touches a plane that bisects $\mathbf{G}$ between the origin and the reciprocal lattice point defined by $\mathbf{G}$. Such a construction is known as the "Laue Construction".[7] If one assumes the scattering system to act as a mirror, and each plane of atoms in the system to be separated by a distance d, then given that the magnitude of the reciprocal lattice is given by $|\mathrm{G}| = 2\pi/d$, on arrives at the result:

$$k\sin\theta = \frac{\pi n}{d} \tag{2.9}$$

where k is the magnitude of the incident wave vector, θ is the angle subtended by the incident X-rays and the material and n is an integer. By substituting $k = 2\pi/\lambda$, Equation 2.9 becomes:

$$2d\sin\theta = n\lambda \tag{2.10}$$

which is the celebrated Bragg's Law (see Figure 2.2a for a schematic representation of Bragg scattering).

In general, $\mathbf{k}$ will not satisfy the above conditions. As such, if one were to attempt to an X-ray scattering experiment with $\mathbf{k}$ fixed, one would see no constructive interference at all. In practice, one must either vary the incident wavelength or the incident direction to observe interference peaks. Changing the incident direction is typically performed by rotating the single crystal sample. The reciprocal lattice then rotates about that axis of rotation and will eventually satisfy the condition for constructive interference. In principle, a powder X-ray diffraction experiment produces a similar outcome, with the added caveat that the incident direction is now averaged over all possible orientations (this is due to the fact that a polycrystalline powder can be considered as a large collection of randomly oriented single crystal grains). In modern powder diffraction experiments, the direction of the incident beam is fixed, the powder is rotated within the plane defined by the incident and scattered X-ray beam by an angle θ and the detector arm is rotated an angle 2θ with respect to the incident beam. This will allow the scattering to occur as a reflection from the material provided the angles satisfy the Bragg conditions for the given crystal system. For specific angles, the detector arm will register sharp peaks in intensity (show in Figure 2.2). These angles are determined by the crystal structure and can be used to refine the lattice parameters of the material, as well as the volume fraction of the impurity phases present in the sample. This is typically done via a Rietveld refinement. For this work, the Panalyical X'celerator was used to perform XRD experiments. The resultant diffraction pattern was analyzed using the FullProf Suite software. This reflection approach is advantageous as it limits the amount of absorption occurring in the experiment.

2.2 SQUID Magnetometry

The Superconducting QUantum Interference Device is piece of experimental equipment that is a mainstay in many condensed matter physics laboratories. The device is constructed with consideration of the Josephson Effect. In BCS theory, when a material enters a superconducting phase, electrons near the Fermi surface are able to pair with one another and become a quasi particle known as a Cooper pair.[7] B. D. Josephson showed that if a two materials in a superconducting phase are separated by a thin non-superconducting material, Cooper pairs may still be able to quantum mechanically tunnel through the barrier, thus preserving a supercurrent.[30] He showed that the Ginzberg-Landau order parameter

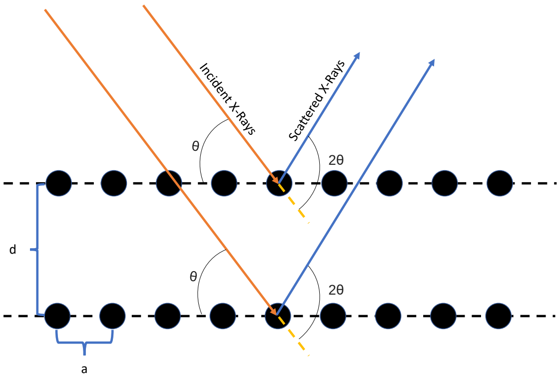

(A) X-ray scattering for a series of lattice planes

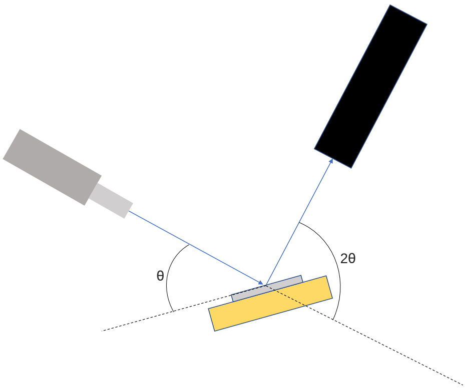

(B) Schematic diagram of a powder X-ray diffraction experiment.

FIGURE 2.2: Illustration of X-ray diffraction geometries.

describing the superconducting phase of one of the superconductors must related to the order parameter of the other superconductor by a phase shift. Josephson then concluded that, in the presence of a magnetic field, the supercurrent passing through the aforementioned loop would be modulated by a factor of sin($\Delta\theta$ - $\frac{\pi\Phi}{\Phi_0}$), where Φ is the magnetic flux present in the loop, Φ_0 is the fundamental flux quanta and $\Delta\theta$ is the phase shift.

The SQUID uses this principle to conduct ultra sensitive magnetic measurements to determine the magnetic moment of the measured sample. In principle, there are two kinds of SQUID magnetometers available, the DC SQUID and the RF SQUID. The DC SQUID consists of two Josephson Junctions in parallel coupled to a pick up loop. The two circuits are coupled by the external magnetic flux felt by the junction. When a static field is applied within the pick up loop, the movement of the sample causes an induced current due to the magnetic flux produced by the sample's translation. The current within the superconducting loop will oscillate with period, Φ_0, the fundamental flux quanta, due to the DC Josephson Effect. Here, the total current in within the loop is given by[31]:

$$I = I_{c1}\text{sin}(\Delta\theta_1) + I_{c2}\text{sin}(\Delta\theta_2) \tag{2.11}$$

where I_{ci} is the current within each part of the loop and $\Delta\theta_i$ is the phase difference in each junction. If on assumes a balanced SQUID loop, then $\Delta\theta_1$=$\Delta\theta + \frac{\pi\Phi}{\Phi_0}$ and $\Delta\theta_2$=$\Delta\theta - \frac{\pi\Phi}{\Phi_0}$. Equation 2.11 then becomes:

$$I = 2I_c\text{sin}(\Delta\theta)\text{cos}\left(\frac{\pi\Phi}{\Phi_0}\right) \tag{2.12}$$

A bias current must applied to the device. The instrument detects the voltage output from the device as [32]:

$$V = \frac{R}{2}\sqrt{I_b^2 - 2I_c\text{cos}\left(\frac{\pi\Phi}{\Phi_0}\right)} \tag{2.13}$$

where R is the resistance of the junctions, I_b is the bias current.

The RF SQUID functions in a different way. Here, instead of two Josephson junctions, the RF SQUID requires only one. The superconducting loop is coupled to a circuit that is now being driven by an RF current. This loop now experiences an external magnetic flux, Φ_{ex} of:

$$\Phi_{ex} = \Phi_{sample} + \Phi_{RF} \tag{2.14}$$

where Φ_{sample} and Φ_{RF} are the resultant fluxes for the sample and RF circuit, respectively. This is not, however, the total magnetic flux, Φ_{total} measured as one must always take into account the inductance, L, from the loop. Keeping this in mind, and that phase difference between the current in the superconducting loop must be integer numbers of 2π, on arrives at a self consistent result for the total measured flux:

$$\Phi_{total} = \Phi_{ex} - LI_0 \mathrm{sin}\left(\frac{2\pi\Phi_{total}}{\Phi_0}\right) \tag{2.15}$$

Thus, as the AC current oscillates, one can measure the difference between the total magnetic flux and the known RF magnetic flux to determine the magnetic susceptibility of the sample. The SQUID used in this work is the Quantum Design MPMS XL-3 RF magnetometer with He-3 and He-4 inserts. The susceptibility is reported in units of emu g^{-1} G^{-1}.

2.3 Theoretical Point Charge Calculations of Crystalline Electric Field Eigenvalues and Eigenvectors

Theoretical point charge calculations were performed to estimate the four crystal electric field doublets present in $Ba_6Yb_2Ti_4O_{17}$ ($J = 7/2$ in $Ba_6Yb_2Ti_4O_{17}$ so there must be four doublets as $2J+1=8$). This was done using novel Python software developed by Allen Scheie at Oak Ridge National Laboratories called PyCrystalField.py.[33] The program imports a crystal structure .cif file (generated using VESTA or some other crystal structure visualization tool) and uses the allowed symmetries to perform the calculations (outlined in subsection 1.1.1) for the magnetic ion in the material. It is also capable of using the ground state wavefunction it produces to determine the anisotropic g-tensor (i.e. how well the magnetic field couples to the x, y and z components of the magnetic moment). If one recalls the definition of the Zeeman contribution to the magnetic Hamiltonian:

$$\mathcal{H} = \mu_B \mathbf{H} \cdot g \cdot \mathbf{J} \tag{2.16}$$

where the anisotropic g-tensor g is defined as:

$$g = \begin{bmatrix} g_{xx} & g_{xy} & g_{xz} \\ g_{yx} & g_{yy} & g_{yz} \\ g_{zx} & g_{zy} & g_{zz} \end{bmatrix} \tag{2.17}$$

the components of which are calculated by $g_{zz} = 2\langle +|J_z|+\rangle$ and $g_{zx} + ig_{zy} = 2\langle +|J_z|-\rangle$ for each of the three directions. In principle it is possible to rotate the local environment such that all only diagonal terms appear. The program does this and outputs the matrix form of the tensor.

To use the program, all one needs is the appropriate .cif file and a Python compiler. To run the software, the user must import "PyCrystalField.py" as well as the numpy library. The user can then call the module "importCIF" taking the name of the .cif file and the magnetic ion of interest as arguments. This allows the user to call the "printEigenvectors" function. This module will then print the CEF coefficients (i.e. the B_n^m's), the orientation of the local environment the program has chosen to reduce the number of coefficients required to simplify the Hamiltonian and finally the eigenfunctions and the corresponding energies. Subsequently, the anisotropic g-tensor is estimated by calling the "g_tensor" function. This function takes the ground-state doublet produced by the "printEigenvectors" function and calculates the g-tensor in the form of Equation 2.17.

Chapter 3

Introduction to Neutron Scattering

In this chapter, I will discuss one of the most important and versatile tools a condensed matter researcher has in their tool box; neutron scattering. I will begin with a brief discussion of the fundamental properties of the neutron and why those properties lead to a uniquely useful probe to investigating matter. I will then discuss some of the intricacies of neutron scattering itself and finish with a description of the instruments used to investigate the ground state and low energy excitations in $Ba_6Yb_2Ti_4O_{17}$ and $ErMgGaO_4$. More details on the theory of neutron scattering can be found in [6].

3.1 Fundamental Properties of the Neutron

Neutrons are one of the three constituent particles in atoms. It is unique in that it carries a charge of zero and that its mass is such that the de Broglie wavelength for thermal neutrons (energy 300K/k_B) is on the order of atomic distances in materials. As such, interference effects are possible when neutrons scatter from condensed matter. The fundamental properties of the neutron are listed in Table 3.1.

The de Broglie wavelength allows the neutron to be scattered from the structure of the material, in a manner similar to that to that of X-Rays. Where they differ is in the fact that the neutron is scattering due to the strong nuclear interaction with

mass, m_n	1.675×10^{-27}kg
charge	0
spin	$\frac{1}{2}$
magnetic dipole moment, μ_n	-1.913μ_N

TABLE 3.1: Fundamental properties of the neutron. Taken from [6]. Here, μ_N is the nuclear magnetic moment.

nuclei as opposed the electric field of the X-ray interacting with the electron cloud in atoms. In fact, the neutron can also interact with the electron cloud associated with magnetic electrons in solids, by virtue of its spin-1/2 magnetic moment. Because the neutron is uncharged, it is not scattered by the electron cloud directly and it can be much more sensitive to light atoms, such as hydrogen and oxygen, as it is scattering off of their nuclei. As already mentioned, due to the spin-1/2 nature of the neutron, it is also capable of discerning the magnetic properties of the investigated material as the dipole moment of the neutron will couple to the dipole moment of the unpaired electrons in the system. When scattered elastically, the neutron will provided information on the nuclear and magnetic structures of materials. When scattered inelastically, the neutron will elucidate magnetic and structural excitations within the material.

3.2 Neutron Production

Because the neutron interacts relatively weakly with matter, a large neutron flux incident on the sample of interest is required for most neutron scattering studies of materials. This is typically done using either a neutron reactor or a spallation neutron source as the source of neutrons (in principle, there are small linear neutron producing devices but, as they are still in the development process, I will omit these from the discussion). A reactor source provides a continuous source of neutrons. In a reactor, the fuels rods are typically comprised of uranium full rods containing approximately 20% ^{235}U. The ^{235}U nuclei undergo a chain nuclear reaction in which a neutron is captured by the ^{235}U nucleus. The new ^{236}U nucleus is unstable and immediately splits into two lighter elements plus several neutrons. The fuel rods are contained in a moderator tank that moderates the energies of the resulting neutrons so that they may be moderated to thermal energies and used in neutron scattering experiments, as well as to keep the chain reaction going, as only thermal neutrons can be efficiently absorbed by the ^{235}U (the moderator is typically heavy water, H_3O, or water). A spallation neutron source on the other hand typically uses accelerated protons incident on a liquid heavy metal target. The proton bombardment of the heavy metal target causes the compound nucleus to eject 20-30 neutrons/protons. The typical spallation source makes use of a proton track that is of the order of km in length before the protons reach the accelerator ring that is a couple hundred meters in diameter. The accelerator ring then produces a pulse of protons with the same energy to bombard the heavy metal target. Due to the size and the amount of energy and manpower required to run these sources, they are expensive to manage. As such, there are a handful of dedicated facilities around the world at which neutron scattering experiments are performed.

Whether the source provides a continuous source of neutrons from as a product of a nuclear reaction within uranium fuel rods (reactor) or the bombardment of a heavy metal target with protons that can be either continuous or in a modulated time structure (spallation), the produced neutron velocities after moderation can be well defined by a Maxwellian distribution. If the neutron is moderated by only the the liquid in the moderator tank than the energy corresponding to the root-mean-squared velocity of the outgoing neutrons is on the order of 300K (it is a common convention to regard the energy of neutrons as a temperature given that $E = k_BT$). These are known as thermal neutrons. In both spallation and reactor neutron production, the neutrons are emitted in all directions. Neutrons that are incident on the beam-line (that is, the port of the containment apparatus that leads to the instrument being used) will be directed toward the instrument via a beam tube. The thermal neutrons will give the user access to information pertaining to structural and magnetic excitations on the order of 10-100meV. Should lower energy excitations be of interest, then an additional moderator (usually liquid hydrogen) is used to moderate the neutron energy further to 25K. This will provide information to excitations on the order of 0.1-10meV. The neutron scattering instruments used in this work make use of reactor sources at the National Institute of Standards and Technology (NIST) in Gaithersburg, Maryland, USA and IN6 at the Institut Laue-Langevin (ILL) in Grenoble, France. I will discuss these instruments shortly.

3.3 Neutron Scattering Length and Neutron Scattering Cross Section

Before getting into the details of nuclear scattering, one must develop the concept of the scattering cross-section. The scattering cross-section, σ_{tot} is defined as the total number of neutrons scattered by the scattering system (i.e the sample) per second divided by the incident neutron flux, Φ. If one considers a beam of monochromatic neutrons incident on a scattering system with a neutron counter that is far away from the scattering system that counts neutrons with energy between E' and $E' + dE'$, then one can define the *partial differential scattering cross-section* as :[6]

$$\frac{d^2\sigma}{d\Omega dE'} = (\text{number of neutrons scattered into solid angle } d\Omega \text{ with energy between } E\text{' and } E\text{' } + dE\text{'})/\Phi d\Omega dE' \quad (3.1)$$

If one assumes an axially symmetric scattered collection of neutrons then, when Equation 3.1 is integrated twice (once with respect to E' and again with respect to Ω) then one can write σ_{tot} as:

$$\sigma_{tot} = \int_0^\pi \frac{d\sigma}{d\Omega} 2\pi \text{sin}\theta d\theta \quad (3.2)$$

The above definition has units of [area] so it would be natural to define a quantity known as the neutron scattering length. Consider a single fixed nucleus as the scattering system and incident neutrons with wavevector $\mathbf{k}$ directed along the z-axis. The wavefunction of such a beam is given by:

$$\psi_n = \exp(ikz) \quad (3.3)$$

Because the wave length of thermal and cold neutrons is on the order of 10^{-10}m and the extent of the nuclear force is only 10^{-14}-10^{-15}m, the wavefunction of the scattered neutron can be treated as spherically symmetric.[6] The wave function of the scattered neutrons is therefore given by:

$$\psi_{sc} = -\frac{b}{r}\exp(ikr) \tag{3.4}$$

where b is known as the scattering length and is independent of θ and ϕ. This constant various greatly, and randomly, across the periodic table as the periodic table. Some of the systematics of the variation of b with nucleon can be predicted, but detailed neutron scattering lengths are hard to predict from first principles and scattering lengths must be experimentally determined. Using this construction, the total scattering cross-section from a single nucleus is given by:

$$\sigma_{tot} = 4\pi b^2 \tag{3.5}$$

The details of the calculation leading to Equation 3.5 can be found in [6].

This of course becomes more complicated when one extends the above to a system of multiple atoms at positions $\mathbf{R}_j$ relative to an arbitrary origin scattering a beam of neutrons with incident wavevector $\mathbf{k}$. If the neutrons and the scattering system are in initial states ψ_k and χ_λ respectively, then the interaction potential V will serve to transition the neutrons and the scattering system to states $\psi_{k'}$ and $\chi_{\lambda'}$. If one assumes that the neutron cannot impart kinetic energy to the nucleus, the scattering will be entirely elastic. This means that the energy of the outgoing neutrons and the scattering system after a scattering event must be the same as the incident neutrons and the scattering system prior to a scattering event. As such the energy transition can be represented as a Dirac δ-function and the partial differential scattering cross-section can be represented as follows:

$$\left(\frac{d^2\sigma}{d\Omega dE'}\right)_{\lambda\rightarrow\lambda'} = \frac{k'}{k}\left(\frac{m}{2\pi\hbar^2}\right)^2 |\langle \mathbf{k}'\lambda'|V|\mathbf{k}\lambda\rangle|^2 \delta(E_\lambda - E_{\lambda'} + E - E') \tag{3.6}$$

where I have invoked Fermi's Golden Rule to describe the transition from one state to another. If one uses the Fermi Pseudopotential (that is a potential of the form $V_j = \frac{2\pi\hbar^2}{m} b_j$), then one can write Equation 3.6 as:[6]

$$\frac{d^2\sigma}{d\Omega dE'} = \frac{k'}{k}\frac{1}{2\pi\hbar}\sum_{jj'} b_j b'_j \int_{-\infty}^{\infty} \langle \exp(-i\boldsymbol{\kappa}\cdot\mathbf{R}_{j'}(0))\exp(i\boldsymbol{\kappa}\cdot\mathbf{R}_j(t))\rangle \exp(i\omega t)dt \tag{3.7}$$

where $\boldsymbol{\kappa} = \mathbf{k} - \mathbf{k}'$ (called the scattering vector) and $b_{j,j'}$ are the scattering lengths for the j^{th} and j^{th}' atoms in the scattering system. If one further assumes that the scattering system is comprised of several atoms each with several different isotopes, each with different scattering lengths then one can represent $b_j b_{j'}$ as $(\bar{b})^2$ for $j \neq j'$ or $\bar{b^2}$ for $j = j'$.[6] This then changes the form of Equation 3.7 to the form:

$$\begin{aligned}\frac{d^2\sigma}{d\Omega dE'} = &\frac{k'}{k}\frac{1}{2\pi\hbar}\frac{\sigma_{coh}}{4\pi}\sum_{jj'}\int_{-\infty}^{\infty} \langle \exp(-i\boldsymbol{\kappa}\cdot\mathbf{R}_{j'}(0))\exp(i\boldsymbol{\kappa}\cdot\mathbf{R}_j(t))\rangle \exp(i\omega t)dt \\ &+ \frac{k'}{k}\frac{1}{2\pi\hbar}\frac{\sigma_{inc}}{4\pi}\sum_{j}\int_{-\infty}^{\infty} \langle \exp(-i\boldsymbol{\kappa}\cdot\mathbf{R}_{j}(0))\exp(i\boldsymbol{\kappa}\cdot\mathbf{R}_j(t))\rangle \exp(i\omega t)dt\end{aligned} \tag{3.8}$$

where:

$$\sigma_{coh} = 4\pi(\bar{b})^2 \tag{3.9}$$

$$\sigma_{inc} = 4\pi(\bar{b^2} - (\bar{b})^2) \tag{3.10}$$

are the coherent scattering cross-section and the in coherent scattering cross-section (i.e. the scattering cross-section corresponding to scattering from the same atom at the same position at different times and the scattering cross-section corresponding to scattering of different nuclei at different times) respectively. Coherent scattering leads to interference effects and is dependent on the mean neutron scattering length while incoherent does not produce interference effects and depends on variations away from the mean neutron scattering length.

3.4 Structural Neutron Scattering By Crystals

The calculations necessary to define scattering from crystal structures are quite long an cumbersome. I will, therefore, refer the interested reader to ref. [6] for the finer details. In this section, I will limit myself to reporting the more important results of the previously mentioned calculations; the first being that of the emergence of Bragg's Law once again.

When on considers a crystal lattice, one typically defines the position of the constituent parts as:

$$\mathbf{R}_j = \mathbf{l}_j + \mathbf{u}_j(t) \tag{3.11}$$

where $\mathbf{l}_j$ is the lattice vector defined in the usual way for the atom and $\mathbf{u}_j(\mathrm{t})$ is the time-dependent displacement of the atom from $\mathbf{l}_j$. If one assumes the interatomic forces to be harmonic, then $\mathbf{u}_j(\mathrm{t})$ can be defined by a set of normal modes:

$$\mathbf{u}_j(t) = \left(\frac{\hbar}{2MN}\right)^{1/2} \sum_{\mathbf{q},p} \frac{\mathbf{e}_{\mathbf{q},p}}{\sqrt{\omega_{\mathbf{q},p}}} [a_{\mathbf{q},p}\mathrm{exp}(i\mathbf{q}\cdot\mathbf{l}_j) + a^{+}_{\mathbf{q},p}\mathrm{exp}(-i\mathbf{q}\cdot\mathbf{l}_j)] \tag{3.12}$$

where p is the polarization index (p=1, 2, 3), $\mathbf{q}$ is the wavevector of the normal mode, $\omega_{\mathbf{q},p}$ is the frequency of the normal mode and $a_{\mathbf{q},j}$ and $a^{+}_{\mathbf{q},j}$ are the annihilation and creation operators of the harmonic oscillator. M is the mass of the atoms (assumed to be all the same for simplicity), $\mathbf{e}_{\mathbf{q},p}$ is the polarization vector of the normal mode and N is the number of values $\mathbf{q}$ can take within the 1^{st} Brillioun Zone. To determine the structural coherent scattering, one must substitute

Equation 3.12 into the first term appearing in Equation 3.8. The coherent partial differential cross section then becomes[6]:

$$\left(\frac{d^2\sigma}{d\Omega dE'}\right)_{coh} = \frac{\sigma_{coh}}{4\pi}\frac{k'}{k}\frac{N}{2\pi\hbar}\sum_j \exp(i\boldsymbol{\kappa}\cdot\mathbf{l}_j)\int_{-\infty}^{\infty}\langle \exp U \exp V\rangle \exp(-i\omega t)dt \tag{3.13}$$

where:

$$U = -i\boldsymbol{\kappa}\cdot\mathbf{u}_0(0) = -i\sum_{\mathbf{q},p}(g_{\mathbf{q},p}a_{\mathbf{q},p} + g_{\mathbf{q},p}a^{+}_{\mathbf{q},p}) \tag{3.14}$$

$$V = i\boldsymbol{\kappa}\cdot\mathbf{u}_j(t) = i\sum_{\mathbf{q},p}(h_{\mathbf{q},p}a_{\mathbf{q},p} + h^{*}_{\mathbf{q},p}a^{+}_{\mathbf{q},p}) \tag{3.15}$$

$$g_{\mathbf{q},p} = \left(\frac{\hbar}{2MN}\right)^{1/2}\frac{\boldsymbol{\kappa}\cdot\mathbf{e}_{\mathbf{q},p}}{\sqrt{\omega_{\mathbf{q},p}}} \tag{3.16}$$

$$h_{\mathbf{q},p} = \left(\frac{\hbar}{2MN}\right)^{1/2}\frac{\boldsymbol{\kappa}\cdot\mathbf{e}_{\mathbf{q},p}}{\sqrt{\omega_{\mathbf{q},p}}}\exp[i(\mathbf{q}\cdot\mathbf{l}_j - \omega_{\mathbf{q},p}t)] \tag{3.17}$$

Making use of a few operator identities, one can then write Equation 3.13 as:

$$\left(\frac{d^2\sigma}{d\Omega dE'}\right)_{coh} = \frac{\sigma_{coh}}{4\pi}\frac{k'}{k}\frac{N}{2\pi\hbar}\exp\langle U^2\rangle\sum_j \exp(i\boldsymbol{\kappa}\cdot\mathbf{l}_j)\int_{-\infty}^{\infty}\exp\langle UV\rangle \exp(-i\omega t)dt \tag{3.18}$$

The term $\exp\langle UV\rangle$ inside the integral can be expanded into a power series in the usual way:

$$\exp\langle UV\rangle = 1 + \langle UV\rangle + \frac{1}{2!}\langle UV\rangle^2 + ... \tag{3.19}$$

For a crystal of N atoms, there are $3N$ normal modes. The initial state of the material is given by the quantum numbers of these $3N$ modes $(n_1, n_2, ..., n_{3N})$. When a neutron scatters from these oscillators, the state of the system transitions to that of a system described by the quantum numbers: $n'_1, n'_2, ..., n'_{3N}$. For an elastic process (i.e. a process in which the state of the crystal remains unchanged), n_i=n'_i. The coherent cross-section for this process corresponds to the cross-section calculated using the first term in in Equation 3.19. This leads to a partial differential cross-section of the form:[6]

$$\left(\frac{d^2\sigma}{d\Omega dE'}\right)_{\text{coh el}} = \frac{\sigma_{coh}}{4\pi} N \exp\langle U^2\rangle \sum_j \exp(i\boldsymbol{\kappa}\cdot\mathbf{l}_j)\delta(\hbar\omega) \tag{3.20}$$

Taking the incident energy of the incoming neutrons to be fixed and integrating Equation 3.20 with respect to E':

$$\left(\frac{d\sigma}{d\Omega}\right)_{\text{coh el}} = \frac{\sigma_{coh}}{4\pi} N \exp(-2W)\frac{(2\pi)^3}{v_0}\sum_{\mathbf{G}}\delta(\boldsymbol{\kappa}-\mathbf{G}) \tag{3.21}$$

where $\mathbf{G}$ are reciprocal lattice vectors, $\frac{(2\pi)^3}{v_0}\sum_{\mathbf{G}}\delta(\boldsymbol{\kappa}-\mathbf{G}) = \sum_j \exp(i\boldsymbol{\kappa}\cdot\mathbf{l}_j)$, v_0 is the volume of the unit cell and W is the so-called Debye-Waller Factor:

$$2W = \langle U^2\rangle = \langle[\boldsymbol{\kappa}\cdot\mathbf{u}_0(0)]^2\rangle \tag{3.22}$$

The δ-function present in Equation 3.21 requires that, in order for scattering to take place $\mathbf{G}$ = $\mathbf{k}$' - $\mathbf{k}$. This is the same as Bragg's Law in X-Ray scattering. Should the above prescription be extended to a crystal structure that consists of not just a Bravais lattice but a Bravais lattice plus a basis (i.e. $\mathbf{R}_j = \mathbf{l}_j + \mathbf{d}_j + \mathbf{u}_j(t)$ where $\mathbf{d}_j$ is the j^{th} atom's position relative to the lattice point) then Equation 3.21 must be modified to include the nuclear structure factor $\mathrm{F}_N(\boldsymbol{\kappa})$:

$$\left(\frac{d\sigma}{d\Omega}\right)_{\text{coh el}} = N\frac{(2\pi)^3}{v_0}\sum_{\mathbf{G}}\delta(\boldsymbol{\kappa}-\mathbf{G})|\mathrm{F}_N(\boldsymbol{\kappa})|^2 \tag{3.23}$$

where:

$$\mathrm{F}_N(\boldsymbol{\kappa}) = \sum_{\mathbf{d}_j} \bar{b}_{\mathbf{d}_j} \exp(i\boldsymbol{\kappa} \cdot \mathbf{d}_j) \exp(-W_{\mathbf{d}_j}) \tag{3.24}$$

The incident neutrons may also scatter from structural excitations. If one assumes that the atoms are bonded together by springs, the lattice vibrations (phonons) have the ability to impart or take away energy from the incident neutron beam. The neutron will scatter when the energy it imparts (or takes away) creates (or annihilates) a phonon. To determine the scattering cross-section for the one-phonon process, on must repeat the above calculation, this time using the second term appearing in Equation 3.19. This leads to the following scattering conditions for one phonon creation: $E - E' = \hbar\omega_{\mathbf{q},j}$ and $\mathbf{q} + \mathbf{G} = \mathbf{k} - \mathbf{k}'$, where $\mathbf{q}$ is the wavevector of the phonon. For one phonon annihilation, the conditions $E' - E = \hbar\omega_{\mathbf{q},j}$ and $\mathbf{q} - \mathbf{G} = \mathbf{k} - \mathbf{k}'$ must be satisfied. For multi-phonon processes, one must perform the calculations for higher order terms of Equation 3.19. These calculations can be found in ref. [6] and serve to increase the background measured in neutron scattering experiments.

3.5 Magnetic Neutron Scattering

Once again, the derivations for the partial differential scattering cross-sections for neutron scattering from magnetism are long and fairly involved, so I will limit this discussion to the important results outlined in ref. [6]. While the neutron does not carry charge, it does carry spin-1/2 and through that a dipole moment. The operator describing this moment is given by:

$$\boldsymbol{\mu}_n = -\gamma\mu_N\boldsymbol{\sigma} \tag{3.25}$$

where γ=1.913, μ_N=$\frac{e\hbar}{2m_n}$ and $\boldsymbol{\sigma}$ is the Pauli Spin operator. The unpaired electrons in the crystal also carry a magnetic dipole moment given by:

$$\boldsymbol{\mu}_e = -2\mu_B \mathbf{s} \tag{3.26}$$

where μ_B is the Bohr magneton and $\mathbf{s}$ is the spin angular momentum operator. This dipole moment produces a magnetic field with which the neutron interacts. If one considers an electron with momentum $\mathbf{p}$ at position $\mathbf{R}$, then one can define the the magnetic field produced by this electron at a position $\mathbf{R}$ as the sum of the magnetic field produced by the electrons spin, $\mathbf{B}_s$, and the magnetic field produced by the electrons angular momentum, $\mathbf{B}_L$. The total magnetic field produced by the electron is therefore given by:

$$\mathbf{B} = \mathbf{B}_s + \mathbf{B}_L = \frac{\mu_0}{4\pi}\left[\text{curl}\left(\frac{\boldsymbol{\mu}_e \times \hat{\mathbf{R}}}{R^2}\right) - \frac{2\mu_B}{\hbar}\frac{\mathbf{p}\times\hat{\mathbf{R}}}{R^2}\right] \tag{3.27}$$

where $\hat{\mathbf{R}}$ is a unit vector directed along $\mathbf{R}$. This magnetic field creates an interaction potential, V_m=$-\boldsymbol{\mu}_n \cdot \mathbf{B}$, in which the the initial state of the neutron, given by σ, k, transitions to a state given by σ', k' and the state of the crystal transitions from λ to λ'. Subbing this potential into Equation 3.6 results in:

$$\left(\frac{d^2\sigma}{d\Omega dE'}\right)_{\sigma\lambda\rightarrow\sigma'\lambda'} = \frac{k'}{k}\left(\frac{m}{2\pi\hbar}\right)^2 |\langle \mathbf{k}'\sigma'\lambda'|V_s + V_L|\mathbf{k}\sigma\lambda\rangle|^2 \delta(E_\lambda - E_{\lambda'} + \hbar\omega) \tag{3.28}$$

If one considers the potential as a sum of the potentials from each individual electron, then Equation 3.28 can be written in a convenient form:

$$\left(\frac{d^2\sigma}{d\Omega dE'}\right)_{\sigma\lambda\rightarrow\sigma'\lambda'} = (\gamma r_0)^2\frac{k'}{k}|\langle\sigma'\lambda'|\boldsymbol{\sigma}\cdot\mathbf{Q}_\perp|\sigma\lambda\rangle|^2\delta(E_\lambda - E_{\lambda'} + \hbar\omega) \tag{3.29}$$

where:

$$\mathbf{Q}_\perp = \sum_i \langle \mathbf{k}'_i | \mathbf{W}_{si} + \mathbf{W}_{Li} | \mathbf{k}_i \rangle \tag{3.30}$$

$$\mathbf{W}_s = \text{curl}\left(\frac{\mathbf{s} \times \hat{\mathbf{R}}}{R^2}\right) \tag{3.31}$$

$$\mathbf{W}_L = \frac{1}{\hbar}\frac{\mathbf{p} \times \hat{\mathbf{R}}}{R^2} \tag{3.32}$$

and:

$$r_0 = \frac{\mu_0}{4\pi}\frac{e^2}{m_e} \tag{3.33}$$

If one considers scattering from the electron spin degree of freedom only (the Heilter-London Formalism), then one arrives at the result for the partial differential scattering cross-section due to a magnetic structure with a basis is[6]:

$$\begin{aligned}\frac{d^2\sigma}{d\Omega dE'} = (\gamma r_0)^2 \frac{k'}{k} \sum_{\alpha\beta} (\delta_{\alpha\beta} - \hat{\kappa}_\alpha \hat{\kappa}_\beta) \sum_j{}' \sum_j F_d^*(\boldsymbol{\kappa}) F_d \boldsymbol{\kappa} \\ \times \sum_{\lambda\lambda'} p_\lambda \langle \lambda | \exp(-i\boldsymbol{\kappa} \cdot \mathbf{R}_{j'}) S_{j'}^\alpha | \lambda' \rangle \\ \times \langle \lambda' | \exp(i\boldsymbol{\kappa} \cdot \mathbf{R}_j) S_j^{\beta} | \lambda \rangle \, \delta(E_{\lambda - E_{\lambda'} + \hbar\omega})\end{aligned} \tag{3.34}$$

where α, β denote the x, y and z directions, $\delta_{\alpha\beta}$ is the Kronecker delta, the subscript j denotes an ion at position $\mathbf{l}+\mathbf{d}$, p_λ is the probability the crystal is in the initial state λ and $F_d(\boldsymbol{\kappa})$ is known as the magnetic form factor. In the spin only system, $F_d(\boldsymbol{\kappa})$ is given by the Fourier transform of the normalized density of the unpaired electrons. To generalize this result to a system in which scattering may also occur for the orbital angular momentum, one must make the following considerations:

$$F_d(\boldsymbol{\kappa}) = \frac{1}{2}gF(\boldsymbol{\kappa}) \tag{3.35}$$

$$\frac{1}{2}gF(\boldsymbol{\kappa}) = \frac{1}{2}g_s\mathcal{J}_0 + \frac{1}{2}g_L(\mathcal{J}_0 + \mathcal{J}_2) \tag{3.36}$$

$$g_s = 1 + \frac{S(S+1) - L(L+1)}{J(J+1)} \tag{3.37}$$

$$g_L = \frac{1}{2} + \frac{L(L+1) - S(S+1)}{2J(J+1)} \tag{3.38}$$

$$\mathcal{J}_n = 4\pi \int_0^\infty j_n(\kappa r)s(r)r^2dr \tag{3.39}$$

where $j_n(\kappa r)$ are the Bessel functions of order n and $s(r)$ is the normalized density of unpaired electrons.[6] One must also replace S with J.

The above prescription has several consequences to the elastic scattering signatures from magnetic materials. If one considers a paramagnetic material in zero magnetic field, the scattering will be entirely diffusive (in the sense that there will be no resolution-limited Bragg peaks - note: completely diffusive scattering, with no structure in Q, only occurs in a complete paramagnet at T=infinity). When a magnetic field is applied, the Bragg peaks present will see an increase of intensity and the diffuse scattering will diminish to some extent.[6] When neutrons are incident on a magnetically ordered material (i.e. one in which the temperature is below the transition temperature), then the Bragg peak intensity would increase, provided the structural unit cell and the magnetic unit cell are commensurate (this is the case in all ferromagnetic materials). In antiferromagnets, however, it is possible for new magnetic Bragg peaks to manifest. This is due to the fact that in some antiferromagnetic materials, the magnetic structure is incommensurate with the nuclear structure. In both cases, one may look at a particular magnetic Bragg peak and measure the scattered intensity as a function of temperature. As the temperature is lowered from the transition temperature toward 0K, the intensity of the peak will increase until it reaches a saturated value. This intensity is related to the sub-lattice magnetization of the material and can therefore be used as the magnetic order parameter.

The effects of magnetism are not limited to elastic neutron scattering. The magnetic moments present in the the material of interest may also scatter inelastically. In simple ferromagnets or antiferromagnets, this is done by either the creation or destruction of spin excitations such as spin waves, which are the normal modes of a magnetically ordered state. As phonons are the particle associated with structural excitations in a crystal, so too are magnons or spin waves (these are the same thing) the excitations of a magnetically-ordered material. Spin waves have been shown to display dispersion relations.[7] When a neutron is incident on a material in an ordered state, the material may take away or add energy to the neutron to create a magnon in a very similar way to that of a phonon. The conditions for scattering from a magnon are as follows[6]:

$$\frac{\hbar^2}{2m}(k^2 - k'^2) = \hbar\omega_{\mathbf{q}} \tag{3.40}$$

$$\mathbf{k} - \mathbf{k}' = \mathbf{G} + \mathbf{q} \tag{3.41}$$

where $\mathbf{q}$ is the wavevector of the magnon. The dispersion measured via neutron scattering can then be fit using linear spin wave theory to determine the exchange coupling constants present in the material. Inelastic neutron scattering from magnetism is not limited to well defined spin wave or magnon detection however. Because spinons are created in pairs (when the probe provides the required energy to flip a spin in a 1D spin chain or break a dimer) the magnetic excitation spectrum will be continuous. This is in contrast to the creation of a magnon as only one magnon is created, thus resulting in a sharp excitation. This is because a magnon is a spin-1 excitation whereas a spinon is a spin-1/2 excitation. The neutron can flip its spin to create a spin-1 spin wave, but must create or destroy spinons in pairs to make either total spin-1 or total spin-0 excitations. Because the neutron interacts with the magnetic moments within the scattering system well, it is capable of creating the spinon pair. Thus, the neutron is a uniquely capable tool for examining spin wave and spinon dispersions in exotic and conventional materials.

3.6 The IN6-SHARP and Disk Chopper Spectrometers

I will now introduce the neutron scattering instruments used in this work, the first being the Disk Chopper Spectrometer (DCS) at the National Institute for Standards and Technology (NIST) in Gaithersburg, Maryland, USA. This instrument is a cold neutron scattering spectrometer that draws incident neutrons from the liquid hydrogen used moderate the neutrons produced in the nuclear reactor. These neutrons are then guided toward a a beryllium crystal to filter higher order reflections from contaminating the neutron beam. The neutrons passing through the crystal filter are then incident on seven disks with slits cut radially called choppers. The disks rotate with a rotation speed determined by the user. This allows the user to create monochromatic pulses of neutrons that are then incident on the sample. The neutrons scattered by the sample are then incident on a bank of ^{3}He detectors. The ^{3}He gas captures the neutron and the energy generated by the capture is converted to a voltage and registered by the hardware. The distance from sample to detector is known, measured to be 4m, so the outgoing energy of the scattered neutrons can be determined by the time at which the neutron capture happens relative to the beginning of the neutron pulse. See Figure 3.1 for a schematic diagram of the instrument.

Through NIST's instrument control software, the user has control of the incident wavelength (and thus the incident energy) through a range of 2.5Å-10Å, allowing the user to probe excitations on the order of 5meV and below. Each wavelength setting has an associated energy resolution as well as an incident neutron

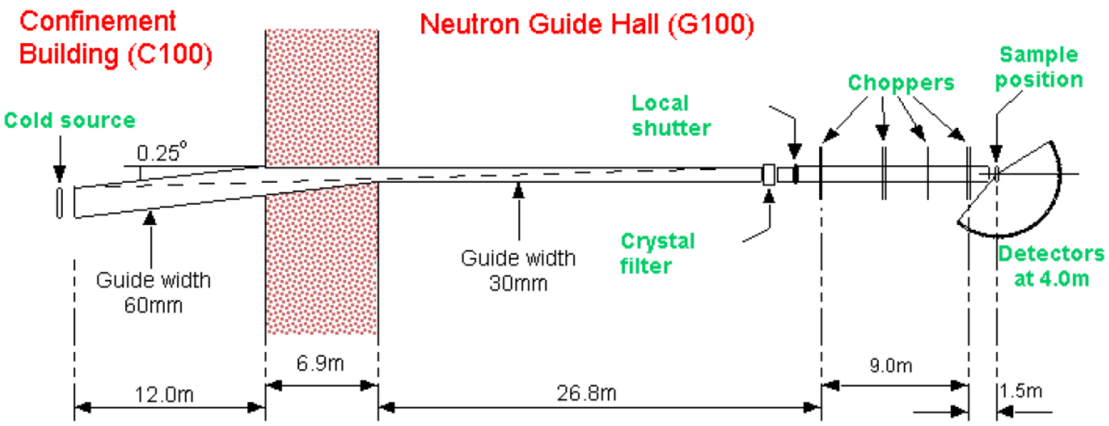

FIGURE 3.1: Schematic representation of DCS, adapted from the NIST DCS webpage

flux. In general, the longer the incident wavelength, the better the energy resolution with the consequence of lower incident neutron flux. Thus the user must make a choice to balance the neutron flux incident on the sample and the resolution of the instrument. The user also has control of the sample environment. DCS is compatible with a dilution refrigerator sample environment allowing for the study of neutron scattering at temperatures as low as 50mK. It can also accommodate a 10T vertical field magnet. It is for these reasons that DCS was chosen to perform cold neutron scattering experiments on $Ba_6Yb_2Ti_4O_{17}$. Data reduction and analysis was performed using a NIST developed software called DAVE.[34]

$ErMgGaO_4$ was studied using the IN6-SHARP instrument at the Institut Laue-Langevin in Grenoble, France. IN6-SHARP is similar to DCS in that they are both cold neutron time-of-flight spectrometers (they rely on the timing the neutron pulses to determine energy transfer between the neutron beam and the sample). IN6-SHARP uses three pyrolytic graphite crystals to create monochromatic beams of neutrons from those produced by the the reactor source. Higher order reflections are removed from the beams through a liquid nitrogen cooled beryllium filter. The neutron beams are then pulsed by a Fermi chopper. The neutrons are then incident on the sample and any scattered neutrons are collected by ^{3}He gas detectors (see Figure 3.2). This instrument is capable of producing incident neutrons of wavelength of 4.14Å, 4.62Å, 5.12Åand 5.92Å. The spectrometer gets is name by using time-focusing to produced a threefold increase in intensity incident on the sample. The three pyrolytic graphite crystals are slightly different. Thus, each crystal scatters a beam of neutrons that has a wavelength that is slightly different than the other two. The Fermi chopper pulses the three beams such that the portion of each beam it allows to pass will reach the sample at exactly the same time. This then provides a sharp threefold increase in neutron flux incident on the sample without a decrease in resolution. The instrument is compatible with a dilution refrigerator sample environment for probing low temperature magnetic states. Again, using ILL instrument control software, the user can control the sample environment temperature. Data reduction is performed using Mantid Workbench software.[35]

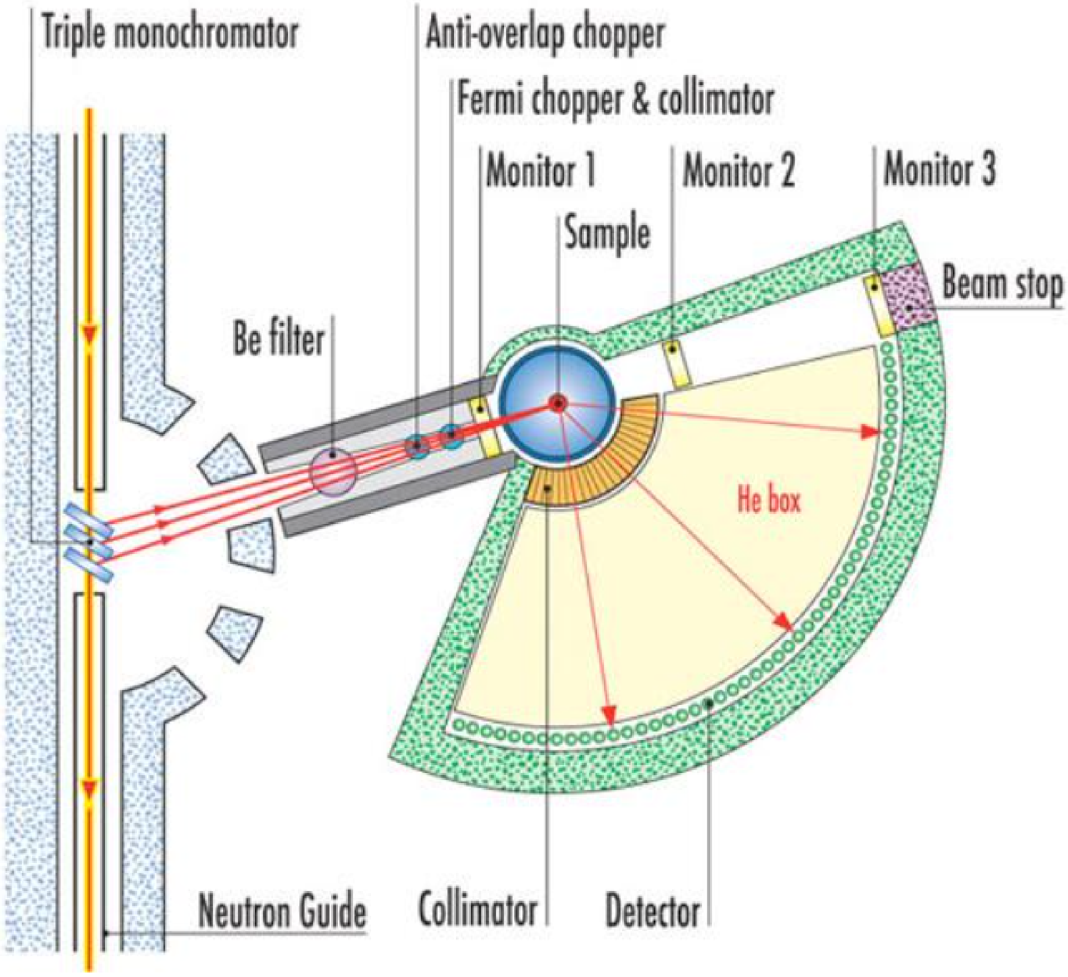

Figure 3.2: Schematic representation of IN6-SHARP, adapted from the ILL IN6-SHARP webpage

Chapter 4

Synthesis and Characterization of $Ba_6Yb_2Ti_4O_{17}$

4.1 Material Synthesis

Initial powder synthesis experiments made use of a 1400° C air reaction environment. Because the synthesis method for $Ba_6Yb_2Ti_4O_{17}$ was unknown and due to the complexity of its chemical formula, it was assumed that high temperatures and long annealing times would be required to produce a phase pure material. As such, the stoichiometric mixture of starting materials $BaCO_3$, Yb_2O_3 and TiO_2 we reacted for 6 days to produce a 30g proof of concept sample. The sample was removed every 48h to re-grind by hand. Once this 48h cycle was completed three times the resultant powder specimen was subjected to a powder X-ray diffraction (XRD) experiment. Rietveld refinement performed on the ensuing XRD pattern revealed a sample whose composition contained 3.53% $BaTiO_3$, 1.51% Yb_2O_3 impurities as well as a significant amount of unknown impurities (see Figure 4.1). This level of unknown impurity is not ideal, but, a single crystal growth growth was attempted using FZS technique in an air environment. The molten zone appeared to have a low viscosity and there appeared to be two phases within the melt, each with a slightly different melting temperature. As such, the zone was prone to both spill over and grinding. When all was said and done, no single crystal was produced. The resultant material consisted of gray-brown shell material

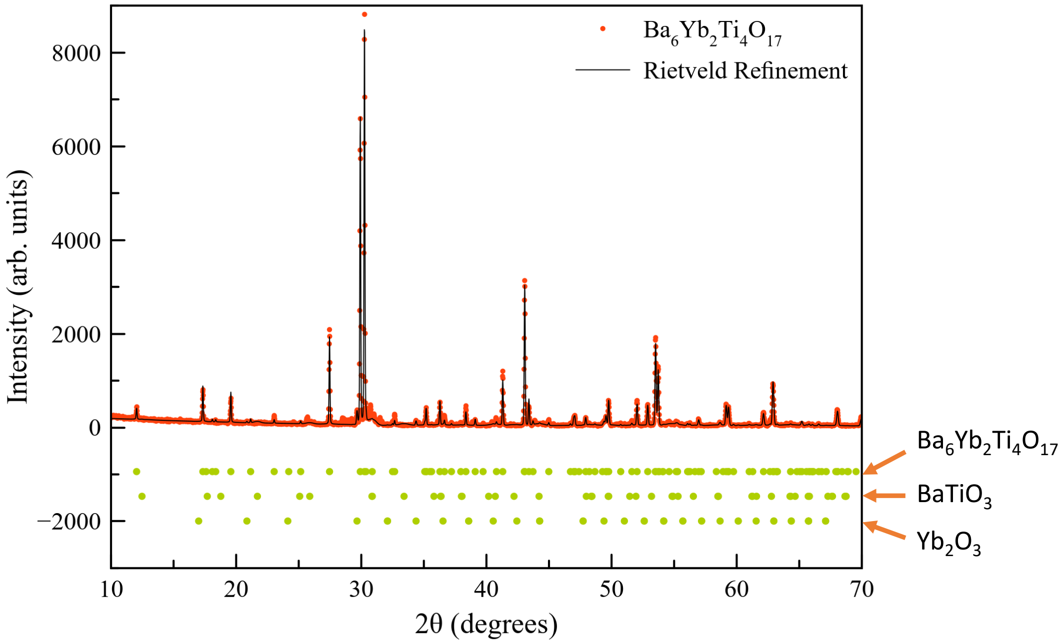

FIGURE 4.1: XRD powder diffraction of first $Ba_6Yb_2Ti_4O_{17}$ powder synthesis trial performed in a 1400° C air sample environment.

and a very small (on the order of millimeters in size) white core. Both were analyzed using powder XRD. The shell was revealed to contain 8.41% $BaTiO_3$ and 1.38% Yb_2O_3 impurities with no visible unknown impurities (see Figure 4.2a). The white core on the other hand, was much more difficult to analyze. While many of the peaks in the XRD pattern can be fit to the $Ba_6Yb_2Ti_4O_{17}$ structure, there are many peaks that do not seem to be present. This, combined with the fact that the refinement is quite poor, would suggest that this portion of the sample is not $Ba_6Yb_2Ti_4O_{17}$. Attempts to accurately identify the material producing these peaks ended in failure, largely due to peak asymmetry. The XRD pattern for the white core with the refinement for $Ba_6Yb_2Ti_4O_{17}$ can be found in Figure 4.2b.

It was presumed that the incongurency of the melt was due to the large amount of various impurities present in the rods used for FZS. With that in mind, the

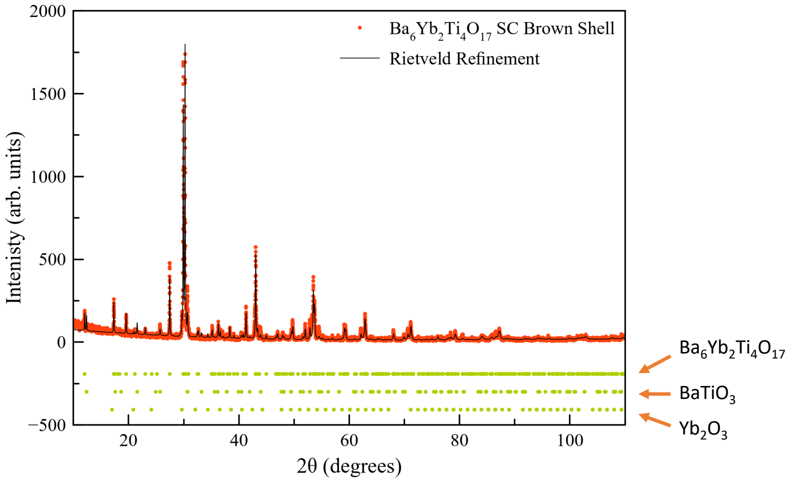

(A) Powder XRD pattern for the gray-brown material present in first FZS attempt.

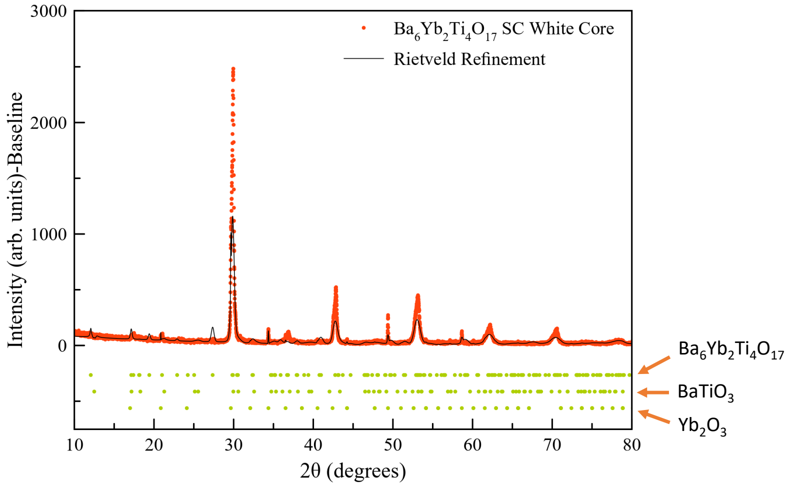

(B) Powder XRD pattern for the white material present in first FZS attempt.

FIGURE 4.2: Powder XRD patterns for the gray-brown shell and white core resultant from the first single crystal FZS attempt performed using an air environment. Synthesis trial resulted in no single crystals being produced.

next 30g powder synthesis experiment consisted of a stoichiometric mixture of the same starting materials in a 1350° C air environment. As in the previous trial, the specimen was removed several times during the experiment to re-grind by hand. This trial differed from the previous in that when the sample was removed, a small portion of the powder (on the order of 10's of mg) was used to generate a powder XRD pattern. The intent was to examine how the impurity evolves as a function of increasing reaction time. The XRD experiments were performed after a period of 72h, 5 days and 7 days. The resultant patterns can be seen in Figure 4.3. This resulted in a powder containing 7.39% $BaTiO_3$ and 16.82% Yb_2O_3 impurities as well as an unknown impurity phase after 72h and 4.43% $BaTiO_3$ and 9.69% Yb_2O_3 impurities as well as an unknown impurity phase after 5 days. After 7 days of annealing, the resultant specimen contained 9.27% $BaTiO_3$ and 8.05% Yb_2O_3 as well as unknown impurity phases. This shows that the amount of $BaTiO_3$ appears to fluctuate with each anneal, while the Yb_2O_3 appears to diminish with increasing annealing time. As the unknown impurities phases remained present throughout the entire experiment, but were not present in the gray-brown shell after the FZS single crystal synthesis experiment, it was determined that higher temperatures were required to eliminate those phases. Nevertheless, this powder was used to again perform a single crystal synthesis experiment using FZS technique, this time using an oxygen environment of 6 atmospheres. The higher pressure was applied to try to force the material to melt congruently. Once again, the molten zone exhibited low viscosity as well as the same incongruency as previously observed. The experiment resulted in no single crystals being formed. The experiment also resulted in the formation of only the gray-brown material (i.e. no white core was produced).

In an attempt to eliminate the unknown impurities in the resultant powder, a higher temperature of 1500° C was employed. The starting materials were initially annealed for 48 hours in an attempt to produce a 25g phase pure sample. The resultant powder was then analyzed by powder XRD refinement. The reaction resulted in a powder that contained 5.97% $BaTiO_3$ and 0.91% Yb_2O_3 impurities only (see Figure 4.4a). To try and eliminate the $BaTiO_3$ and Yb_2O_3 impurities further, the sample was placed in the furnace again in the same sample environment for an additional 24 hours. The additional annealing time increased the amount of

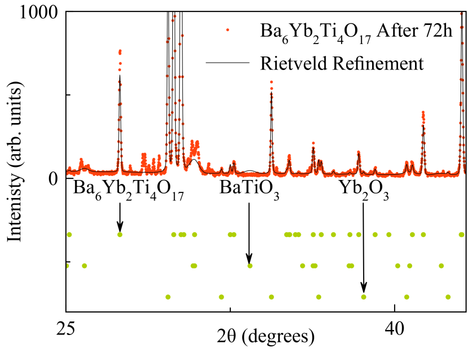

(A) XRD pattern of $Ba_6Yb_2Ti_4O_{17}$ after 3 days of annealing.

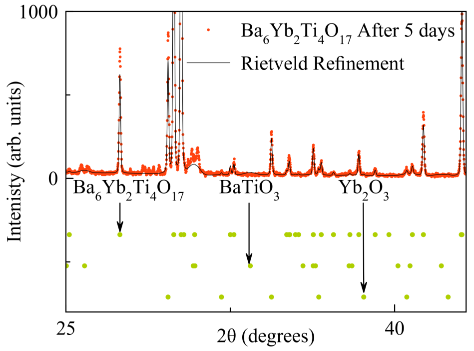

(B) XRD pattern of $Ba_6Yb_2Ti_4O_{17}$ after 5 days of annealing.

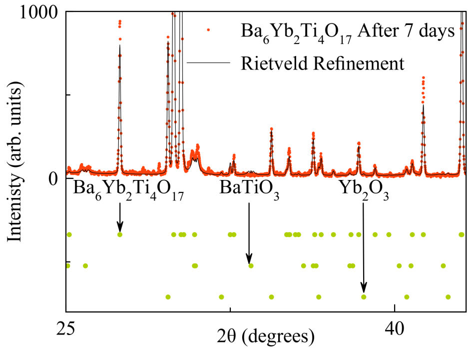

(C) XRD pattern of $Ba_6Yb_2Ti_4O_{17}$ after 7 days of annealing.

FIGURE 4.3: Powder XRD patterns a $Ba_6Yb_2Ti_4O_{17}$ powder synthesis experiment in a 1350° C air environment. XRD experiments conducted after 3, 5 and 7 days. The phase markers (green dots) follow the same pattern as in Figure 4.1

$BaTiO_3$ present in the sample to 7.24% without much change in the Yb_2O_3 present (0.93% present after the additional 24 hours). The powder diffraction pattern can be seen in Figure 4.4b. With no unknown impurity present, and the smallest amount of total known impurities, the optimal materials preparation technique appears to be an annealing in a 1500° air environment for a period of 48 hours. This sample was also subjected to a FZS experiment. This once again resulted in the formation of zero single crystals due to the molten zones tendency to spill and grind (i.e. portions of the material within the floating zone remained solid causing the molten zone to shake). Figure 4.5 shows the common outcome of one of these growth attempts. The optimal single crystal synthesis conditions have yet to be identified.

With all of the previous powders used for single crystal synthesis, another 10g batch was synthesized for the purposes of magnetic susceptibility measurements and thermal neutron scattering experiments. This powder was annealed following the previously disclosed optimal synthesis technique. The resultant powder was found to contain 6.5% $BaTiO_3$ and 1.18% Yb_2O_3 impurities by Rietveld refinement. While the amount of $BaTiO_3$ present in the material has increased somewhat, it is non-magnetic and thus should not affect the magnetic ground state.

4.2 Magnetic Characterization

To characterize the magnetic ground state of $Ba_6Yb_2Ti_4O_{17}$, the DCS instrument at NIST in Gaithersburg, Maryland, USA was used. The experiment was performed on a 5g sample, provided by Professor Edwin Kermarrec and Suvam Bhattacharya from the Université Paris-Saclay, which contained a nominal amount of non-magnetic impurity. The sample needed to be provided by Professor Kermarrec as all powders produced at McMaster at the time of the experiment were used in single crystal synthesis experiments. The sample was placed in an aluminum sample can under vacuum. The can was then placed in a dilution refrigerator sample environment with a 10T magnet attachment. The purpose the experiment was to observe and analyze the ground state spin correlations and their field dependence. These findings would then be compared to the neutron scattering experiments on

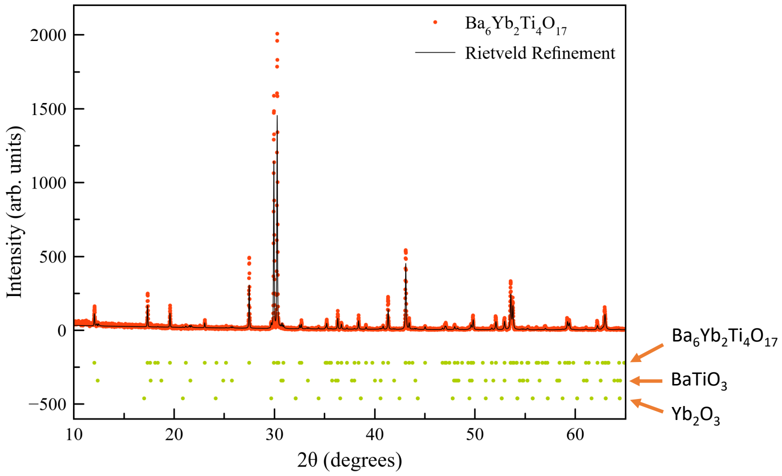

(A) Powder XRD pattern of $Ba_6Yb_2Ti_4O_{17}$ after a 48 hour anneal at 1500° C.

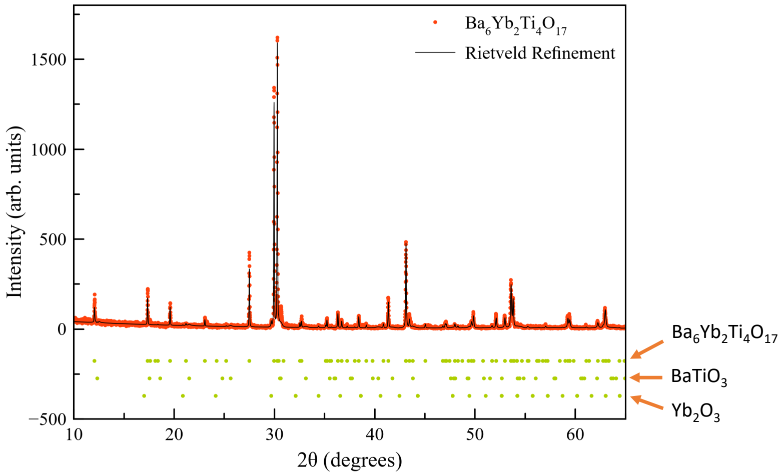

(B) Powder XRD pattern of $Ba_6Yb_2Ti_4O_{17}$ after an additional 24 hour anneal at 1500° C.

FIGURE 4.4: Powder XRD patterns for $Ba_6Yb_2Ti_4O_{17}$ prepared at 1500° C in air after 48 hours and 72 hours.

Figure 4.5: Resultant material from FZS experiment using rods comprised of $Ba_6Yb_2Ti_4O_{17}$ powder annealed at 1500° C.

a single crystal of $YbMgGaO_4$, found in ref. [1], in an attempt to elucidate the QSL nature of the material. The experiment was conducted at a base temperature of 60mK in applied magnetic fields of 0T, 2T, 3T, 4T, 5T and 8T using incident neutrons with wavelengths of 5Å. A 7Å wavelength incident neutron beam was also employed at applied magnetic fields of 0T and 8T. Both wavelengths were used to produce data sets at a temperature of 1K in a 0T field as well, to be used as background data. The data sets were then reduced using DAVE for further analysis. Colour contour plots of the raw energy transfer versus magnitude of the scattering wavevector are presented for select fields in Figure 4.6. The raw neutron scattering data sets reveal the splitting of the Kramer's doublet ground state of the Yb^{3+} ions in this system (as evidenced by the the flat excitation evolving upwards in energy transfer as a function of increasing field) but there is no obvious spinon continuum, at least by eye. To examine this further, cuts in energy over a range of $|Q|=[0.5, 1.2]Å^{-1}$ were analyzed (see Figure 4.7). The inelastic scattering peaks observed in these cuts are the integrated intensity of the split Kramer's doublet within that |Q| range. These peaks were fitted to Lorenzian functions to determine the energy splitting. That was then plotted versus the field applied. By recalling the second term appearing in the magnetic Hamiltonian present in Equation 1.21, one can fit the data to a linear function and determine the powder averaged g-tensor, g_{powder}. g_{powder} was found to be 2.36±0.04 from this analysis. The cuts along energy also reveal no obvious spinon-like excitations present in the raw data so further examination is required.

To provide a better look at the low energy spin correlations in the $Ba_6Yb_2Ti_4O_{17}$ system, several background subtractions were employed. The first was a subtraction using the 8T data set as the background set. By using the 8T data set as a background, one can examine the real background as well as lattice contributions to the neutron scattering. The colour contour plot for the 0T - 8T case is presented in Figure 4.8a. The same analysis technique used for the raw data was used for this subtraction (i.e. cuts through energy transfer with the same |Q| integration window were analyzed). The ensuing cuts along energy transfer reveal the possibility of a spinon continuum in the 0T field minus 8T field data with a bandwidth of approximately 0.3meV. However, the signal to noise ratio is poor for such weak scattering and is thus inconclusive (see Figure 4.8b and Figure 4.8c).

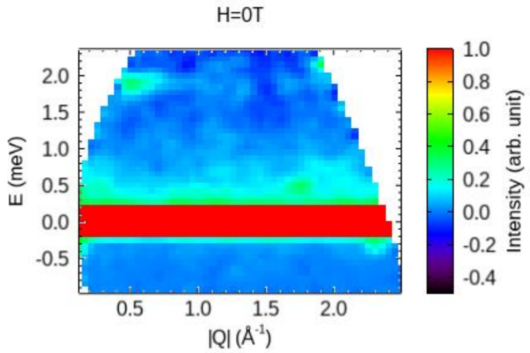

(A) Energy transfer vs. |Q| map of $Ba_6Yb_2Ti_4O_{17}$ using a 5Å incident neutron beam at 60mK in a 0T applied field

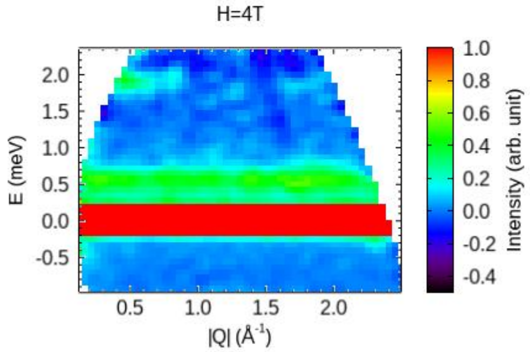

(B) Energy transfer vs. |Q| map of $Ba_6Yb_2Ti_4O_{17}$ using a 5Å incident neutron beam at 60mK in a 4T applied field

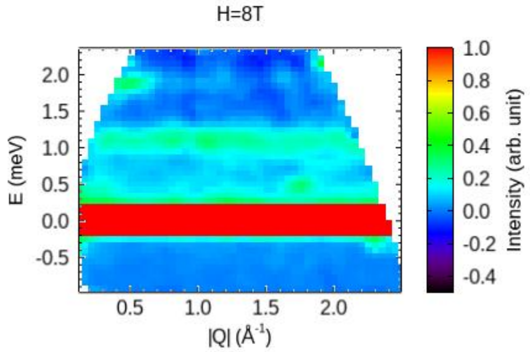

(C) Energy transfer vs. |Q| map of $Ba_6Yb_2Ti_4O_{17}$ using a 5Å incident neutron beam at 60mK in a 8T applied field

FIGURE 4.6: Energy transfer vs. |Q| colour contour maps for select applied fields as a result of cold neutron scattering from $Ba_6Yb_2Ti_4O_{17}$ using DCS with an incident neutron wavelength of 5Å at 60mK

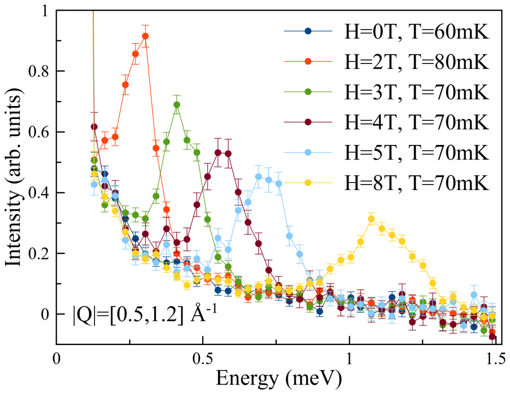

(A) Cuts in energy energy transfer with |Q|=[0.5, 1.2]$\mathrm{\AA}^{-1}$ for various applied fields.

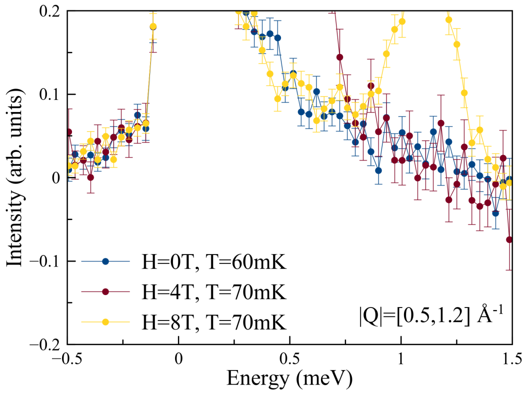

(B) Cuts in energy transfer with |Q|=[0.5, 1.2]$\mathrm{\AA}^{-1}$ for select applied fields. No obvious signatures of spinon continuum are present.

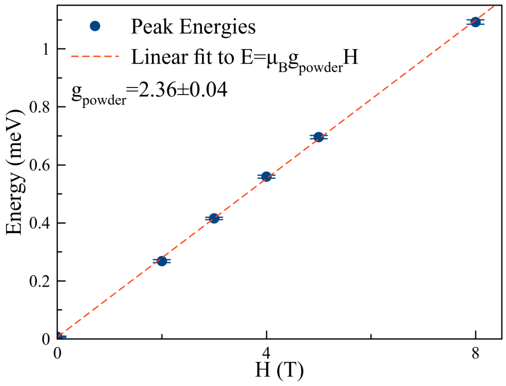

(C) Energy transfer vs. applied field, H.

FIGURE 4.7: Analysis of cuts along energy with a common |Q| integration range. The inelastic peaks present in the data represent the splitting of the Kramer's ground state double with increasing magnetic field. Peak positions were determined using a Lorenzian function.

Subtracted Data Set	g_{powder}
No Subtraction	2.36±0.04
8T field subtraction	2.393±0.004
0T field subtraction	2.43±0.02
1K temperature subtraction	2.41±0.02

TABLE 4.1: g_{powder} for various background subtractions in $Ba_6Yb_2Ti_4O_{17}$ as estimated by fitting the energy splitting of the Kramer's ground state doublet to $E=g_{powder}\mu_B H$

The 0T applied field data set and the 1K data set were also used as background data sets for the purpose of isolating the real magnetic scattering. The results of these subtractions are presented in Figure 4.9 and Figure 4.10. The corresponding values for g_{powder} can be found in Table 4.1. The values of g_{powder} resultant from each subtraction are quite consistent.

The neutron scattering data is supplemented by further magnetic characterization via a point charge calculation and a DC susceptibility measurement. The point charge calculation - performed using PyCrystalField.py[33] - estimates that the ground state and excited state structures are those presented in Table 4.2. This construction was then used to determine an anisotropic g-tensor in the form of Equation 2.17:

$$g = \begin{bmatrix} 2.431 & 0 & 0 \\ 0 & 2.431 & 0 \\ 0 & 0 & 2.084 \end{bmatrix}$$

This implies a theoretical powder averaged g-tensor to be 2.315 which is in good agreement with the observed powder averaged g-tensor in the DCS experiment. While this theoretical calculation agrees well with the experimentally observed values, one is still required to perform CEF analysis on thermal neutron scattering experiment data to verify this result. Because one assumes the ions within the local environment to be point charges, the effects of the spacial extent of the ions has been ignored. This can be significant when considering the construction of the ground state and excited state doublets as well as the spin anisotropy in the

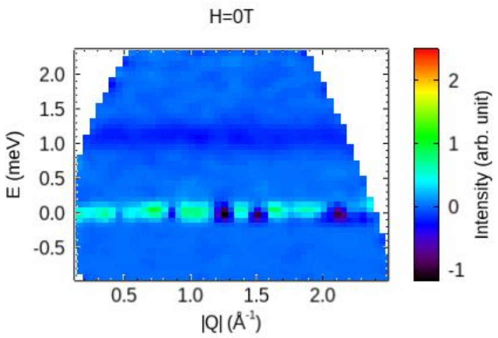

(A) Colour contour map presented in Figure 4.6a with an 8T subtraction

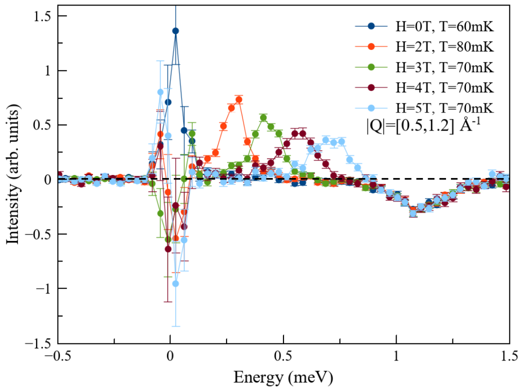

(B) Cuts in energy transfer with |Q|=[0.5, 1.2]Å^{-1} for all applied fields with an 8T applied field subtraction.

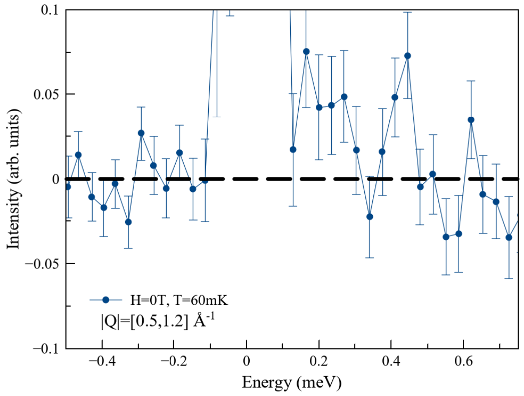

(C) The same 0T - 8T cut presented above with a smaller energy window.

FIGURE 4.8: Data analysis using the 8T neutron scattering data set as a background data set. The 0T-8T colour contour plot is shown in (A). Cuts in energy with each applied field are also shown showing the splitting of the Kramers' ground state doublet.

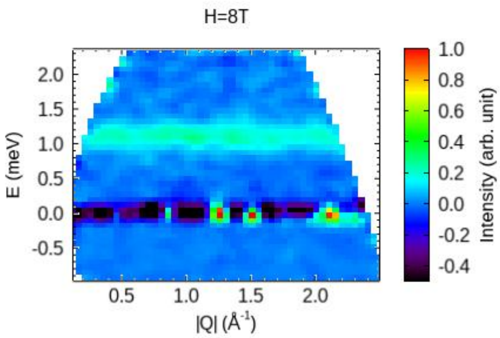

(A) Colour contour map presented in Figure 4.6c with a 0T subtraction

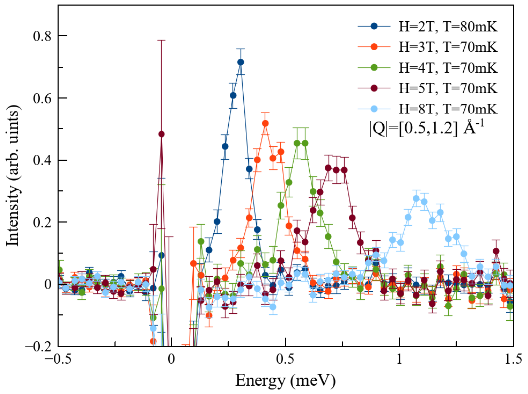

(B) Cuts in energy transfer with |Q|=[0.5, 1.2]Å^{-1} for all applied fields with a 0T applied field subtraction.

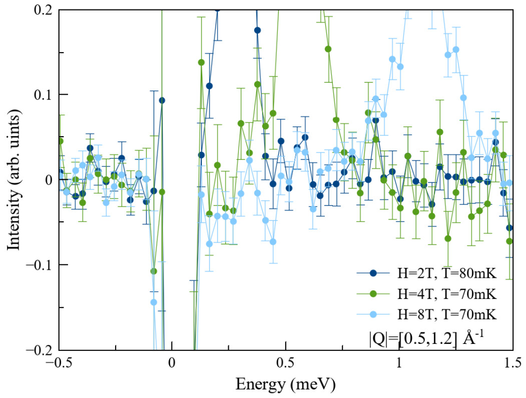

(C) The same 0T subtraction cuts presented above with a smaller energy window.

FIGURE 4.9: Similar data analysis found in Figure 4.8 this time using the 0T neutron scattering data set as a background data set. Here the colour contour plot of 8T-0T is shown as well as cuts in energy for each applied field with a 0T background subtraction to show the ground state doublet splitting.

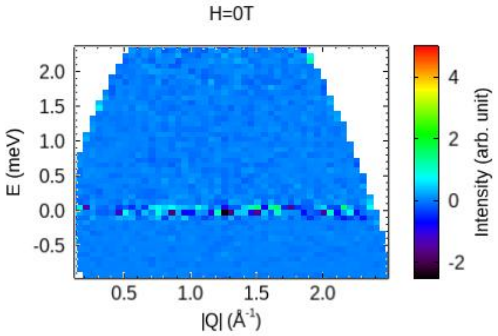

(A) Colour contour map presented in Figure 4.6a with a 1K data set subtraction

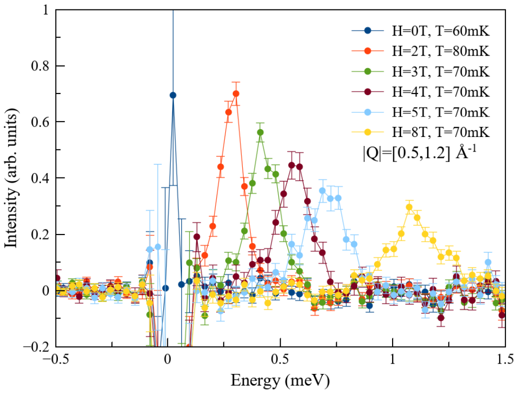

(B) Cuts taken along energy transfer with |Q|=[0.5, 1.2]Å^{-1} for all applied fields with a 1K data set subtraction.

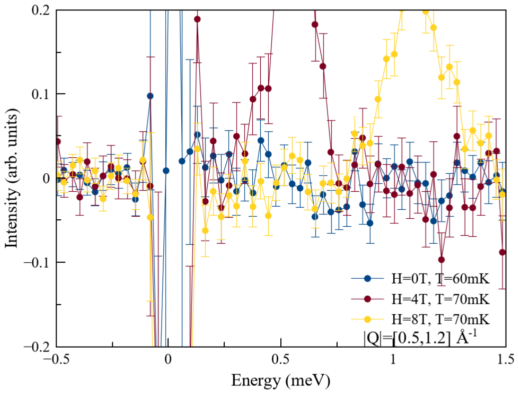

(C) A selection of cuts presented in Figure 4.10b to show weak scattering signatures.

Figure 4.10: Similar data analysis found in Figure 4.8 this time using the 1K neutron scattering data set as a background data set. Here the colour contour plot of 0T-1K is shown as well as cuts in energy for each applied field with a 1K background subtraction to show the ground state doublet splitting.

E (meV)	$\|7/2\rangle$	$\|5/2\rangle$	$\|3/2\rangle$	$\|1/2\rangle$	$\|-1/2\rangle$	$\|-3/2\rangle$	$\|-5/2\rangle$	$\|-7/2\rangle$
0.00	0.221	0	0	-0.623	0	0	-0.75	0
0.00	0	0.75	0	0	-0.623	0	0	-0.221
25.56	0	0	0.246	0	0	-0.969	0	0
25.56	0	0	-0.969	0	0	-0.246	0	0
44.17	-0.431	0	0	0.628	0	0	-0.648	0
44.17	0	-0.648	0	0	-0.628	0	0	-0.431
96.09	-0.875	0	0	-0.467	0	0	0.129	0
96.09	0	-0.129	0	0	-0.467	0	0	0.875

Table 4.2: Eigenvalues and eigenvectors of the ground state and excited CEF doublets estimated by point charge calculations using PyCrystalField.py. [33]

material. DC susceptibility measurements were performed on the 48 hour 1500° C sample in a constant 100Oe field for temperatures ranging from 0.5K to 100K. χ_{mass} was plotted in units of e.m.u $g^{-1}G^{-1}$. The susceptibility data, plotted on a log(T) scale in Figure 4.11a, revealed no spin freezing or magnetic ordering down to 0.5K. The inverse susceptibility data was fit to a Curie-Weiss law for both the low temperature regime (2K to 5K) and a moderate temperature regime (25K to 50K). These fits give estimates of the Weiss temperature of -0.37K and -11.3K respectively, thus implying antiferromagnetic interactions within the spin system. The fact that the Curie-Weiss temperature changes and seems headed to zero is indicative of a susceptibility whose shape is likely influenced by crystal field effects. Hence its full temperature dependence would be described by a Van Vleck susceptibility. The low Curie-Weiss temperature is consistent with the lack of spinon continuum observed in the neutron scattering data. The strong decrease in the Weiss temperature when the fitting is performed at higher temperatures suggests that the CEF levels are influencing the Van Vleck contribution to the susceptibility. The susceptibility data and the Curie-Weiss analysis are presented in Figure 4.11. It is important to note that these data represent the raw magnetic susceptibility. No temperature independent contributions have been removed.

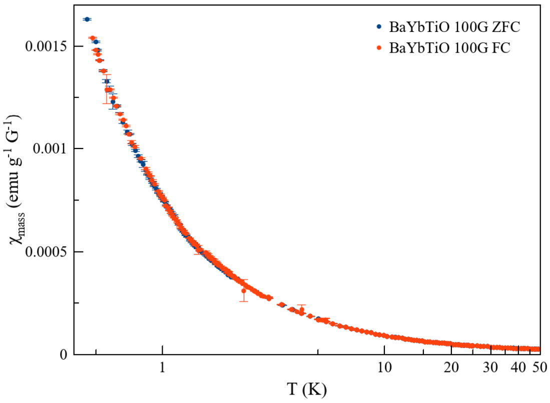

(A) ZFC and FC DC susceptibility of $Ba_6Yb_2Ti_4O_{17}$ in a constant 100Oe applied field.

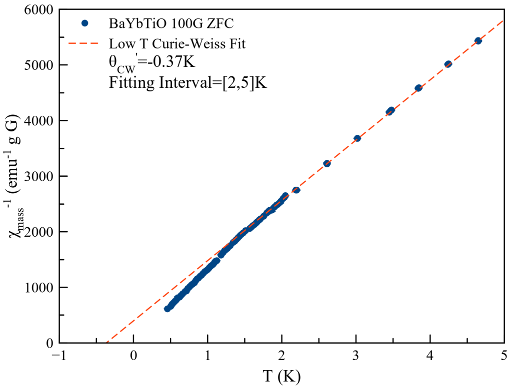

(B) Curie-Weiss fitting of the inverse susceptibility at low temperatures.

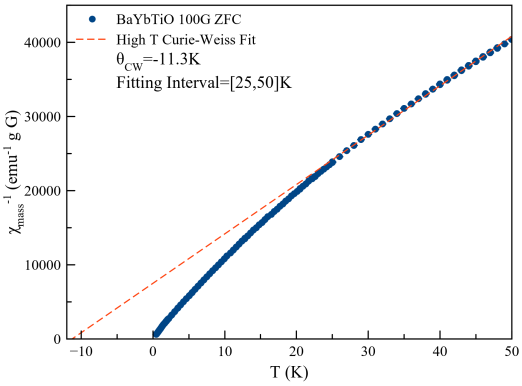

(C) Curie-Weiss fitting of the inverse susceptibility at moderate temperatures.

Figure 4.11: DC Susceptibility analysis for $Ba_6Yb_2Ti_4O_{17}$ in a constant 100Oe applied field.

4.3 Discussion and Future Work

Synthesis experiments performed to date suggest the optimal synthesis procedure for $Ba_6Yb_2Ti_4O_{17}$ powder is an annealing of a stoiciometric mixture of $BaCO_3$, Yb_2O_3 and TiO_2 for 48 hours at 1500° C in air. This produces a $Ba_6Yb_2Ti_4O_{17}$ powder with nominal amounts of $BaTiO_3$ and Yb_2O_3. Synthesis attempts at lower temperatures give rise to unknown impurity phases while longer anneals increase the amount of $BaTiO_3$ impurity. This suggests that $Ba_6Yb_2Ti_4O_{17}$ is itself an unstable phase. FZS experiments using the resultant powders from such powder synthesis trials reveal a molten zone that is impossible to control using the optical image furnaces available at McMaster University. Due to the low viscosity and the incongruency of the melt, all attempts at producing single crystals via FZS technique have ended in failure. Due to the complexity of the chemical formula, it may be impossible to produce single crystals using the equipment available in the BIMR laboratories. Collaboration with the Stewart Blusson Quantum Materials Institute at the University of British Columbia or Paradigm at Johns Hopkins University in Baltimore, Maryland where FZS furnaces with higher pressures are available, might be fruitful.

Magnetic characterization was performed using low temperature DC susceptibility analysis and cold neutron inelastic neutron scattering in a magnetic field at low temperatures. In addition, point charge calculations of the CEF levels for Yb^{3+} in Ba6Yb2Ti4O17 were carried out. The susceptibility revealed no spin freezing and no magnetic ordering down to 0.5K, which is a typical signature of QSL materials.[11] Inverse susceptibility revealed a -0.37K and a -11.3K Weiss temperature when fitting the data to a Curie-Weiss law between temperatures of 2K to 5K and 25K to 50K respectively. The negative Weiss temperatures confirm the presence of antiferromagnetic couplings between local magnetic moments in $Ba_6Yb_2Ti_4O_{17}$.[2] While the Weiss temperature appears to be temperature dependent, the change is likely due to CEF effects that cannot be accounted for without CEF analysis.

A powder neutron scattering experiment was performed using cold neutrons and a magnetic field to compare with the neutron scattering measurements on

$YbMgGaO_4$ found in ref. [1]. Our neutron scattering data, reduced and analyzed using DAVE [34], revealed the Zeeman splitting as a function of increasing magnetic field of the Kramer's ground state doublet for the Yb^{3+} ions in the $Ba_6Yb_2Ti_4O_{17}$ structure. Fitting the energy splitting as a function of increasing magnetic field provided estimates for the powder averaged g-tensor for each of the background subtractions performed (see Table 4.1). Different subtractions of data sets as a function of temperature and magnetic field paint a consistent picture, within error. Cuts along energy transfer of the raw data sets (i.e. no background data set subtraction) did not indicate a spinon continuum as one would expect for a triangular antiferromagnet QSL. When the 8T data set is used as a high field background, there appears to be come quasi-elastic magnetic scattering present in the energy cuts. The bandwidth of this feature is 0.3meV and is significantly smaller than the bandwidth of the spinon continuum observed in [1]. This would suggest that $Ba_6Yb_2Ti_4O_{17}$ could be a weakly interacting QSL candidate but the signal to noise ratio makes it difficult to draw conclusions. The weak interactions inferred from the neutron scattering data are consistent with susceptibility data. This study was supplemented by a theoretical point charge calculation to estimate the ground state and excited state wavefunctions and eigenenergies. The point charge calculation also estimated a relatively isotropic g-tensor that is consistent with the powder averaged g-tensors observed in the neutron scattering experiment. The isotropic nature of the spin system in $Ba_6Yb_2Ti_4O_{17}$ is consistent with the isotropic nature observed in $YbMgGaO_4$, although in $YbMgGaO_4$ a larger g value was observed.[19] To complete this study, magnetization versus applied field should be performed using a constant temperature of 5K. By fitting this data to Equation 1.17, the antiferromagnetic coupling constant J can be estimated. CEF transition analysis must also be performed using thermal neutron scattering in order to measure all of the transitions out of the CEF ground state doublet. Fitting the CEF transitions will provide an experimentally accurate g-tensor as well as the full eigenvectors and eigenvalues of the ground state and excited state doublets. This can then be used to validate the g-tensors observed by the point charge calculation and the cold neutron scattering experiments.

Chapter 5

Synthesis and Characterization of $ErMgGaO_4$

5.1 Sample Preparation

Preparation of phase pure $ErMgGaO_4$ has yet to be reported in the literature. Every reported instance of synthesized $ErMgGaO_4$ has a nominal amount of $Er_3Ga_5O_{12}$, a material with a garnet structure exhibiting a spin glass transition at 0.8K.[29] In order to accurately characterize the ground state of $ErMgGaO_4$ one must examine the magnetic features of a phase pure sample; magnetic impurities serve to muddy the waters of the magnetic ground state. To that end, I set out to produce a phase pure $ErMgGaO_4$ sample. To do this, the FZS technique was employed using rods of 10cm in length and 0.5cm in diameter comprising of a stoichiometric mixture of Er_2O_3, MgO and Ga_2O_3 sintered at 1200° C. Three synthesis experiments were performed, each using a 7 atm oxygen gas environment. The first growth (conducted by Casey Marjerrison and James Beare), using a feed rod speed of 0.25mm/h and a seed rod speed of 0.5mm/h, resulted in a rod 7cm in length that was 9.3g in mass. This rod was confirmed to be polycrystallline via Laue XRD. In cutting through different sections of the material, XRD experiments revealed portions of the rod containing no $Er_3Ga_5O_{12}$ impurity and other sections with varying amounts (ranging anywhere from a fraction of a percent to 35%). Thus, in order to provide an adequately sized polycrystalline sample for neutron scattering, a thorough survey of the impurities present in the resultant rod was required

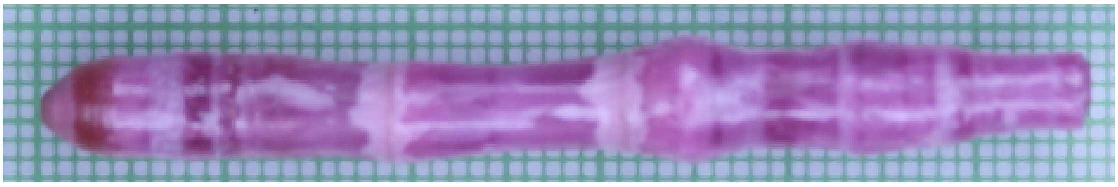

FIGURE 5.1: Resultant polycrystalline rod from a FZS $ErMgGaO_4$ growth using 7atm of O_2 gas and feed and seed rod speeds of 0.5mm/h.

millimeter by millimeter. It was immediately obvious that one FZS would not be enough to produce the necessary phase pure mass for neutron scattering. The next growth used feed and seed rod speeds of 2.5mm/h. This growth has yet to be characterized as time and effort was focused on the first and third growths, due to timing constraints. The third growth (pictured in Figure 5.1) was performed using 0.5mm/h feed and seed rod speeds. Five pieces of this rod were isolated for further investigation via Laue XRD to determine if they are single crystal. The first and third growths provided 0.85g of $ErMgGaO_4$ powder containing no detectable $Er_3Ga_5O_{12}$ impurities, combined. For the purposes of a neutron scattering study, this 0.85g sample (henceforth referred to as Sample 1) was supplemented with a 1.26g sample containing 1.14% $Er_2Ga_5O_{12}$ (Sample 2). This resulted in a 2.11g sample with a 0.68% $Er_3Ga_5O_{12}$ impurity, which is less than what has been reported in [28] and [29]. The XRD patterns for both the phase pure and the sample containing 1.14% $Er_3Ga_5O_{12}$ are shown in Figure 5.2.

5.2 Magnetic Characterization

Prior to performing a neutron scattering experiment on the two samples, the influence of the impurity on the magnetic signatures was determined. This was done using a DC susceptibility measurement as a function of temperature from 0.5K to 50K (Figure 5.3). Susceptibility data for both samples 1 and 2 exhibit the same spin-glass like transition at 0.75K (evidenced by the hysteresis of the ZFC and FC data below that temperature) and a broad magnetic feature at 3-4K. This contrasts with the susceptibility measurements performed in [29] on a single crystal with 5% $Er_3Ga_5O_{12}$ along two different crystallographic directions. The

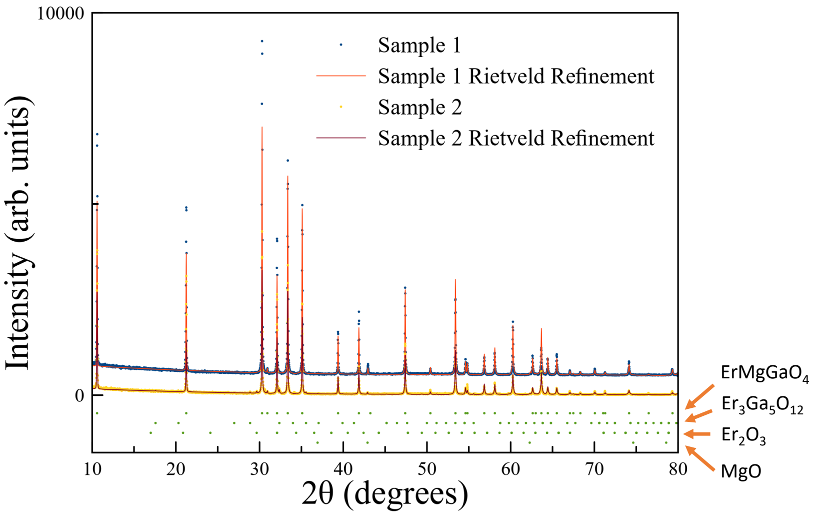

(A) Powder XRD pattern of both the pure $ErMgGaO_4$ sample and the sample containing 1.14% $Er_3Ga_5O_{12}$ impurity.

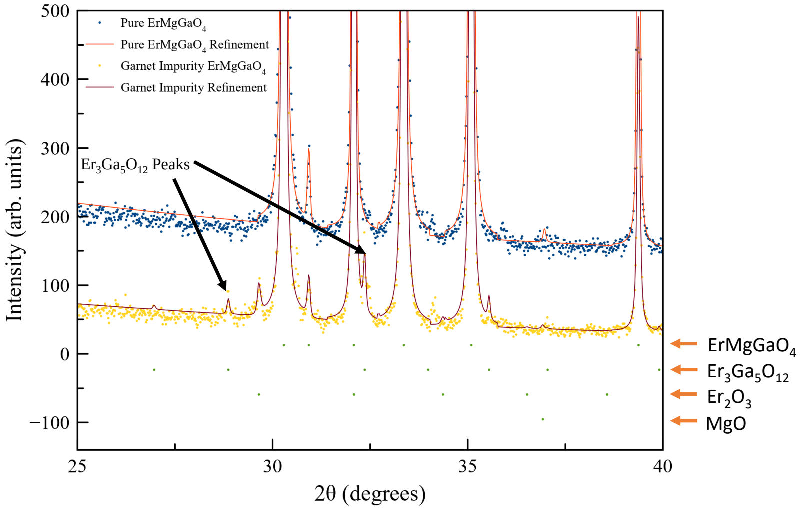

(B) The same XRD patterns presented above on a smaller scale showing the change in $Er_3Ga_5O_{12}$ impurity.

FIGURE 5.2: Powder XRD patterns for both $ErMgGaO_4$ samples. Here, Sample 1 denotes the phase pure $ErMgGaO_4$ sample while Sample 2 denotes the sample containing 1.14% $Er_3Ga_5O_{12}$. Sample 1 has been shifted vertically upward.

inverse susceptibility was analyzed using a Curie-Weiss fitting over temperature ranges of 2K to 5K and 25K to 50K. Sample 1 exhibited Weiss temperatures of -7.38K and -14.7K while Sample 2 exhibited Weiss temperatures of -6.97K and -14.5K for the aforementioned fitting regions respectively (see Figure 5.4 and Figure 5.5), providing good agreement between the two magnetic responses. As was the case in $Ba_6Yb_2Ti_4O_{17}$, this shows that that the local magnetic moments in the material are antiferromagnetically coupled at low temperatures. This would also suggest that these features are intrinsic to $ErMgGaO_4$ and any magnetic features one might observe in neutron scattering data would be from $ErMgGaO_4$ as well.

A cold neutron scattering study was performed on Samples 1 and 2 using the IN6-SHARP instrument at ILL in Grenoble, France. To prevent contaminating the samples, they were enveloped in aluminum foil individually prior to being placed inside the aluminum sample can. The can was then filled with a helium exchange gas to ensure that the sample would appropriately thermalize and cooled using a dilution refrigerator sample environment. This study was an exploratory study to examine the low energy magnetic excitations in the system in the absence of an applied magnetic field. Using a 5.12Å incident neutron wavelength, data sets for a number of temperatures ranging from 125mK to 100K were collected. An energy transfer versus magnitude of scattering vector colour contour plot at 125mK is presented in Figure 5.6 and colour contour plots for other select temperatures can be found in Figure 5.7. At the lowest temperatures, a spinon-like continuum of excitations is observed and persists to 4K. This continuum has a bandwidth of approximately 0.8meV and is remarkably similar to the continuum exhibited by $YbMgGaO_4$.[1] Figure 5.6b shows two elastic features, one centred on q=1.5Å^{-1} and one centred on q=1.1Å^{-1}. The peak at q=1.5Å^{-1} is a nuclear Bragg peak while the q=1.1Å^{-1} is incommensurate with the allowed nuclear Bragg peaks. It is also quite diffuse (i.e. it is not resolution limited in q as one would expect for a Bragg peak). It is therefore a diffuse magnetic peak. To examine this feature further, cuts along q integrating over an energy range of E=[-0.08, 0.08]meV were plotted (see Figure 5.8). The diffuse magnetic feature has a pronounced temperature dependence. Integrating the intensity over q=[0.8, 1.25]Å^{-1} and plotting as a function of temperature is presented in Figure 5.9. This can be used as an order

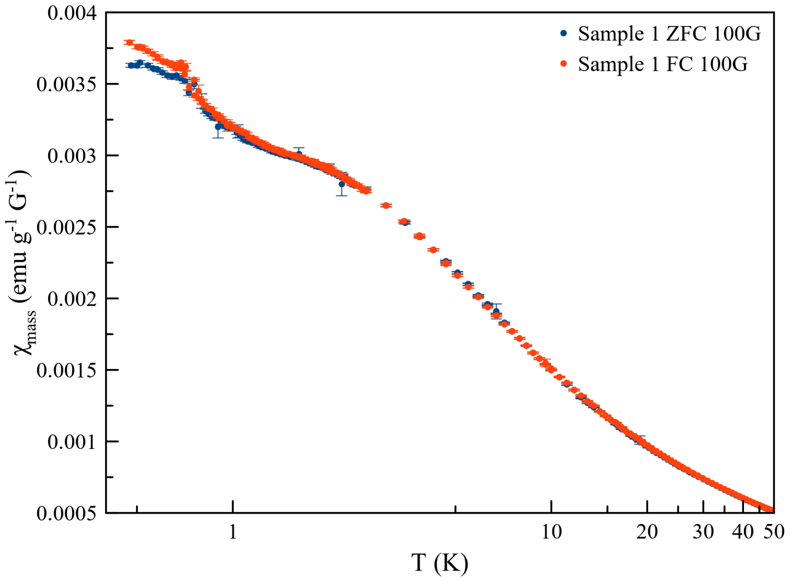

(A) DC susceptibility of Sample 1 in a 100Oe applied magnetic field.

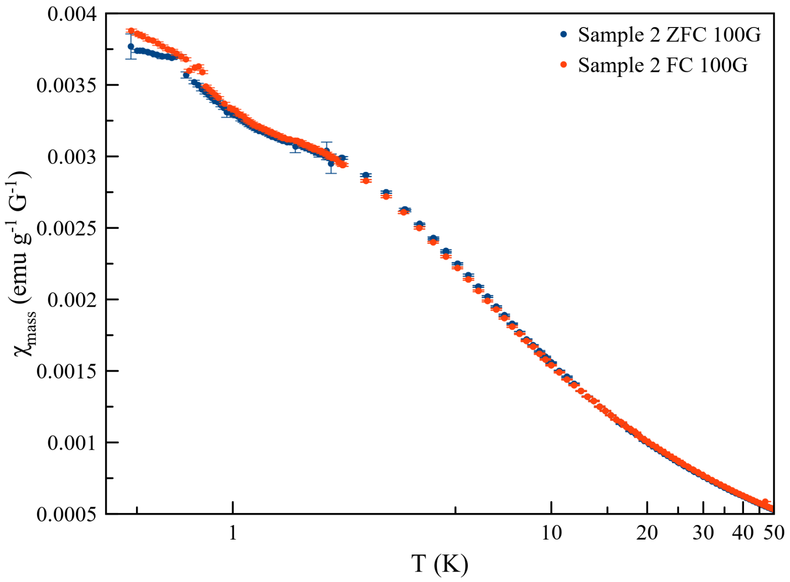

(B) DC susceptibility of Sample 2 in a 100Oe applied magnetic field.

FIGURE 5.3: DC Susceptibility measurements for Samples 1 and 2 in a 100Oe applied magnetic field. Similar features are observed at 0.75K and 3K for both samples.

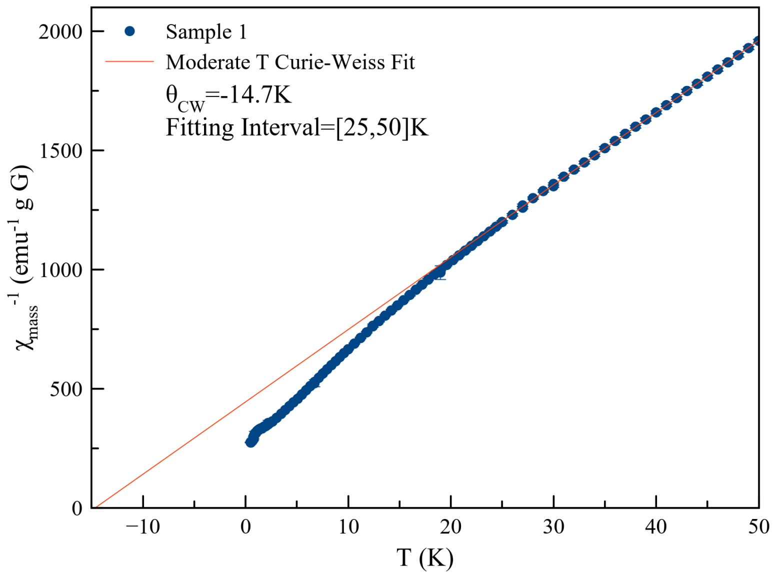

(A) Inverse Susceptibility for Sample 1 fit to a Curie-Weiss law over a moderate temperature region.

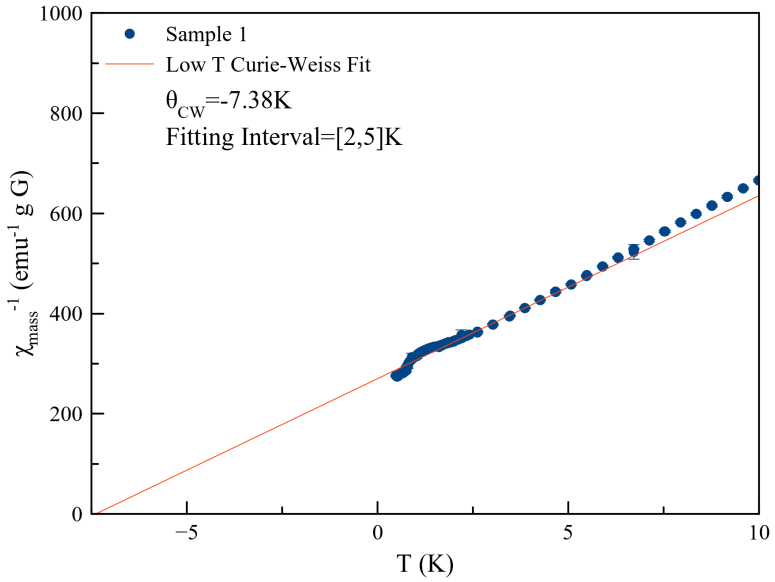

(B) Inverse Susceptibility for Sample 1 fit to a Curie-Weiss law over a low temperature region.

FIGURE 5.4: Inverse susceptibility analysis for Sample 1. Weiss temperatures of -7.38K and -14.7K were observed when performing a fit to a Curie-Weiss law over low temperatures and moderate temperatures respectively.

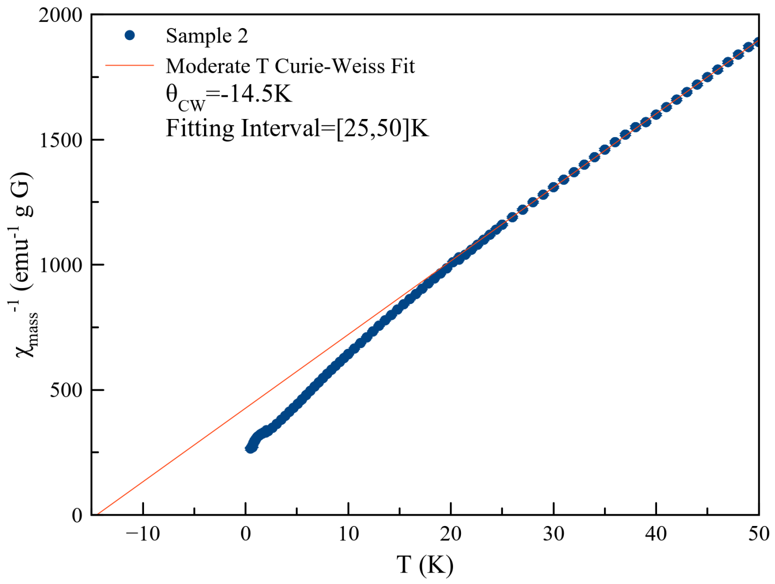

(A) Inverse Susceptibility for Sample 2 fit to a Curie-Weiss law over a moderate temperature region.

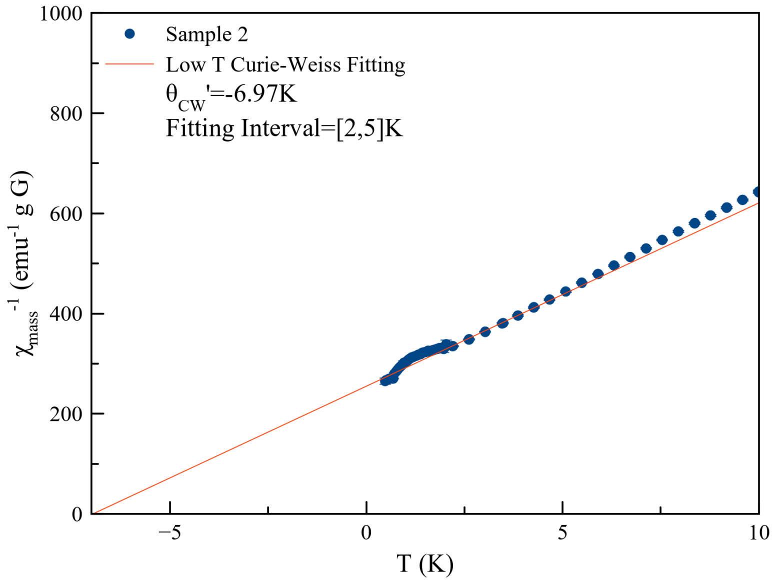

(B) Inverse Susceptibility for Sample 2 fit to a Curie-Weiss law over a low temperature region.

FIGURE 5.5: Inverse susceptibility analysis for Sample 2. Weiss temperatures of -6.97K and -14.5K were observed when performing a fit to a Curie-Weiss law over low temperatures and moderate temperatures respectively.

parameter describing growth of these magnetic correlations with decreasing temperatures. Indeed, two characteristic temperatures can be inferred from this order parameter: the temperature at which the integrated intensity saturates, T^{*}=0.7K, and the temperature at which the intensity begins it's dramatic increase, $T^{*\prime}$=4K. These values are in good agreement with the temperatures at which magnetic features are observed in the DC susceptibility data.

The shape of the elastic magnetic feature is also of considerable interest as it appears to be very asymmetric in q. To elucidate the line shape, the 100K data set was used as a background data set to subtract off the non-magnetic (temperature-independent) features for the elastic line (Figure 5.8b). In so doing, the data revealed a very sharp increase in intensity at low q, followed by a relatively gradual decrease in intensity with increasing q beyond the peak position. This is indicative of two dimensional correlations within the triangular planes. To determine the appropriate two-dimensional correlation lengths, one can fit the data to the equation:[36]

$$I(Q) = Km\frac{F_{hk}^{2}\left[1-2\left(\frac{\lambda Q}{4\pi}\right)^{2}+\left(\frac{\lambda Q}{4\pi}\right)^{4}\right]}{\left(\frac{\lambda Q}{4\pi}\right)^{3/2}}\left(\frac{\xi}{\lambda\sqrt{\pi}}\right)^{1/2}F(a)[f(Q)]^{2} \tag{5.1}$$

where:

$$a = \frac{\xi\sqrt{\pi}}{2\pi}(Q-Q_{0}) \tag{5.2}$$

and:

$$F(a) = \int_{0}^{10}\exp[-(x^{2}-a^{2})]dx \tag{5.3}$$

Here, Q is the magnitude of the scattering wavevector, ξ is the two dimensional spin-spin correlation length characteristic of the correlations within the triangular planes, Q_0 is the peak centre, $f(Q)$ is the magnetic form factor and F_{hk} is the two dimensional structure factor. This line shape is known as the Warren line shape.This signature is similar to that observed in $TbInO_3$ and $(D_3O)Fe_3(SO_4)_2(OD)_6$, although the diffuse peak in $ErMgGaO_4$ is sharper.[36, 37] This implies that the in-plane correlation length in $ErMgGaO_4$ is longer than that in $TbInO_3$ and $(D_3O)Fe_3(SO_4)_2(OD)_6$ (see Figure 6 in [36] and Figure 4 in [37]). Attempts are fitting these line shapes to Equation 5.1 are currently ongoing. A diffuse magnetic structure has also been observed in $YbMgGaO_4$ neutron scattering studies, but those studies were performed on single crystals and thus not averaged over all directions.[1] Because the neutron scattering experiments performed on $YbMgGaO_4$ were conducted using single crystals and not a powder, a direct comparison of the diffuse magnetic scattering is difficult. As such, a powder neutron scattering study should be performed on powder $YbMgGaO_4$ for comparison.

To investigate the spinon excitation continuum, several cuts were taken as a function of energy transfer, centred at different values of q. In examining the q-dependence of these cuts along energy, one can determine whether or not the the spinon continuum is gapped or gapless (i.e. centered on zero energy transfer). Several cuts for selected temperatures are presented in Figure 5.10. When in the QSL state, $ErMgGaO_4$ appears to exhibit a gapped excitation at low q that transitions to a gapless excitation at high q values. Because the majority of the spectral weight of the excitation is centred around high q, this has been classified as a gapless spinon continuum overall, similar to what was observed in [1] for $YbMgGaO_4$. This is, of course, a qualitative argument as fitting the spectrum accurately is impossible without first obtaining a background. Also of interest are a pair of flat excitations in the negative energy channels observed in the 100K data set. They are centred at energies of -3meV and -9meV respectively. This is shown in Figure 5.11. These flat excitations are presumably CEF transitions and provide a proof of concept measurement for a future neutron scattering experiment similar to the one proposed for $Ba_6Yb_2Ti_4O_{17}$.

5.3 Discussion and Future Work

In an attempt to produce the first phase pure single crystals of $ErMgGaO_4$, three FZS experiments were conducted. The first, used a 0.25mm/h feed rod speed and

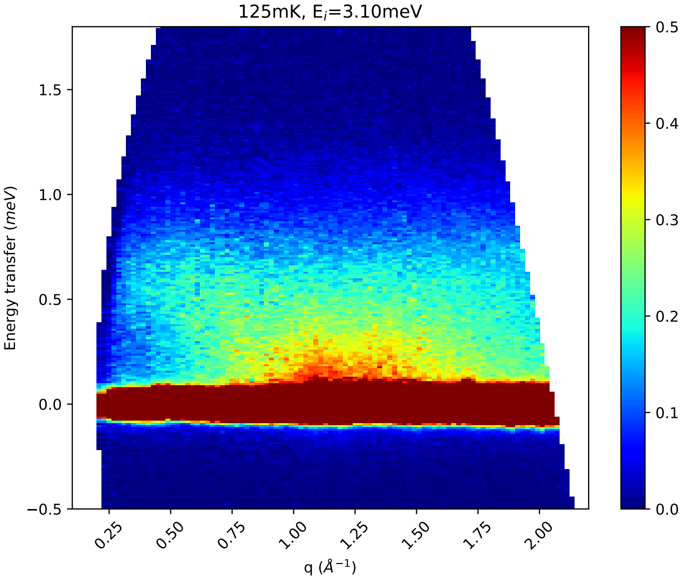

(A) Energy transfer vs. q colour contour plot of $ErMgGaO_4$ at a temperature of 125mK.

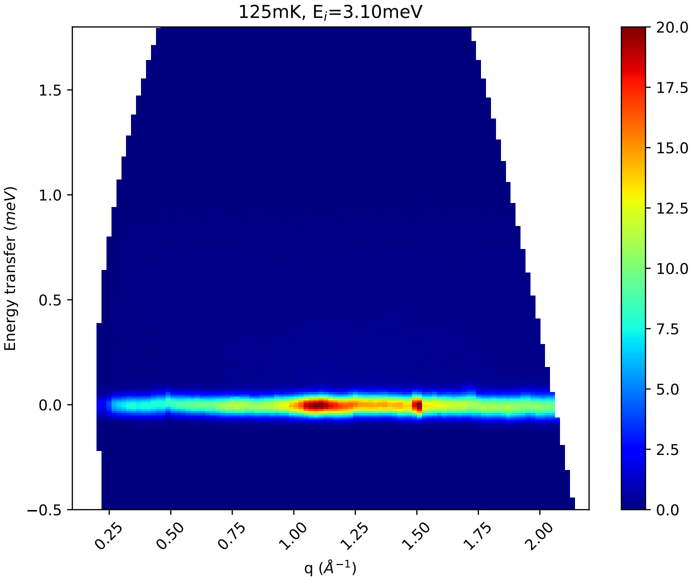

(B) The same data set present in (A) with a larger intensity scale to show the elastic features.

FIGURE 5.6: Energy transfer vs. q for $ErMgGaO_4$ using a 5.12Å incident neutron beam. Here, the inelastic excitations and the elastic features are shown using an appropriate intensity scale.

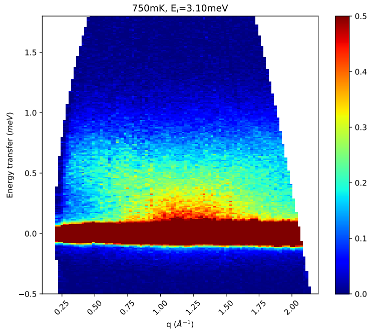

(A) Energy transfer vs. q colour contour plot of ErMgGaO$_4$ at a temperature of 750mK.

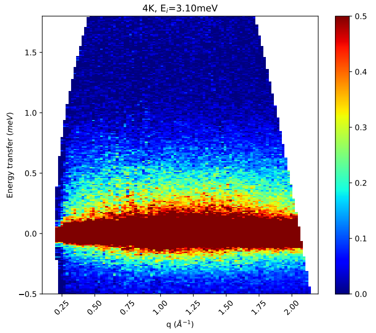

(B) Energy transfer vs. q colour contour plot of ErMgGaO$_4$ at a temperature of 4K.

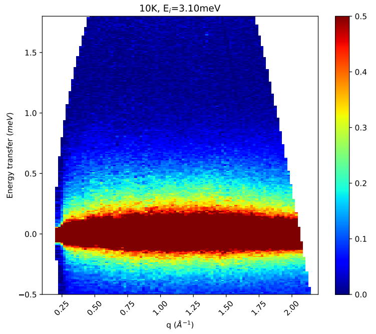

(C) Energy transfer vs. q colour contour plot of ErMgGaO$_4$ at a temperature of 10K.

FIGURE 5.7: Energy transfer vs. q colour contour plots of ErMgGaO$_4$ using a 5.12Å incident neutron beam at selected temperatures.

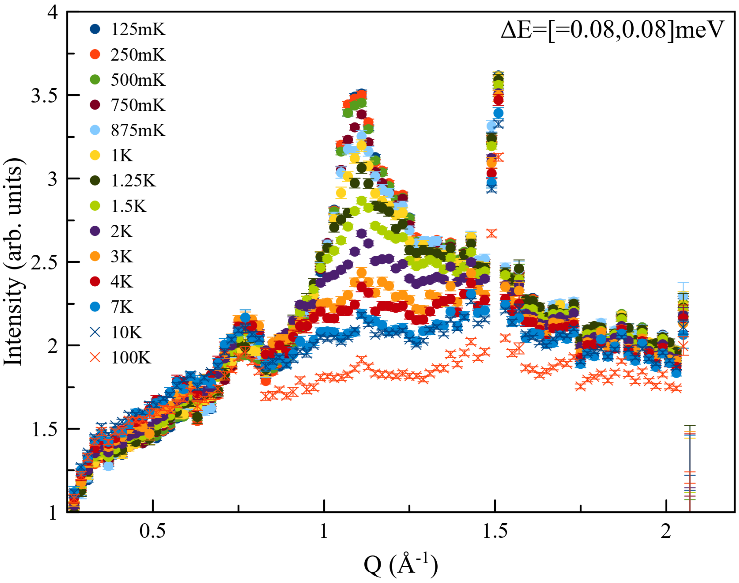

(A) Cuts taken along q for all temperatures with an energy integration range of [-0.08, 0.08]meV.

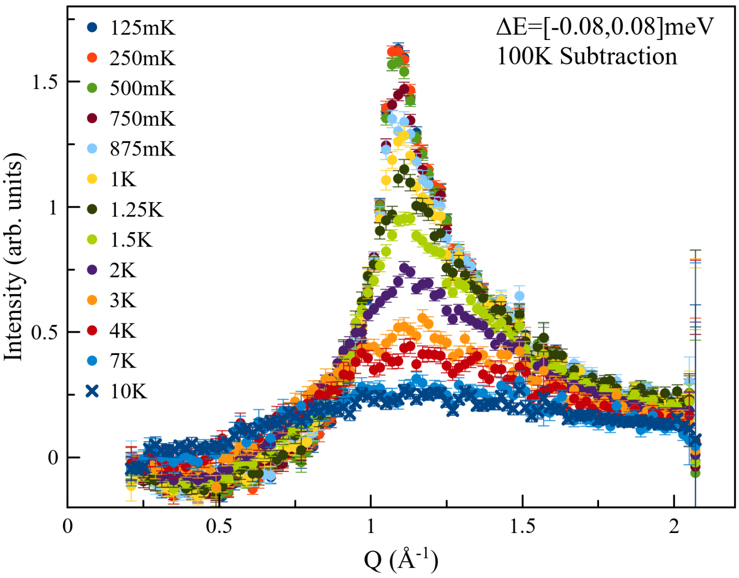

(B) Cuts taken along q for all temperatures with an energy integration range of [-0.08, 0.08]meV with the 100K data set used as a background.

FIGURE 5.8: Elastic neutron scattering from $ErMgGaO_4$. The presence of a diffuse magnetic peak is observed when the temperature is lowered below 4K.

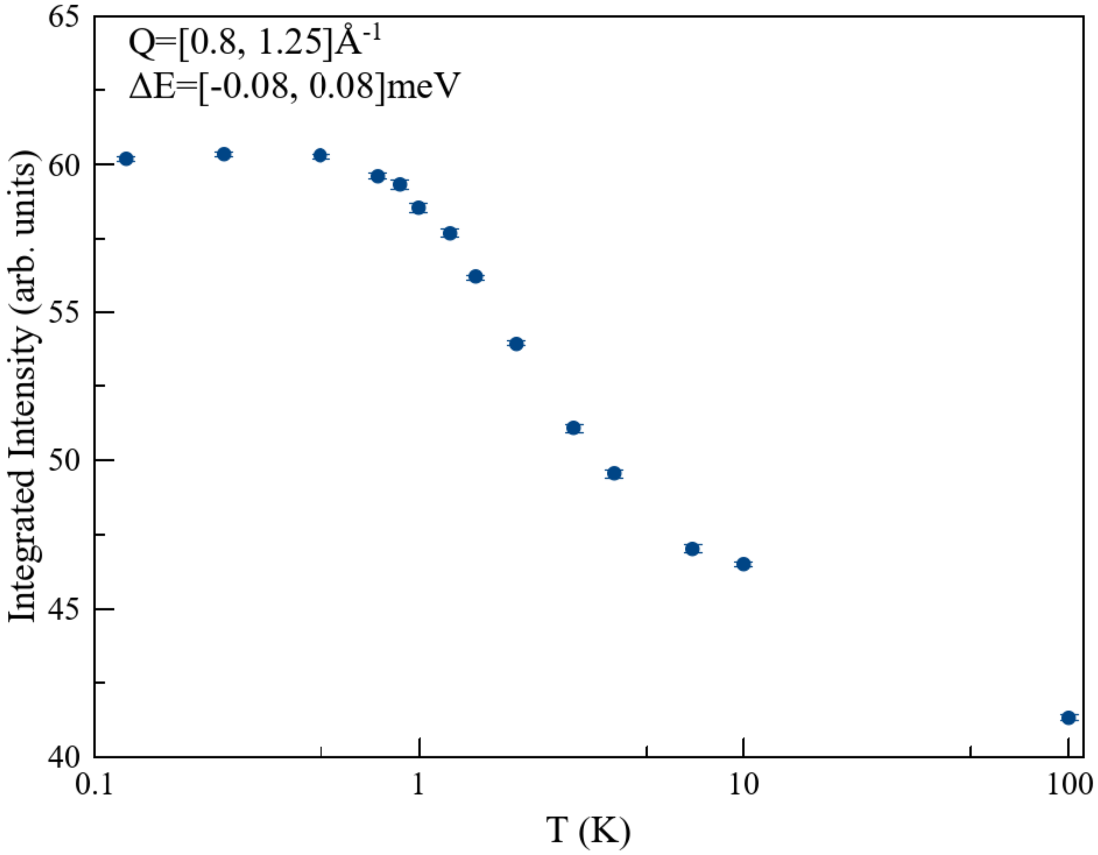

Figure 5.9: Integrated intensity of the q=1.1Å^{-1} magnetic diffuse peak as a function of temperature. Intensity was integrated over q=[0.8, 1.25] Å^{-1}. Here we see the increase in integrated intensity begin to significantly change at approximately 4K and saturate at approximately 0.75K. These temperatures are in good agreement with those observed in the DC susceptibility measurements resented in Figure 5.3a and Figure 5.3b.

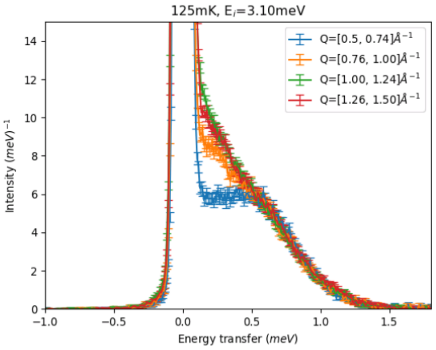

(A) Cuts along energy transfer for $ErMgGaO_4$ at a temperature of 125mK.

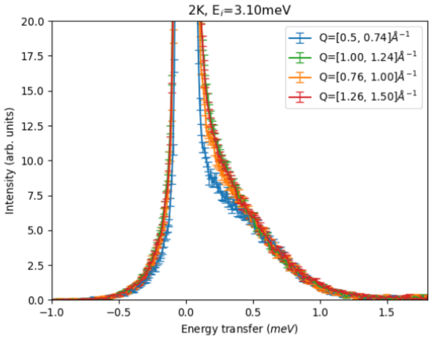

(B) Cuts along energy transfer for $ErMgGaO_4$ at a temperature of 2K.

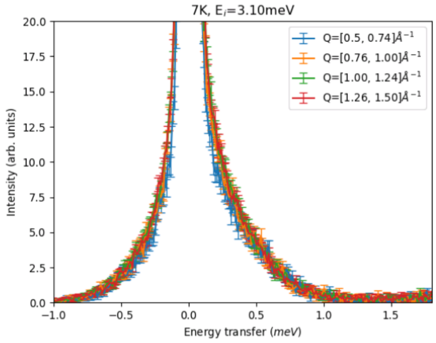

(C) Cuts along energy transfer for $ErMgGaO_4$ at a temperature of 7K.

FIGURE 5.10: Neutron scattering data from $ErMgGaO_4$is shown. Cuts along energy transfer for $ErMgGaO_4$ for selected temperatures using a 5.12Å neutron beam. The spinon continuum appears to be gapped at low q and gapless at moderate to high q.

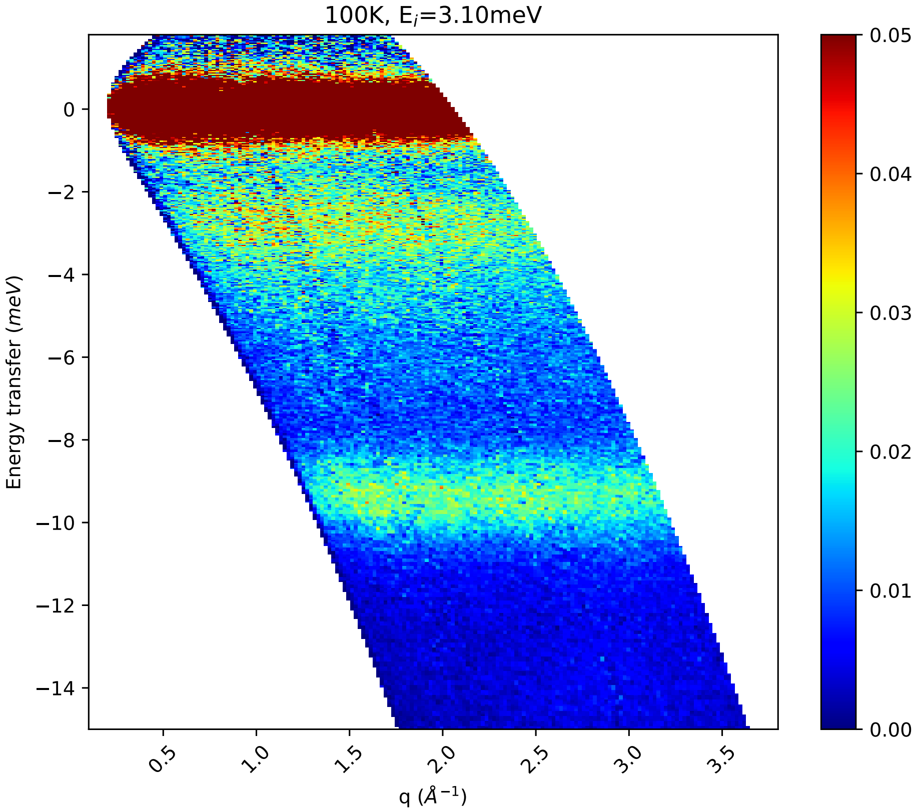

FIGURE 5.11: Neutron scattering data, now focusing on neutron energy gain at high temperatures. Energy transfer vs. q for $ErMgGaO_4$ at 100K. Negative energies are shown to emphasis the presence of the flat excitations at -3meV and -9meV.

a 0.5mm/h seed rod speed. This resulted in a polycrystalline rod that contained sections of $ErMgGaO_4$ material with varying degrees of magnetic $Er_3Ga_5O_{12}$ impurity. The second experiment made use of 2.5mm/h feed and seed rod speeds but this material has yet to be fully characterized. 0.5mm/h feed and seed rod speeds were used to conduct the final growth, which resulted in a rod that was mostly polycrystalline. Several pieces of potentially single crystal $ErMgGaO_4$ have been isolated from the third growth for future Laue XRD characterization. Between the first and third rod, 0.85g of phase pure $ErMgGaO_4$ powder was isolated. This is, to my knowledge, the first time this has been achieved. With most of the phase pure material coming from the third specimen, the optimal material synthesis recipe appears to be feed and seed rod speeds of 0.5mm/h in a 7 atm oxygen gas sample enviroment. This 0.85g sample was relatively small for a neutron scattering study, so it was supplemented with 1.26g of $ErMgGaO_4$ that contained 1.14% $Er_3Ga_5O_{12}$. The potential single crystals isolated from the third FZS experiment are quite small (on the order of 1-2mm in thickness) and as such, larger single crystals would be required for future neutron scattering experiments. To that end, it may be possible to perform a number of FZS experiments to produce a large amount of phase pure polycrystalline material, then pack that into rods under high pressure, and perform a subsequent FZS experiment on those rods. Because FZS experiments are usually performed on phase pure powders, this may produce single crystals.

To estimate the extent by which magnetic features exhibited by the $Er_3Ga_5O_{12}$ impurity may effect the neutron scattering signatures, a DC susceptibility measurement was performed. This experiment was performed in a constant applied field of 100Oe and measured as a function of temperature between 0.5K and 50K. The susceptibilities of both the pure $ErMgGaO_4$ sample and the sample containing a nominal amount of $Er_3Ga_5O_{12}$ were remarkably similar. Both materials exhibit a broad magnetic feature at 3-4K and a spin-glass like transition at 0.75K. Because these features are present in both data sets, they are presumed to be intrinsic to phase pure $ErMgGaO_4$. The 3-4K feature does not appear to present in reported studies focused on $ErMgGaO_4$ with higher levels of impurity,[27] Analysis of the inverse susceptibility revealed consistent Weiss temperatures between the two samples when the fitting was performed over low temperature and moderate temperature ranges. It also revealed antiferromagnetic interactions between local magnetic moments down to 0.5K. These samples were then selected to be used in a neutron scattering study using IN6-SHARP.

A neutron scattering experiment performed using a 5.12Å incident neutron beam was performed at various temperatures. In the low temperature regime, colour contour plots revealed the presence of a spinon continuum that is quite similar to the one observed in $YbMgGaO_4$.[1] The bandwidth of this continuum of excitations was found to be 0.8meV. This commonality between the two materials would suggest that both materials exhibit very similar QSL correlations. Cuts taken along the energy transfer axis centred at different values of q reveal that the spinon continuum is gapped at low q and gapless at moderate to high values of q. This would suggest that the spinon continuum is gapless overall as the majority of the spectral weight is concentrated at moderate to high q. These cuts as well as the colour contour plots show that the spinon continuum persists to 4K. Also revealed in the low temperature colour contour plots is the presence of a magnetic diffusive elastic feature centred at q=1.1Å^{-1}. The integrated intensity of this feature was plotted as a function of temperature to determine an order parameter of the magnetic state. From the order parameter, two characteristic temperatures were estimated: T^*=0.7K and $T^{*\prime}$=4K, which is consistent with the characteristic temperatures observed in the susceptibility data. When the 100K data is used as a background subtraction, the line shape of this magnetic excitation was found to be that of a Warren line shape. This suggests that there are two dimensional correlations within the two dimension triangular planes. The correlations are characterized by a correlation length that can be estimated when the line shape is fit to the Warren function. This is qualitatively similar to the elastic magnetic peak observed in cold neutron scattering from $TbInO_3$.[37]

To complete the study of $ErMgGaO_4$, several experiments have been proposed. The first is a thermal neutron scattering experiment intended to elucidate the ground state and excited CEF state wave functions of $ErMgGaO_4$, similar to the experiment proposed for $Ba_6Yb_2Ti_4O_{17}$. This should also determine an experimentally accurate g-tensor for the Er^{3+} ions in this system. The 100K neutron scattering data set revealed two low energy CEF doublets so an instrument like

SEQUOIA at Oak Ridge National Laboratories (ORNL) in Oak Ridge, Tennessee, USA should be very effective in measuring the full spectrum of crystal field excitations appropriate to Er^{3+}. Magnetization versus applied magnetic field measurements should also be performed to experimentally estimate the g-tensor as well as the antiferromagnetic coupling constant. A cold neutron scattering experiment in a magnetic field will show how the spinon continuum and the local magnetic moments interact with an applied magnetic field. Cold neutron scattering should be performed on powder $YbMgGaO_4$ in order to compare the nature of the magnetic elastic diffuse scattering in $ErMgGaO_4$ and $YbMgGaO_4$.

Chapter 6

Conclusions

The powder synthesis procedure for $Ba_6Yb_2Ti_4O_{17}$ was optimized to produce a powder containing nominal amounts of $BaTiO_3$ and Yb_2O_3 impurities - that is, a procedure of annealing a stoichiometric mixture of $BaCO_3$, Yb_2O_3 and TiO_2 at 1500° C in air for 48 hours. Synthesis experiments using lower temperatures resulted in the presence of unknown impurity phases and experiments performed using longer times generally resulted in more $BaTiO_3$ in the sample. This would suggest that $Ba_6Yb_2Ti_4O_{17}$ is a unstable phase. This assertion is further corroborated by the instability of the molten zone observed in FZS experiments. When molten, $Ba_6Yb_2Ti_4O_{17}$ exhibits a low viscosity as well as a phase separation within the melt. The two phases appear to have slightly different melting temperatures. This resulted in the molten zone being prone to spill over the sides of the seed rod while also having a tendency to grind. It is for these reasons that no single crystals of $Ba_6Yb_2Ti_4O_{17}$ have been produced to date.

DC susceptibility, a theoretical point charge calculation of the Yb^{3+} crystal field states, and cold neutron inelastic scattering were used to characterize the magnetic ground state of $Ba_6Yb_2Ti_4O_{17}$. DC susceptibility revealed no spin freezing or magnetic ordering down to 0.5K. Inverse susceptibility revealed Weiss temperatures of -0.37K and -11.3K when the Curie-Weiss fitting was performed over a low temperature region and moderate temperature region respectively. This suggests that the local magnetic moments in $Ba_6Yb_2Ti_4O_{17}$ are antiferromagnetically coupled but weakly interacting at low temperatures. A cold neutron scattering study using the DCS instrument at NIST showed no obvious signs of a spinon continuum in the raw data. Several background subtractions were performed in an attempt to see weak scattering features. In fact, an excitation continuum may be present with a bandwidth of 0.3meV but, due to the signal to noise ratio and the weakness of the intensity, it is not possible to say it is there for certain. If this is the spinon continuum, one could then conclude that $Ba_6Yb_2Ti_4O_{17}$ is a QSL candidate material with substantially weaker interactions between local moments than those observed in $YbMgGaO_4$.[1] The neutron scattering experiment also revealed the energy splitting of the ground state Kramer's doublet as a function of increasing field. Analysis of this phenomenon estimates the powder averaged g-tensor to be approximately 2.4. This value is smaller than the g-tensor observed in $YbMgGaO_4$.[19] Using a theoretical point charge model, the wavefunction and eigenenergies of the ground state and excited state crystal field doublets for Yb^{3+} were estimated. Using these calculated doublets, the g-tensor was estimated to be relatively isotropic. The powder averaged g-tensor resulting from the point charge crystal field calculation is in good agreement with the experimentally observed g-tensor from neutron scattering. To complete this study, magnetization versus applied magnetic field measurements should be conducted to estimate the antiferromagnetic coupling constant. Thermal neutron scattering should also be conducted, as this will allow from the CEF Hamiltonian to be accurately derived and thus the eigenvalues and eigenvectors of ground state and excited state CEF doublets can be experimentally defined. It would also provide an accurate measure of the g-tensor.

For the first time, $ErMgGaO_4$ has been synthesized without a detectable $Er_3Ga_5O_{12}$ impurity present due to the resolution limit of approximately 1% from the instrument and the fitting. This was achieved using an optimized FZS procedure using 0.5mm/h feed and seed rod speeds in a 7 atm oxygen gas sample environment. After three FZS experiments, 0.85g of phase pure $ErMgGaO_4$ powder was isolated along with 1.26g of $ErMgGaO_4$ powder containing 1.14% $Er_3Ga_5O_{12}$. These powders were characterized using a combination of DC susceptibility and cold neutron scattering. The susceptibility measurements reveal common signatures between the two samples. Both powders exhibit a broad feature at 3K (a feature that is not observed for higher $Er_3Ga_5O_{12}$ concentrations [27]) and a similar hysteresis between ZFC and FC at 0.75K. Inverse susceptibility also revealed both powders exhibit antiferromagnetic coupling between local magnetic moments via the negative Weiss temperatures. The Weiss temperature in both samples are approximately the same. This suggests that the magnetic phenomena observed would be intrinsic to $ErMgGaO_4$.

A neutron scattering study in the absence of an applied magnetic field was performed on this phase pure powder of $ErMgGaO_4$ at temperatures ranging from 125mK to 100K. The 125mK data set revealed a spinon continuum that is remarkably similar to the one observed in $YbMgGaO_4$.[1] The continuum displayed a bandwidth of 0.8meV at 125mK and persisted until 4K. This continuum was found to be gapless, much like the spinon continuum in $YbMgGaO_4$.[1] Analysis of the elastic energy scattering revealed the evolution of a diffuse magnetic peak as a function of decreasing temperature that is incommensurate with the allowed nuclear Bragg peaks for $ErMgGaO_4$. Upon subtraction of the 100K data set, the magnetic feature appears to be qualitatively consistent with a Warren line shape. This implies the presence of two dimensional correlations associated with a characteristic two dimensional correlation length, similar to what is observed in $TbInO_3$ and $(D_3O)Fe_3(SO_4)_2(OD)_6$.[36, 37] Because the Warren peak is sharper in $ErMgGaO_4$ than in $TbInO_3$ and $(D_3O)Fe_3(SO_4)_2(OD)_6$, this would imply that the in-plane correlation length is longer in $ErMgGaO_4$. Fitting the data to the Warren function to determine this characteristic length is under way. CEF transitions were also observed in the 100K data set at negative energies. This has been used as a proof of concept measurement in a proposed experiment using SEQUOIA at ORNL to examine the CEF excitations in $ErMgGaO_4$.

Bibliography

[1] J. A. M. Paddison, M. Daum, Z. Dun, G. Ehlers, Y. Liu, M. B. Stone, H. Zhou, and M. Mourigal. Continuous excitations of the triangular-lattice quantum spin liquid YbMgGaO_4. *Nature Physics*, 13:117–122, 2017.

[2] Stephen Blundell. *Magnetism in Condensed Matter.* Oxford University Press, 2001.

[3] M. T. Hutchings. Point-charge calculations of energy levels of magnetic ions in crystalline electric fields. *Solid State Physics*, 16(227), 1964.

[4] A. J. Freeman and R. E. Watson. Theoretical investigation of some magnetic and spectroscopic properties of rare-earth ions. *Physical Review*, 127(6), 1962.

[5] U. Walter. Treating crystal field parameters in lower than cubic symmetries. *J. Phys. Chem. Solids*, 45(4), 1984.

[6] G. L. Squires. *Introduction to the theory of thermal neutron scattering.* Cambridge University Press, 1978.

[7] N. W. Ashcroft and N. D. Mermin. *Solid State Physics.* Holt-Saunders, 1976.

[8] Tôru Moriya. Anisotropic superexchange interaction and weak ferromagnetism. *Phys. Rev.*, 120:91–98, Oct 1960.

[9] David Chandler. *Introduction to Modern Statistical Mechanics.* Oxford University Press, 1987.

[10] G. H. Wannier. Antiferromagnetism. the triangular ising net. *Physical Review*, 79(2), 1950.

[11] L. Balents. Spin liquids in frustrated magnets. *Nature Review*, 401, 2010.

[12] A. P. Ramirez, A. Hayashi, R. J. Cava, R. Siddharthan, and B. S. Shastry. Zero-point entropy in 'spin ice'. *Nature*, 399:333–334, 1999.

[13] P. W. Anderson. Resonating valence bonds: a new kind of insulator. *Mat. Res. Bull.*, 8:153–160, 1973.

[14] Li Y., Zhang H., Zhang Z., Li S., Jin F., Ling L., Zhang L., Zou Y., Pi L., Yang Z., Wang J., Wu Z., and Zhang Q. Gapless quantum spin liquid ground state in the two-dimensional spin-1/2 triangular antiferromagnet $\mathrm{YbMgGaO_4}$. *Sci Rep*, 5(16419), 2015.

[15] Y. Shimizu, K. Miyagawa, K. Kanoda, M. Maesato, and G. Saito. Spin liquid state in an organic mott insulator with a triangular lattice. *Phys. Rev. Lett.*, 91:107001, Sep 2003.

[16] T. Itou, A. Oyamada, S. Maegawa, M. Tamura, and R. Kato. Quantum spin liquid in the spin-1/2 triangular antiferromagnet $\mathrm{EtMe_3Sb[Pd(dmit)_2]_2}$. *Phys. Rev. B*, 77:104413, Mar 2008.

[17] T. Ono, H. Tanaka, H. Aruga Katori, F. Ishikawa, H. Mitamura, and T. Goto. Magnetization plateau in the frustrated quantum spin system $\mathrm{Cs_2CuBr_4}$. *Phys. Rev. B*, 67:104431, Mar 2003.

[18] Koichi Momma and Fujio Izumi. *VESTA3* for three-dimensional visualization of crystal, volumetric and morphology data. *Journal of Applied Crystallography*, 44(6):1272–1276, Dec 2011.

[19] Yuesheng Li, Gang Chen, Wei Tong, Li Pi, Juanjuan Liu, Zhaorong Yang, Xiaoqun Wang, and Qingming Zhang. Rare-earth triangular lattice spin liquid: A single-crystal study of $\mathrm{YbMgGaO_4}$. *Phys. Rev. Lett.*, 115:167203, Oct 2015.

[20] Y. Shen, Y. Li, and Wo H. *et. al.* Evidence for a spinon fermi surface in a triangular-lattice quantum-spin-liquid candidate. *Nature*, 540:559–562, 2016.

[21] Y. Xu, J. Zhang, Y. S. Li, Y. J. Yu, X. C. Hong, Q. M. Zhang, and S. Y. Li. Absence of magnetic thermal conductivity in the quantum spin-liquid candidate $\mathrm{ybmggao_4}$. *Phys. Rev. Lett.*, 117:267202, Dec 2016.

[22] Yao-Dong Li, Yao Shen, Yuesheng Li, Jun Zhao, and Gang Chen. Effect of spin-orbit coupling on the effective-spin correlation in $YbMgGaO_4$. *Phys. Rev. B*, 97:125105, Mar 2018.

[23] Lucile Savary and Leon Balents. Disorder-induced quantum spin liquid in spin ice pyrochlores. *Phys. Rev. Lett.*, 118:087203, Feb 2017.

[24] Yuesheng Li, Devashibhai Adroja, Robert I. Bewley, David Voneshen, Alexander A. Tsirlin, Philipp Gegenwart, and Qingming Zhang. Crystalline electric-field randomness in the triangular lattice spin-liquid $YbMgGaO_4$. *Phys. Rev. Lett.*, 118:107202, Mar 2017.

[25] Zhenyue Zhu, P. A. Maksimov, Steven R. White, and A. L. Chernyshev. Disorder-induced mimicry of a spin liquid in $YbMgGaO_4$. *Phys. Rev. Lett.*, 119:157201, Oct 2017.

[26] Itamar Kimchi, Adam Nahum, and T. Senthil. Valence bonds in random quantum magnets: Theory and application to $YbMgGaO_4$. *Phys. Rev. X*, 8:031028, Jul 2018.

[27] Y. Cai, C. Lygouras, G. Thomas, M. N. Wilson, J. Beare, S. Sharma, C. A. Marjerrison, D. R. Yahne, K. A. Ross, Z. Gong, Y. J. Uemura, H. A. Dabkowska, and G. M. Luke. μsr study of the triangular ising antiferromagnet $ErMgGaO_4$. *Phys. Rev. B*, 101:094432, Mar 2020.

[28] F. Alex Cevallos, Karoline Stolze, and Robert J. Cava. Structural disorder and elementary magnetic properties of triangular lattice $ErMgGaO_4$ single crystals. *Solid State Communications*, 276:5 – 8, 2018.

[29] Y. Cai, M. N. Wilson, J. Beare, C. Lygouras, G. Thomas, D. R. Yahne, K. Ross, K. M. Taddei, G. Sala, H. A. Dabkowska, A. A. Aczel, and G. M. Luke. Crystal fields and magnetic structure of the ising antiferromagnet $Er_3Ga_5O_{12}$. *Phys. Rev. B*, 100:184415, Nov 2019.

[30] B. D. JOSEPHSON. Coupled superconductors. *Rev. Mod. Phys.*, 36:216–220, Jan 1964.

[31] James F. Annett. *Superconductivity, Superfluids, and Condensates.* Oxford University Press, 2013.

[32] Michael Tinkham. *Introduction to Superconductivity.* Dover Publications, 2015.

[33] A. Scheie. Pycrystalfield: Software for calculation, analysis, and fitting of crystal electric field hamiltonians. 2020.

[34] R.T. Azuah, L.R. Kneller, Y. Qiu, P.L.W. Tregenna-Piggott, C.M. Brown, J.R.D. Copley, and R.M. Dimeo. Dave: A comprehensive software suite for the reduction, visualization, and analysis of low energy neutron spectroscopic data. *J. Res. Natl. Inst. Stan. Technol.*, 114(6), 2009.

[35] O. Arnold, J.C. Bilheux, J.M. Borreguero, A. Buts, S.I. Campbell, L. Chapon, M. Doucet, N. Draper, R. Ferraz Leal, M.A. Gigg, V.E. Lynch, A. Markvardsen, D.J. Mikkelson, R.L. Mikkelson, R. Miller, K. Palmen, P. Parker, G. Passos, T.G. Perring, P.F. Peterson, S. Ren, M.A. Reuter, A.T. Savici, J.W. Taylor, R.J. Taylor, R. Tolchenov, W. Zhou, and J. Zikovsky. Mantid—data analysis and visualization package for neutron scattering and sr experiments. *Nuclear Instruments and Methods in Physics Research Section A: Accelerators, Spectrometers, Detectors and Associated Equipment*, 764:156 – 166, 2014.

[36] A. S. Wills, G. S. Oakley, D. Visser, J. Frunzke, A. Harrison, and K. H. Andersen. Short-range order in the topological spin glass $(D_3O)Fe_3(SO_4)_2(OD)_6$ using **xyz** polarized neutron diffraction. *Phys. Rev. B*, 64:094436, Aug 2001.

[37] L. Clark, G. Sala, and D. D. Maharaj *et. al.* Two-dimensional spin liquid behaviour in the triangular-honeycomb antiferromagnet $TbInO_3$. *Nature*, 15:262–268, 2019.